5-2019

Light Extraction Efficiency of Nanostructured III-Nitride Light-Emitting Diodes

Yu Kee Ooi
yo4083@rit.edu

R·I·T

Light Extraction Efficiency of Nanostructured III-Nitride Light-Emitting Diodes

by

Yu Kee Ooi

A dissertation submitted in partial fulfillment of the requirements

for the degree of Doctorate of Philosophy in Microsystems Engineering

Microsystems Engineering Program

Kate Gleason College of Engineering

Rochester Institute of Technology

Rochester, New York

May, 2019

Light Extraction Efficiency of Nanostructured III-Nitride Light-Emitting Diodes

by

Yu Kee Ooi

Committee Approval:

We, the undersigned committee members, certify that we have advised and/or supervised the candidate on the work described in this dissertation. We further certify that we have reviewed the dissertation manuscript and approve it in partial fulfillment of the requirements of the degree of Doctor of Philosophy in Microsystems Engineering.

Jing Zhang, Ph.D. Date
Assistant Professor, Electrical and Microelectronic Engineering

---

Santosh Kurinec, Ph.D. Date
Professor, Electrical and Microelectronic Engineering

Parsian Mohseni, Ph.D. Date
Assistant Professor, Microsystems Engineering

Sean Rommel, Ph.D. Date
Professor, Electrical and Microelectronic Engineering

Certified by:

Bruce Smith, Ph.D. Date
Director, Microsystems Engineering Program

ABSTRACT

Kate Gleason College of Engineering
Rochester Institute of Technology

Degree: Doctor of Philosophy **Program:** Microsystems Engineering
Author Name: Yu Kee Ooi
Advisor Name: Dr. Jing Zhang
Dissertation Title: Light Extraction Efficiency of Nanostructured III-Nitride Light-Emitting Diodes

III-nitride materials have been extensively employed in a wide variety of applications attributed to their compact sizes, lower operating voltage, higher energy efficiency and longer lifetime. Although tremendous progress has been reported for III-nitride light-emitting diodes (LEDs), further enhancement in the external quantum efficiency (η_{EQE}), which depends upon internal quantum efficiency, injection efficiency and light extraction efficiency ($\eta_{extraction}$), is essential in realizing next generation high-efficiency ultraviolet (UV) and visible LEDs. Several challenges such as charge separation issue, large threading dislocation density, large refractive index contrast between GaN and air, and anisotropic emission at high Al-composition AlGaN quantum wells in the deep-UV regime have been identified to obstruct the realization of high-brightness LEDs. As a result, novel LED designs and growth methods are highly demanded to address those issues.

The objective of this dissertation is to investigate the enhancement of $\eta_{extraction}$ for various nanostructured III-nitride LEDs. In the first part, comprehensive studies on the polarization-dependent $\eta_{extraction}$ for AlGaN-based flip-chip UV LEDs with microdome-shaped patterned sapphire substrates (PSS) and AlGaN-based nanowire UV LEDs are presented. Results show that the microdome-shaped PSS acts as an extractor for transverse-magnetic (TM)-polarized light where up to ∼11.2-times and ∼2.6-times improvement in TM-polarized $\eta_{extraction}$ can be achieved for 230 nm and 280 nm flip-chip UV LEDs, while as a reflector that limits the extraction of transverse-electric (TE)-polarized light through the sapphire substrate. Analysis for 230 nm UV LEDs with nanowire structure shows up to ∼48% TM-polarized

$\eta_{extraction}$ and ~41% TE-polarized $\eta_{extraction}$ as compared to the conventional planar structure (~0.2% for TM-polarized $\eta_{extraction}$ and ~2% for TE-polarized $\eta_{extraction}$). Plasmonic green LEDs with nanowire structure have also been investigated for enhancing the LED performance via surface plasmon polaritons. The analysis shows that both $\eta_{extraction}$ and Purcell factor for the investigated plasmonic nanowire LEDs are independent of the Ag cladding layer thickness (H_{Ag}), where a Purcell factor of ~80 and $\eta_{extraction}$ of ~65% can be achieved when $H_{Ag} > 60$ nm. Nanosphere lithography and KOH-based wet etching process have been developed for the top-down fabrication of III-nitride nanowire LEDs. The second part of this dissertation focuses on alternative approaches to fabricate white LEDs. The integration of three-dimensional (3D) printing technology with LED fabrication is proposed as a straightforward and highly reproducible method to improve $\eta_{extraction}$ at the same time to achieve stable white color emission. The use of optically transparent acrylate-based photopolymer with a refractive index of ~1.5 as 3D printed lens on blue LED has exhibited ~9% enhancement in the output power at current injection of 4 mA as compared to blue LED without 3D printed lens. Stable white color emission can be achieved with chromaticity coordinates around (0.27, 0.32) and correlated color temperature ~8900 K at current injection of 10 mA by mixing phosphor powder in the 3D printed lens. Novel LED structures employing ternary InGaN substrates are then discussed for realizing high-efficiency monolithic tunable white LEDs. Results show that large output power (~170 mW), high η_{EQE} (~50%), chromaticity coordinates around (0.30, 0.28), and correlated color temperature ~8200 K can be achieved by engineering the band structures of the InGaN/InGaN LEDs on ternary InGaN substrates.

Acknowledgements

I would like to express my deepest gratitude to my advisor, Dr. Jing Zhang, for her mentorship, guidance and encouragement. I am grateful for the opportunity that Dr. Zhang has provided me – this dissertation would not have been possible without her constant support and guidance. She has been a wonderful mentor and role model throughout my Ph.D. study, and she has taught me many things that extend well beyond research. I am very fortunate to have her as my Ph.D. advisor and mentor.

I also would like to thank my committee members, Dr. Santosh Kurinec, Dr. Parsian Mohseni, and Dr. Sean Rommel, for providing me insightful suggestions and recommendations for my research work. I also gratefully acknowledge my external committee member, Dr. Rui Liu, for his valuable remarks and useful discussions.

I also would like to acknowledge the contributions of my research group members (Very-Soon-To-Be-Dr. Cheng Liu, Soon-To-Be-Dr. Matthew Hartensveld, Xing Lei, Gildas Ouin, Eric Evangelou, Christopher Ugras, and Rahnuma Rifat Chowdhury) for their help and useful discussions. In particular, I am very thankful to Cheng and Matt for always being available for support and discussions, and the many hours of companionship working in the cleanroom and the labs.

I also would like to acknowledge the contributions of Dr. Denis Cormier and his group, particularly Chaitanya Mahajan and Shaunak Gandhi, for their help in 3D printing.

I also would like to acknowledge the staffs of RIT SMFL, including Sean O'Brien, Patricia Meller, John Nash, Richard Battaglia, Bruce Tolleson, Thomas Grimsley, Scott Blondell, Peter Morici, and Dr. Karl Hirschman, for their support in the cleanroom.

I also would like to thank the faculty and staffs in the Microsystems Engineering Program and the Department of Electrical and Microelectronic Engineering for their help and guidance throughout my time at RIT. Special thanks to Dr. Bruce Smith,

Lisa Zimmerman, James Stefano, Kenneth Snyder, Florence Layton, Dr. James Moon, Mark Indovina, Dr. Robert Pearson, Dr. Stefan Preble and Dr. Seth Hubbard for their patience and assistance in many things.

I also would like to thank my all friends Elisabeth McClure, Dr. Mario Saucedo Espinosa, Dr. Mert Corbaci, Yali Zhang, Simon Shipkowski, Jennifer Shipkowski, Mohadeseh Asadolahi-Baboli, Peng Han, Michelle Horan, Dr. Xiang Li, Xiaoya Shen, Dr. Lei Fan, and many more. Thank you for all the fun and laughter that make this long journey a fun and memorable adventure.

Finally I would like to thank my family member – this journey would not have been possible without the unconditional love and support of my mother, Gaik Lee Chan, my grandmother, Ah Moy Khor, my husband, Dr. Yong Lin Kong, my sister, Tracy Ooi, my brother, Jaspher Ooi, my nephew, Jun Hong Lim, and my parents-in-law, Chin Chin Kong and Chui Pheng Ang. They have been inspiration sources for me, and have supported and motivated me in many different ways over the many years it took to get to where I am today.

To my family.

Contents

List of Tables

List of Figures

Chapter 1

Introduction

III-nitride semiconductors have attracted significant attention as candidate materials for various optoelectronic applications in both visible and ultraviolet (UV) regime due to their direct band gaps and wide spectral region. This chapter provides an overview of III-nitride materials, in particular for light-emitting diodes (LEDs), and discusses their recent progress and development. Motivations and summary of the research works accomplished have also been included in the discussion.

1.1 Overview of III-Nitride LEDs

III-nitride materials possess a number of attractive physical, optical and electronic properties that make them the subject of active research field for numerous electronic and optoelectronic devices in the past three decades. The binary compounds (GaN, InN and AlN) as well as their ternary and quaternary alloys offer tunable band gap from 0.8 eV to 6 eV (Figure 1.1), which cover the whole visible spectrum and into the deep-UV (DUV) region. In the early days, the lack of p-type GaN as well as the poor crystalline quality have impeded the progression of III-nitride emitters. The historic turning point in the development of III-nitride semiconductors came when the first GaN UV/blue LED being demonstrated in the early 1990s [1, 2]. Since then, the

advances in III-nitride semiconductors research have enabled the widespread market for nitride-based emitters in solid-state lighting. In particular, GaN and ternary InGaN alloy have become dominant materials for producing high brightness blue and green LEDs and laser diodes in replacing conventional incandescent and fluorescent light bulbs for various applications. The ability to obtain white color emission by the use of a single blue LED in combination with phosphors as well as the color tunability to achieve any color in the visible spectrum by the combination of red, green and blue LEDs have made III-nitride LEDs suitable for numerous applications ranging from traffic signals, full color displays, automotive backlighting to general illumination. On the other hand, tremendous efforts have also been devoted to III-nitride UV emitters as new UV light sources for various applications, such as semiconductor photolithography, resin curing for three dimensional (3D) printing, water and air purification, sterilization, bioagent detection, and biological and chemical sensing.

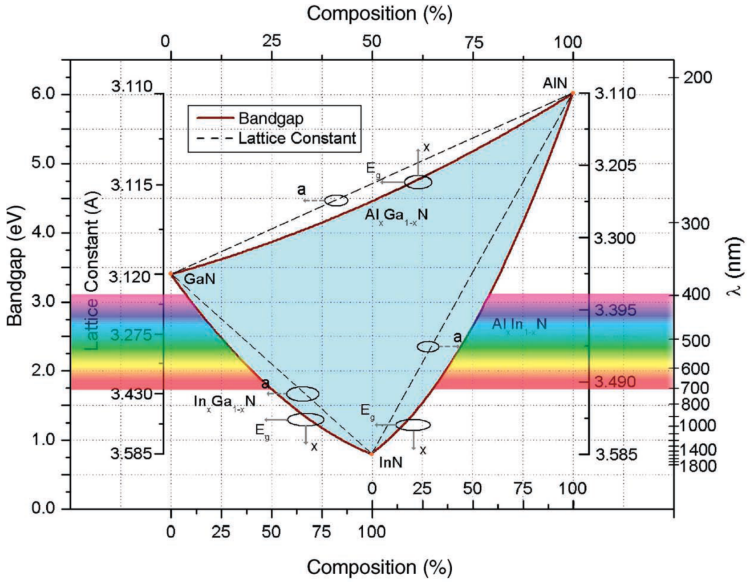

Figure 1.1: Band gaps and lattice constants for GaN, InN, AlN and their ternary alloys [3].

As opposed to conventional incandescent light bulbs and mercury lamps, III-nitride LEDs are more compact in size, consume less power, generate less heat,

have higher energy efficiency and longer lifetime. Nevertheless, several technological roadblocks and market challenges still need to be overcome for realizing next generation high-efficiency and high-brightness LEDs. One of the issues is the lack of cost-effective lattice-matched substrates for growing III-nitride materials. The most commonly used substrates for III-nitride devices are sapphire and silicon carbide attributed to their chemical stability during the aggressive growth environment. The use of native substrates such as bulk GaN and bulk AlN which are lattice-matched to GaN have also been attempted. However, the expensive cost of these substrates leads to a much more expensive III-nitride LED lamp than conventional light sources. Consequently, epitaxial growth of GaN on silicon substrates has been investigated as the silicon substrates can be obtained at a very cheap price, which is expected to reduce the material cost of the LEDs significantly. However, the crystalline quality of GaN epitaxial layers and the performance characteristics of LEDs on silicon substrates are still inferior to those on sapphire substrates. Alternative oxide substrates such as ZnO, $LiGaO_2$ and $MgAl_2O_4$, and metallic substrates such as copper, silver and nickel [4, 5], have also been attempted to find substrate which has better lattice match, better thermal and chemical stability as well as more economical than the sapphire substrate.

III-nitride semiconductors also suffer from strong polarization: 1) spontaneous polarization arose from the non-uniform sharing of electrons in III-nitride bonds between the group III metals (Al, Ga and In) and nitrogen; and 2) piezoelectric polarization caused by the strain induced by the lattice mismatch between III-nitride materials and sapphire substrate. Table 1.1 summarizes the spontaneous and piezoelectric polarization for various compositions of III-nitride semiconductors. The total polarization of an III-nitride film is the sum of spontaneous and piezoelectric components. A typical blue LED structure consists of an InGaN quantum well (QW) of lower bandgap sandwiched between GaN barriers of higher

Table 1.1: Spontaneous and piezoelectric polarization of III-nitride materials [14].

Spontaneous polarization (C/m^2)	$P^{sp}_{GaN} = -0.034$
	$P^{sp}_{InN} = -0.042$
	$P^{sp}_{AlN} = -0.090$
	$P^{sp}_{Al_xGa_{1-x}N} = -0.090x - 0.034(1-x) + 0.021x(1-x)$
	$P^{sp}_{In_xGa_{1-x}N} = -0.042x - 0.034(1-x) + 0.037x(1-x)$
	$P^{sp}_{Al_xIn_{1-x}N} = -0.090x - 0.042(1-x) + 0.070x(1-x)$
Piezoelectric polarization (C/m^2)	$P^{pz}_{Al_xGa_{1-x}N/InN} = -0.28x - 0.113(1-x) + 0.042x(1-x)$
	$P^{pz}_{Al_xGa_{1-x}N/GaN} = -0.0525x + 0.0282x(1-x)$
	$P^{pz}_{Al_xGa_{1-x}N/AlN} = 0.026(1-x) - 0.0282x(1-x)$
	$P^{pz}_{In_xGa_{1-x}N/InN} = -0.113(1-x) - 0.0276x(1-x)$
	$P^{pz}_{In_xGa_{1-x}N/GaN} = 0.148x - 0.0424x(1-x)$
	$P^{pz}_{In_xGa_{1-x}N/AlN} = 0.182x - 0.0261(1-x) - 0.0456x(1-x)$
	$P^{pz}_{Al_xIn_{1-x}N/InN} = -0.28x + 0.104x(1-x)$
	$P^{pz}_{Al_xIn_{1-x}N/GaN} = -0.0525x + 0.148(1-x) + 0.0938x(1-x)$
	$P^{pz}_{Al_xIn_{1-x}N/AlN} = 0.182(1-x) + 0.092x(1-x)$

bandgap. Due to the different total polarization for the barriers and QW, the discontinuity in the polarization induces interface charge density that results in a large electric field in the QW. Consequently, severe band bending due to the large electric field leads to charge separation effect in the QW. This charge separation issue gives rise to quantum-confined Stark effect (red shift in the emission from LED) as well as reduces the radiative recombination rate. Several approaches such as band structure engineering [6, 7, 8, 9] and the use of semipolar/nonpolar substrates [10, 11, 12, 13] have been pursued to mitigate the charge separation issue by improving the electron and hole wavefunctions overlap.

On the other hand, significant efforts have also been devoted to enhancing light extraction efficiency ($\eta_{extraction}$) of III-nitride LEDs [15, 16, 17, 18]. According to Snell′s Law, the critical angle (θ_c) for a photon to escape from the GaN layer into the

air is about 24°. As a result, photons generated from conventional planar structure LEDs arrive at the GaN/air interface at an angle larger than 24° will experience total internal reflection and get trapped inside the high refractive index material. For a conventional planar GaN-based LED structure, the $\eta_{extraction}$ has been calculated as ∼4% which is insufficient for realizing high-efficiency solid-state lighting. Moreover, valence subbands crossover at high Al-composition AlGaN QW active region results in dominant TM-polarized output in DUV regime, as illustrated in Figure 1.2. As planar structure favors light extraction from the top/bottom surface (along c-axis) while TM-polarized light tends to emit at large angles with respect to c-axis, majority of TM-polarized output will be trapped inside the planar structure due to total internal reflection, and eventually being re-absorbed by the LED device. Accordingly, various LED designs such as patterned sapphire substrate (PSS) [19, 16, 20, 21, 22], flip chip design [23, 24], micro-dome design [25], nanowire structure [26, 27, 28, 29] and plasmonic devices [30, 31, 32, 33, 34] have been investigated with the intention to enhance photon scattering effect that lead to higher possibility of photons entering photon escape cone in the LED structure and results in enhanced $\eta_{extraction}$.

1.2 Research Work Accomplished

1.2.1 UV LEDs with Patterned Sapphire Substrate

3D finite-difference time-domain (FDTD) simulations have been performed to analyze the light extraction mechanisms for flip-chip UV LEDs with microdome-shaped array patterning on the sapphire substrate. The results show that microdome-shaped PSS is particularly efficient in enhancing transverse-magnetic (TM)-polarized $\eta_{extraction}$ where up to ∼11.2-times and ∼2.6-times improvement can be achieved for 230 nm and 280 nm flip-chip UV LEDs respectively. On the contrary, the use of the microdome-shaped PSS does not lead to enhanced transverse-electric (TE)-polarized $\eta_{extraction}$

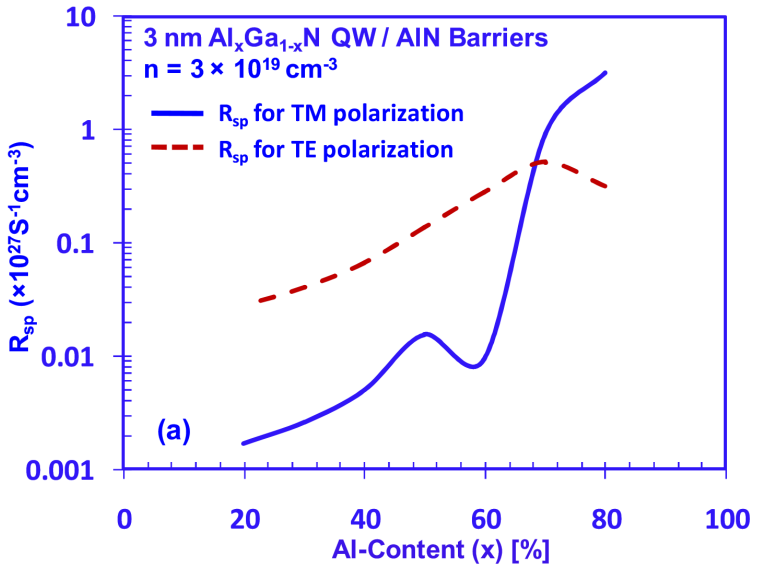

Figure 1.2: TE- and TM-polarized spontaneous emission rate (R_{sp}) for $Al_xGa_{1-x}N$ QW / AlN barriers with various Al-contents (x) in the QW [35].

for the 230 nm and 280 nm flip-chip UV LEDs as the PSS is acting as a reflector that reflects the majority of the TE-polarized light back into the structure.

1.2.2 Nanowire UV LEDs

Nanosphere lithography and KOH-based solution (AZ 400K developer) wet etching have been developed to fabricate III-nitride nanowire LEDs via top-down approach. This study shows that AZ 400K solution with a concentration of 40%, at temperature of 45°C is adequate to achieve smooth nanowires with crystallographic base after etching for 30 minutes. Analysis of the polarization-dependent $\eta_{extraction}$ of AlGaN-based nanowire LEDs in DUV regime has also been investigated using 3D FDTD method. Results show that up to ∼48% TM-polarized $\eta_{extraction}$ and ∼41% TE-polarized $\eta_{extraction}$ can be obtained for 230 nm UV LEDs with nanowire structure as compared to ∼0.2% TM-polarized $\eta_{extraction}$ and ∼2% TE-polarized $\eta_{extraction}$ from conventional planar structure.

1.2.3 Plasmonic Nanowire LEDs

The use of surface plasmon polaritons (SPPs) has been investigated as a means to improve the η_{IQE} and $\eta_{extraction}$ of III-nitride plasmonic LEDs with nanowire structure. In particular, green plasmonic LEDs with nanowire structure coated with Al_2O_3 as a dielectric layer and various Ag cladding layer thicknesses are investigated using 3D FDTD method. The results show that a Purcell factor of ∼80 can be obtained for the investigated plasmonic nanowire LEDs with $\eta_{extraction}$ ∼65% when the Ag thickness > 60 nm. Thinner Ag suffers from lower $\eta_{extraction}$ due to the lower reflectance from the thin metal film despite the fact that higher Purcell factor can be achieved. Strong near-field electric field intensity at the dielectric/metal interface confirms the existence of plasmonic effects in the active region.

1.2.4 3D Printed Lens on InGaN LEDs for White Color Emission

The integration of 3D printed lens with InGaN LED has been proposed as a straightforward and highly reproducible method to improve $\eta_{extraction}$ as well as to achieve white color generation. The use of optically transparent acrylate-based photopolymer with a refractive index of ∼1.5 as a 3D printed lens on blue LEDs has exhibited ∼9% enhancement in the output power at current injection of 4 mA as compared to blue LEDs without 3D printed lens. FDTD analysis on various lens designs also show that up to 1.61-times enhancement in $\eta_{extraction}$ can be obtained. By mixing the photopolymer with YAG:Ce phosphor powder, stable white color emission can be achieved with chromaticity coordinates around (0.27, 0.32) and correlated color temperature ∼8900 K at current injection of 10 mA.

1.2.5 Monolithic White LEDs with Ternary InGaN Substrate

The use of a ternary InGaN substrate for high-efficiency monolithic tunable white LEDs has been investigated. Nanostructure engineering has been conducted in the multiple QW (MQW) active region for LEDs on ternary InGaN substrate to achieve white color illumination. Simulation studies show that by integrating blue- and yellow-emitting InGaN/InGaN MQWs with engineered structures on ternary InGaN substrate, large output power (∼170 mW) and high external quantum efficiency (∼50%) can be achieved for stable white illumination at various current injections at room temperature. The chromaticity coordinates around (0.30, 0.28) and correlated color temperature ∼8200 K at 50 A/cm^2 are also comparable results with those nanostructured white LEDs.

1.3 Dissertation Organization

This dissertation is organized into ten chapters. Chapter 1 presents an overview of III-nitride materials and their applications as well as summarizes the research work accomplished in this dissertation.

Chapter 2 reviews the performance characteristics of III-nitride LEDs and recent approaches to enhance the $\eta_{extraction}$.

Chapter 3 discusses the procedure to fabricate planar structure III-nitride LED devices through standard photolithography steps and reactive ion etching.

Chapter 4 presents the polarization-dependent $\eta_{extraction}$ study for AlGaN-based flip-chip UV LEDs emitting at 230 nm and 280 nm with microdome-shaped patterning on sapphire substrates.

Chapter 5 describes the nanosphere lithography method to fabricate III-nitride nanowires via top-top-down etching, and KOH wet etching in removing the nanowires surface roughness arisen from plasma etch.

Chapter 6 focuses on the polarization-dependent $\eta_{extraction}$ of AlGaN-based 230 nm UV LEDs of various nanowires dimensions and surface passivation layers.

Chapter 7 investigates plasmonic green LEDs with nanowire structure to improve the η_{IQE} and $\eta_{extraction}$ through surface plasmon polaritons.

Chapter 8 proposes the integration of 3D printing technology with InGaN LED as a straightforward and highly-reproducible method to improve $\eta_{extraction}$ and achieve white color emission.

Chapter 9 presents a novel LED structure with the use of ternary InGaN substrate to realize high-efficiency monolithic tunable white LEDs.

Chapter 10 summarizes the research work and discusses the future outlook of III-nitride optoelectronics applications.

Chapter 2

Limitation of Efficiency for III-Nitride LEDs

This chapter discusses the key parameters that characterize the performance of light-emitting diode (LED) as well as the issues associated with low light extraction efficiency of conventional III-nitride LED devices. A review of various approaches to enhance the light extraction is also presented.

2.1 Performance Characteristics of III-Nitride LEDs

An LED is a p-n junction diode that emits light when injected carriers recombine to generate photons [Figure 2.1(a)]. The quantum well (QW) of an LED typically formed by a small band gap layer in a double heterostructure design where the electrons and holes are trapped in the low bandgap layer rather than being distributed along the whole diffusion length, as illustrated in Figure 2.1(b). The radiative recombination process happens in the QW to generate photons where the energy of the photons ($h\nu$) are determined by the band gap (E_g) of the QW, and its relation with the emission

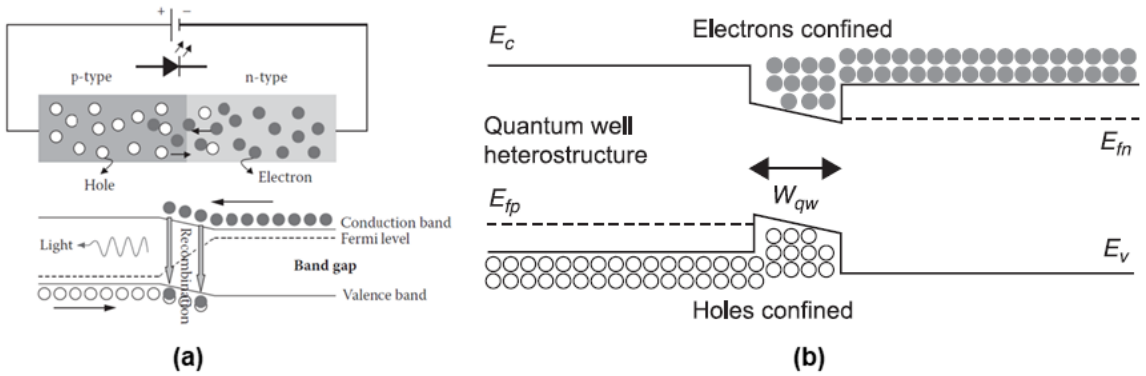

Figure 2.1: (a) Schematic (top) and band diagram (bottom) of an LED [36]; (b) Band diagram of a QW heterostructure showing carrier diffusion and confinement [37].

wavelength (λ) is described as followed:

$$E_g = h\nu = \frac{hc}{\lambda} \tag{2.1}$$

where h is the Planck′s constant and c is the speed of light.

The efficiency of an LED device is typically characterized by external quantum efficiency (η_{EQE}), which is described as a product of injection efficiency ($\eta_{injection}$), radiative recombination efficiency (η_{rad}) and light extraction efficiency ($\eta_{extraction}$), as shown in the following equation:

$$\eta_{EQE} = \eta_{injection} \times \eta_{rad} \times \eta_{extraction} = \eta_{IQE} \times \eta_{extraction} \tag{2.2}$$

The $\eta_{injection}$ describes the ratio of the carriers arrives at the active region to the total carriers being injected into the LED structure through the metal contacts. The η_{rad} is the fraction of the electron-hole pairs that recombine radiatively in the QW. The product of the $\eta_{injection}$ and η_{rad} is called internal quantum efficiency (η_{IQE}), which can possibly be determined by temperature and excitation power-dependent photoluminescence measurements [38]. The $\eta_{extraction}$ is the ratio of photons that can be extracted from the LED structure to the photons that are generated in the

active region. For phosphor-converted white LEDs, the phosphor conversion efficiency ($\eta_{conversion}$) needs to be taking into account when calculating the η_{EQE}, which is described as followed:

$$\eta_{EQE} = \eta_{IQE} \times \eta_{extraction} \times \eta_{conversion} \tag{2.3}$$

In general, there are three types of recombination mechanisms that can occur in the active region of an LED: 1) spontaneous emission process through radiative recombination of electrons and holes to generate photons, 2) non-radiative recombination through defects or traps, and 3) non-radiative Auger recombination that involves many particles. The various recombination processes are shown schematically in Figure 2.2. Thus, the η_{rad} of an LED is expressed by the ratio of radiative recombination rate to the sum of radiative and non-radiative recombination rates:

$$\eta_{rad} = \frac{R_{sp}}{R_{sp} + R_{nr}} \tag{2.4}$$

where R_{sp} is the spontaneous emission rate attributed to the radiative recombination process, and R_{nr} is the sum of non-radiative recombination rate for trap-assisted non-radiative recombination and Auger recombination processes.

Figure 2.3 summarizes the η_{EQE} for III-nitride LEDs that have been reported by various groups as a function of wavelength. Figure 2.3(a) shows the η_{EQE} for commercial nitride-based LEDs in the visible spectrum while Figure 2.3(b) presents the η_{EQE} for AlGaN, AlInGaN and InGaN LEDs emitting in the ultraviolet (UV) spectral range. Relatively high η_{EQE} ($> 50\%$) has been achieved for nitride-based blue and green LEDs attributed to the improved η_{IQE} and $\eta_{extraction}$. However, the η_{EQE} for nitride-based UV is still extremely low compared to its visible counterparts where less than 10% of η_{EQE} has been reported for $\lambda < 300$ nm, and the η_{EQE} further drops to $\sim$1% when λ is below 250 nm [40]. Several factors have been identified to

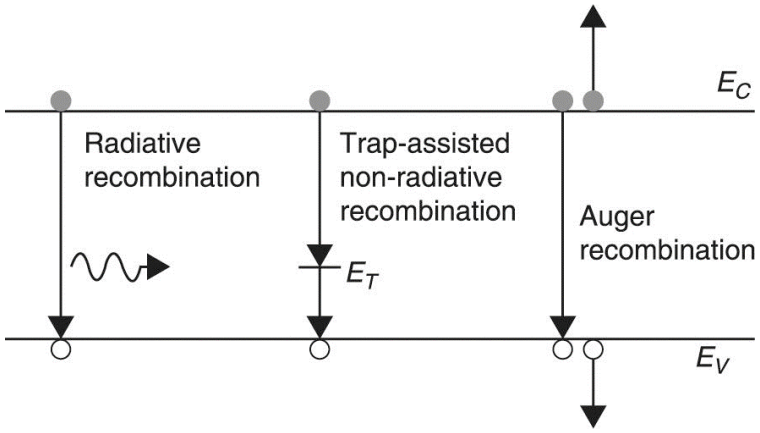

Figure 2.2: Band diagram showing radiative recombination, trap-assisted non-radiative recombination, and Auger recombination processes [37].

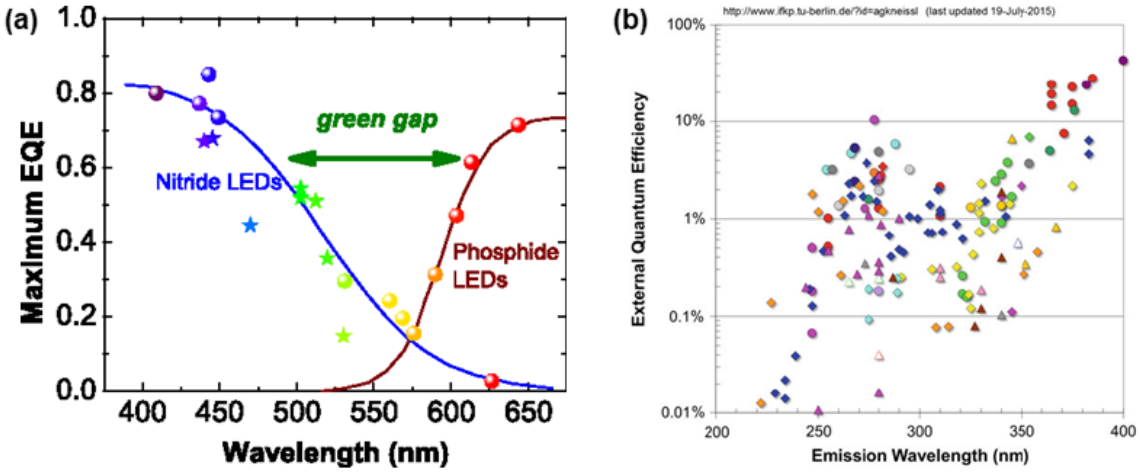

Figure 2.3: External quantum efficiency for (a) nitride- and phosphide-based visible LEDs [39], and (b) nitride-based UV LEDs [40].

contribute to this extremely low UV LED efficiency: 1) difficulties in p-type doping of AlGaN layer, 2) challenges in making good ohmic contact on high Al-content AlGaN layer, 3) large dislocation density from AlGaN materials, and 4) the valence subbands crossover [35, 41, 42, 43, 7] at high Al-composition AlGaN QW active region that results in dominant transverse-magnetic (TM) [$\boldsymbol{E}$ // c-axis] polarized output in DUV regime. Subsequently, extensive works have been focused on thin film growth techniques and novel LED designs to address issues associated with the low η_{EQE} [6,

7, 44, 45, 46, 47, 48, 49, 50]. Despite these continuous efforts, it remains extremely challenging to obtain high $\eta_{extraction}$ from III-nitride LEDs with a planar structure.

2.2 Light Extraction Efficiency of Conventional III-Nitride LEDs

Improving the $\eta_{extraction}$ remains a key challenge for III-nitride LEDs due to the large refractive contrast between III-nitride materials and air. Consequently, photons generated in conventional III-nitride LEDs with the planar structure are subjected to total internal reflection, as illustrated in Figure 2.4. The analysis for total internal reflection can be explained by Snell′s Law:

$$n_{GaN} \sin \theta_{GaN} = n_{air} \sin \theta_{air} \tag{2.5}$$

where n_{GaN} is the refractive index of GaN, θ_{GaN} is the angle of the incident ray, n_{air} is the refractive index of free space, and θ_{air} is the angle of the refracted ray. Total internal reflection occurs when the incident ray is refracted at an angle larger than 90°. By applying $\theta_{air} = 90°$ into Equation 2.5, the critical angle (θ_c) for total internal

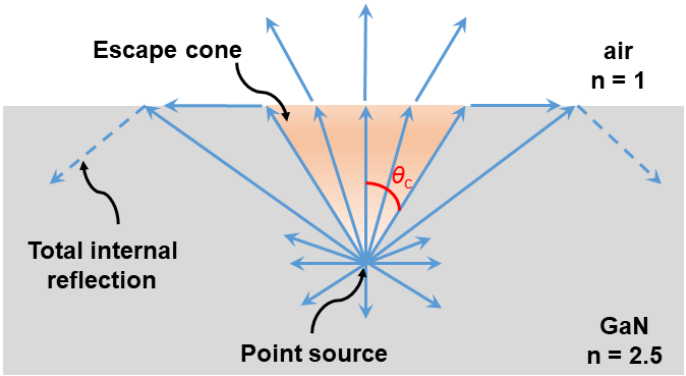

Figure 2.4: Schematic of a planar structure III-nitride LED showing the refraction of light and total internal reflection.

reflection can then be determined as followed:

$$\theta_c = \sin^{-1} \frac{n_{air}}{n_{GaN}} \tag{2.6}$$

By substituting $n_{GaN} = 2.5$ and $n_{air} = 1$ into Equation (2.6), the θ_c for GaN LED is calculated as $\sim$24°. This implies that photons generated in the active region of planar GaN LED arrive at the GaN/air interface at an angle larger than 24° will be trapped inside the LED.

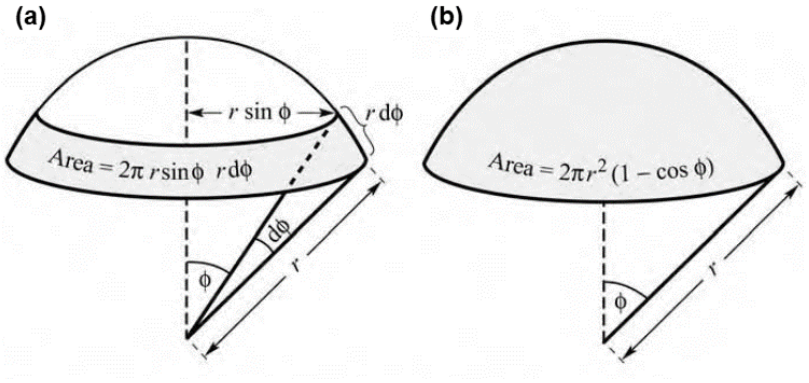

Figure 2.5: (a) Area element (dA) and (b) area of emission sphere defined by radius r and angle ϕ.

The $\eta_{extraction}$ can be determined by the fraction of light travels inside the escape cone, which can be calculated as the ratio of the surface area of a spherical cone with angle θ_c to the surface area of the whole sphere. The emission surface area of an escape cone shown in Figure 2.5 can be expressed as

$$Area = \int_0^{\theta_c} 2\pi r \sin\theta \; r \; d\phi = 2\pi r^2 (1 - \cos\theta_c) \tag{2.7}$$

where r is the radius of the spherical cone. Assuming the light is emitted from a point source with a total power of P_{source}, the fraction of the power that can escape from the planar LED structure (P_{escape}), which also defines the $\eta_{extraction}$ of the LED,

is given by

$$n_{extraction} = \frac{P_{escape}}{P_{source}} = \frac{2\pi r^2(1-\cos\theta_c)}{4\pi r^2} = \frac{1}{2}(1-\cos\theta_c) \tag{2.8}$$

Since the critical angle for GaN is relatively small, the cosine term in Equation 2.8 can be expanded into power series using Taylor′s expansion and neglecting higher-than-second-order terms:

$$n_{extraction} = \frac{1}{2}(1-\cos\theta_c) \approx \frac{1}{2}\left[1-\left(1-\frac{\theta_c^2}{2}\right)\right] = \frac{1}{4}\theta_c^2 = \frac{1}{4}\left(\frac{n_{air}}{n_{GaN}}\right)^2 \tag{2.9}$$

For conventional planar GaN LED, Equation 2.9 suggests that only ∼4% of light generated in the active region can be radiated out from the device. This extremely low $\eta_{extraction}$ is limiting the efficiency of the LED device, and it becomes more severe for DUV LEDs due to dominant TM-polarized output. Therefore, novel designs that can extract more photons from LED structure are essential to enhance to η_{EQE}.

2.3 Approaches to Enhance Light Extraction Efficiency of III-Nitride LEDs

Tremendous efforts have been devoted to enhancing the $\eta_{extraction}$ of III-nitride LEDs. One of the most popular techniques is surface roughening through crystallographic etch [51, 15, 52, 53, 54] where non-uniform surface textures are being formed on the surface of an LED to enhance light scattering and reduces the possibility of total internal reflection. The SEM image in Figure 2.6(a) shows an example of surface texture on GaN LEDs, and the mechanism of light propagation inside an LED with surface texture is illustrated in Figure 2.6(b).

As the surface roughening method typically involves p-GaN layer which is detrimental to holes injection, the use of microstructure arrays with lower refractive

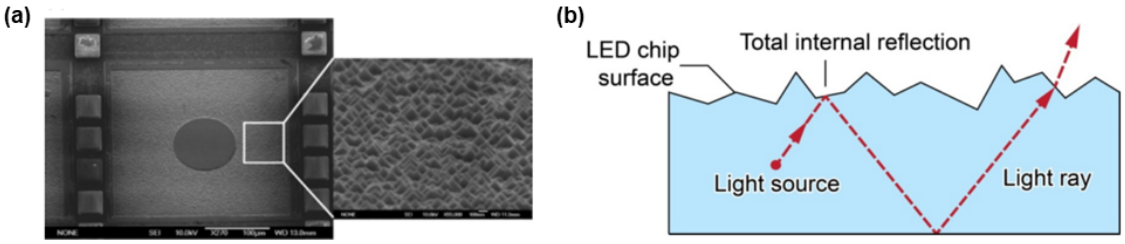

Figure 2.6: (a) SEM image showing rough surface patterning of GaN LEDs [15]. (b) Schematic of light propagation inside an LED with surface texture.

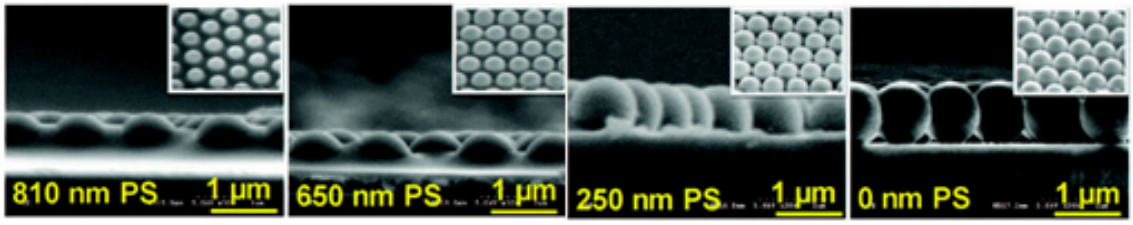

Figure 2.7: SEM images of various PS microstructure arrays designs on LEDs [56].

index materials, such as polystyrene (PS), polydimethylsiloxane (PDMS), SiO_2 spheres and TiO_2 spheres, on top of the LEDs have been proposed as an alternative [17, 55, 56, 57, 58, 59]. Figure 2.7 shows an example of various PS microstructure array designs on LEDs.

The use of patterned sapphire substrate (PSS) has also received significant attention as the patterning on sapphire can help with scattering of light to improve $\eta_{extraction}$ at the same time minimizes dislocation density from epitaxial growth that reduces the possibility of photons trapping in the defect sites [22, 21, 20, 16, 60, 19, 61]. Figures 2.8(a) – 2.8(d) show the SEM of various PSS, and the schematic in Figures 2.8(e) shows an example of an LED fabricated on PSS. The mechanism of light scattering introduced by PSS is very similar to those with surface roughening [Figure 2.6(b)] and microstructure arrays where they all help to mitigate total internal reflection. This is one of the commonly used approaches for commercial III-nitride LEDs in the visible region.

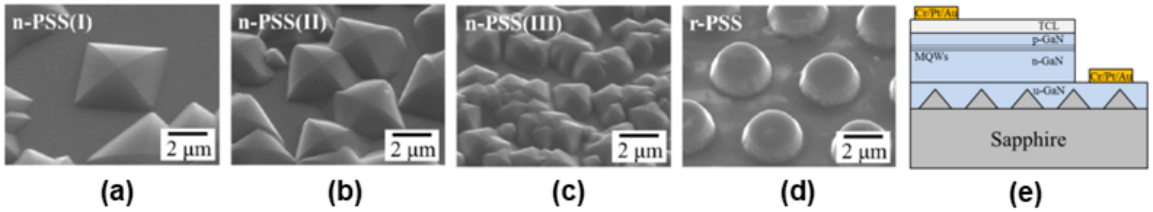

Figure 2.8: (a) – (d) SEM images showing various PSS pattering; and (e) schematic of an LED fabricated on PSS [16].

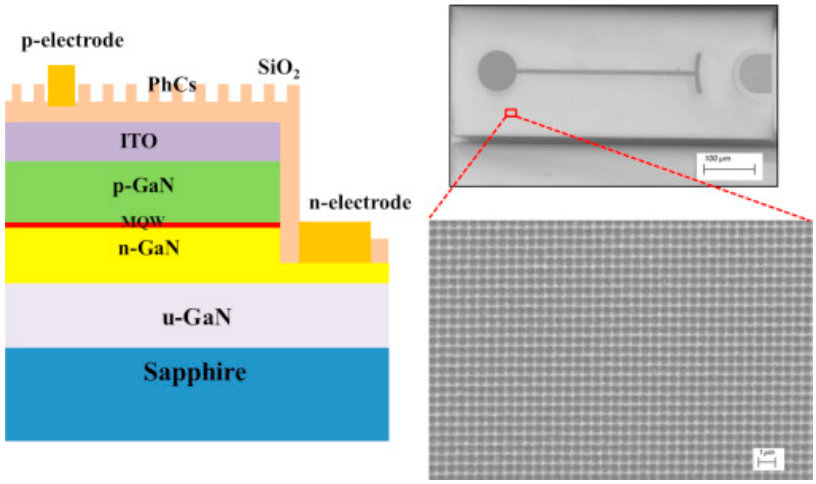

Figure 2.9: Schematic diagram (left) and SEM images (right) of the LED with SiO2 photonic crystal. The enlarged image shows the SiO2 PhCs in the LED chip [62].

A photonic crystal is another commonly used approach to enhance the $\eta_{extraction}$ [62, 6, 64, 65, 18]. The mechanism for the enhancement stems from the photonic bandgap and scattering effects. However, the feature size of photonic crystals is typically in the range of 300 nm to 500 nm, which requires high-cost ebeam lithography or nanoimprint process. Figure 2.9 shows an example of LEDs with SiO_2 photonic crystals. Embedded photonic crystals, for example in the p-GaN and n-GaN layers, have also received significant attention in the past decades for enhancing the $\eta_{extraction}$.

As stated previously, the emission from AlGaN-based mid- and DUV LEDs is primarily TM-dominant. Consequently, many of the light extraction method

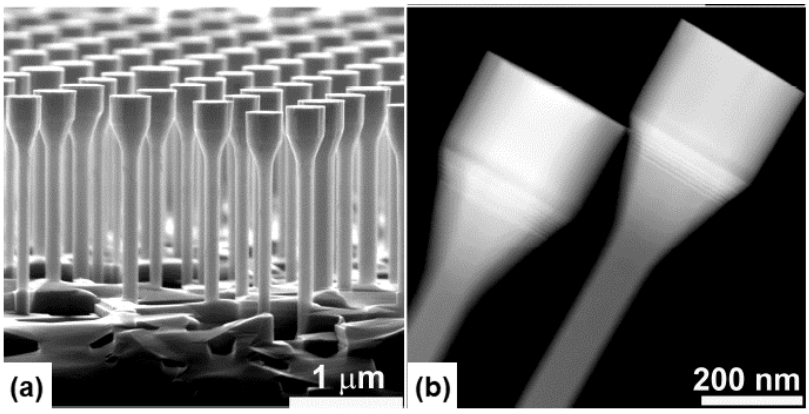

Figure 2.10: (a) SEM image of nanowire LEDs formed through top-down etching. (b) STEM image of nanowires showing the position of InGaN MQWs (bright stripes) [63].

developed for visible or near UV LEDs may not be suitable for these devices. Nanowire structure, on the other hand, has reported to be an excellent candidate for extracting TM-polarized output attributed to its large surface-to-volume ratios [29, 66, 63, 26, 27, 28, 67]. Nanowires structure with a larger surface area than the conventional planar structure can allow more light to escape through the sidewall, which in turn will lead to larger $\eta_{extraction}$. Figure 2.10 shows an example of InGaN nanowires fabricated via top-down etching.

Chapter 3

Fabrication of III-Nitride Planar Structure LEDs

The Semiconductor and Microsystems Fabrication Laboratory (SMFL) at Rochester Institute of Technology (RIT) has never processed any III-nitride materials previously. This chapter presents the fabrication process of nitride-based light-emitting diodes (LEDs) developed utilizing the cleanroom facility at RIT SMFL. Electroluminescence (EL) and photoluminescence (PL) measurements to characterize the fabricated III-nitride LEDs have also been discussed.

3.1 Introduction to Epitaxial Growth of III-Nitride LEDs

The development of III-nitride semiconductors for various applications have been enabled by the advancement in epitaxial growth techniques. In general, molecular beam epitaxy (MBE) and metal-organic chemical vapour deposition (MOCVD) are the two commonly used techniques to grow the LED structure. These two methods

provide single crystalline epitaxy with atomic layer precision, which is particularly important for superlattices and quantum wells.

For MBE process, the thin film is deposited through the reaction of atomic or molecular beams on a heated substrate in a ultra-high vacuum ($\sim 10^{-8}$ to $\sim 10^{-10}$ Torr) chamber. To be more specific, beams of different materials are aimed at a heated substrate to enable the deposition of one atomic layer at a time. The gallium, indium and aluminum beams are created by heating the source of the respective materials in effusion cells while the nitrogen beams are generated by plasma sources. The composition of the III-nitride material is determined by the beam mixing process. The typical growth rate for MBE is 1 Å per second, which can be controlled by varying the source temperature as this will affects the arrival rate of the molecules at the surface. A built-in reflection high-energy electron diffraction system is typically used to monitor the thin film growth process and to optimize the material quality. Since carrier gases are not required during the epitaxial growth, in conjunction with the ultra-high vacuum environment, high purity epitaxy film can easily be obtained.

On the other hand, the MOCVD process involves the chemical reaction of metalorganic precursors and hydrides on a hot substrate surface. Trimethylgallium, trimethylindium and trimethylaluminium are normally used as precursors for gallium, indium and aluminum respectively while ammonia is typically used as a nitrogen source. Hydrogen or nitrogen is used as the carrier gas. By controlling the flow rate of the gases, the growth rate of the epitaxial film can then be controlled easily. The composition of the deposited III-nitride material is determined by the gas phase composition of the precursors. *In situ* monitoring systems, such as for measuring reflectance, temperature and radius of curvature of the wafer, can be implemented to analyze and control growth parameters. As opposed to the MBE process, the ultra-high vacuum environment is not required for the MOCVD process. As a result, the thin film deposition can occur at high pressure of $\sim$1 Torr.

The higher growth rate by the chemical reaction in MOCVD as compared to physical deposition in MBE has made it a more popular system for mass production.

3.2 Fabrication of Planar Structure LEDs

The fabrication of III-nitride LEDs has been carried out at RIT for the first time. MOCVD-grown InGaN/GaN multiple quantum wells (MQWs) blue LED epi wafers obtained from collaborator are fabricated into devices in the SMFL at RIT. Figure 3.1 shows the layer structure of the blue LED grown on a c-plane sapphire substrate. The LED structure consists of a 2.5-μm silicon-doped n-GaN layer, followed by six periods of 2.5-nm InGaN quantum well and 10-nm GaN quantum barrier, and capped with a 200-nm magnesium-doped p-GaN layer. The doping concentration for the n- and p-doped GaN is 10^{18} cm^{-3} and 10^{17} cm^{-3} respectively.

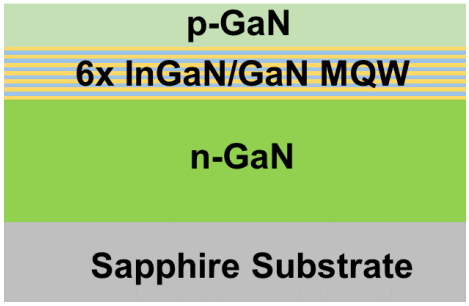

Figure 3.1: Schematic showing the layer structure of InGaN/GaN blue LED.

The fabrication process flow of planar structure top-emitting nitride-based LEDs is summarized in Figure 3.2. First of all, the blue epi-wafer is cleaved into smaller pieces and then rinsed with acetone, isopropyl alcohol (IPA) and deionized (DI) water. Next, $\sim$1 μm OiR-620 positive photoresist is spin coated uniformly on the wafer piece at the speed of 2500 revolutions per minute (rpm) and subsequently soft-bake at 93°C for 1 minute. The spin-coating recipe of OiR-620 on GaN pieces was modified from existing coating recipes for 4 to 6 inches Si wafers.

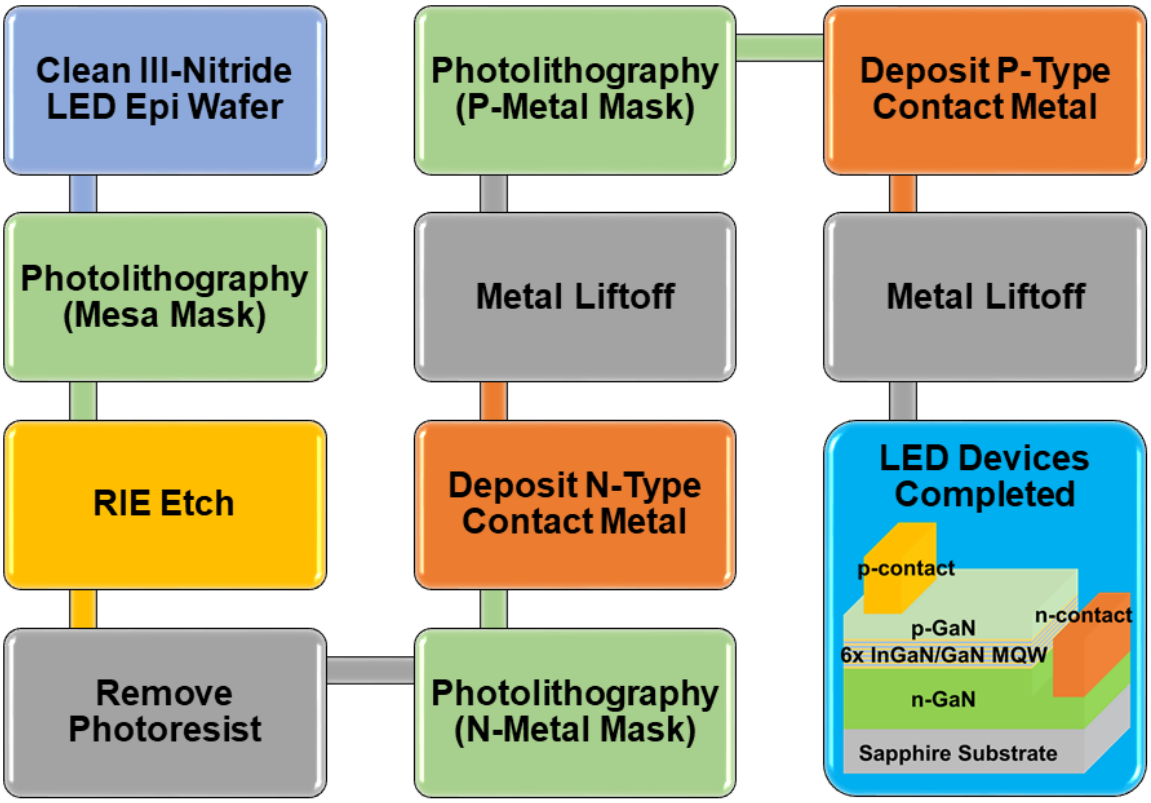

Figure 3.2: Process flow for fabricating top-emitting III-nitride planar LED devices.

Next, the sample coated with photoresist is exposed to ultraviolet (UV) light to define the mesa pattern on the photoresist. Karl Suss MA56 contact mask aligner with mercury lamp is used for the UV exposure. For the measured light intensity of 5.9 mW/cm^2, the sample is exposed to 365 nm UV light for 37 seconds, followed by post-exposure bake at 112°C for 1 minute. The photoresist is then developed in CD-26 for 1 minute to exposure the region on the wafer piece that to be etched away, followed by hard bake at 145°C for 1 minute.

Afterwards, the sample is loaded into reactive ion etcher (RIE) to create mesa patterns on the LED wafer piece. LAM 4600 aluminum etcher is used to perform the etch. The etch recipe was modified from an existing aluminum etch recipe [68]. The flow rates of chlorine and argon gases are determined based upon literature recommendation to keep the etch rate high while maintaining a low surface roughness

on the etched GaN region. During the etch, gases composed of 30 standard cubic centimeter per minute (sccm) of Cl_2, 25 sccm of BCl_3, 8 sccm of $CHCl_3$ and 20 sccm of Ar are flowing into the chamber with RF power of 125 W and a chamber pressure of 100 mTorr. The etch rate is determined as ∼20 nm/min for GaN and ∼50 nm/min for the OiR-620 photoresist. After the etch, the sample is soaked in acetone for ∼10 minutes to remove the remaining photoresist on the substrate, followed by DI water rinsing.

Then, the sample is spin coated with LOR-10A lift-off resist and S1813 positive photoresist to prepare for n-contact metal mask photolithography. The LOR-10A is coated at the speed of 3000 rpm followed by soft-bake at 180°C for 6 minutes while the S1813 is coated at the speed of 3000 rpm followed by soft-bake at 115°C for 1 minute. After that, the sample is aligned with n-contact metal mask using contact mask aligner followed by UV light exposure for 32 seconds. A post-exposure bake is then performed at 95°C for 4 minutes. Next, the photoresist is developed in CD-26 for 2 minutes and 30 seconds followed by DI water rinsing. 20 nm Ti / 200 nm Au metal stack that acts as n-contact metal is evaporated on the substrate using PVD 75 thermal evaporator. After metal deposition, the sample is soaked in PG Remover overnight to lift-off the excess metal. Afterwards, the fabrication steps from spin-coating of lift-off resist to metal liftoff are repeated for p-contact metal, except that 20 nm Ni / 200 nm Au metal stack is evaporated as the p-contact metal. Rapid thermal annealing is not performed after metal deposition as of now due to contamination in the rapid thermal process (RTP) chamber. Nevertheless, the previous investigation on dummy GaN samples with 50 nm Ti on top has exhibited fairly low contact resistance (1.0 – 1.4 kΩ) [68], which imply that the metal stacks without annealing can be used as metal contacts for the LED devices.

The masks are designed using Tanner L-Edit IC Layout, which is a commercial software commonly used for mask design. Figure 3.3(a) illustrated the mask patterns

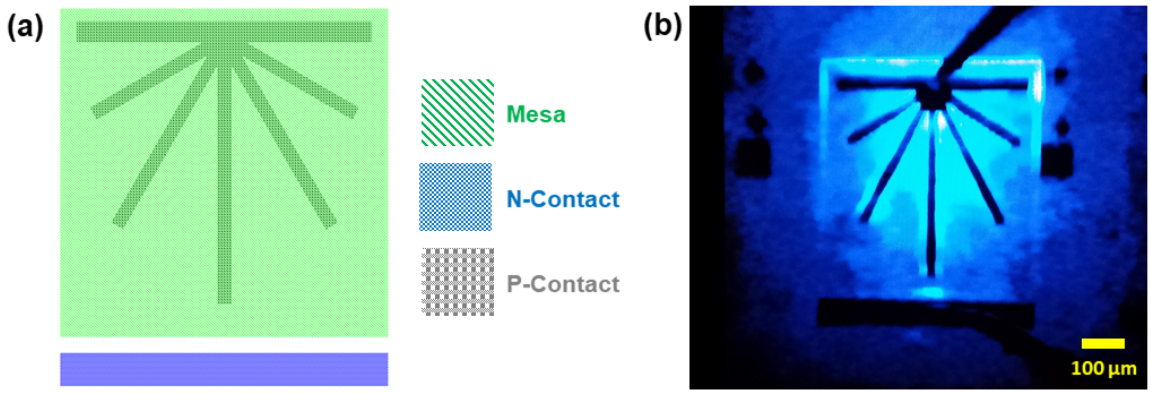

Figure 3.3: (a) Mask design of mesa, n-contact and p-contact for top emitting LED. (b) Photomicrograph of blue LED fabricated in house.

for mesa, n-contact and p-contact. The dimension of the mesa pattern is 500 μm by 500 μm, corresponding to an area of 0.25 mm^2 for each LED device. Figure 3.3(b) shows the photomicrograph of blue LED fabricated at current injection level of 4 mA.

3.3 Device Characterizations

3.3.1 Photoluminescence

Before fabricating the-epi wafer piece into LED devices, photoluminescence (PL) has been used to investigate the purity and crystalline quality of the blue LED. PL is a characterization technique that excites semiconductor by absorbing photons with energy larger than the semiconductor bandgap, and then re-emit them at different wavelength. In general, the photons absorbed by the semiconductor will form electrons and holes at higher energy states in the conduction band and valence band respectively, and then undergo relaxation towards bandgap minimum, and finally recombine to emit photons with energy corresponding to the bandgap of the semiconductor bandgap.

The PL setup is shown in Figure 3.4. The excitation source is a 325 nm transverse mode HeCd laser, and a CCD detector with quantum efficiency above 50% for spectral

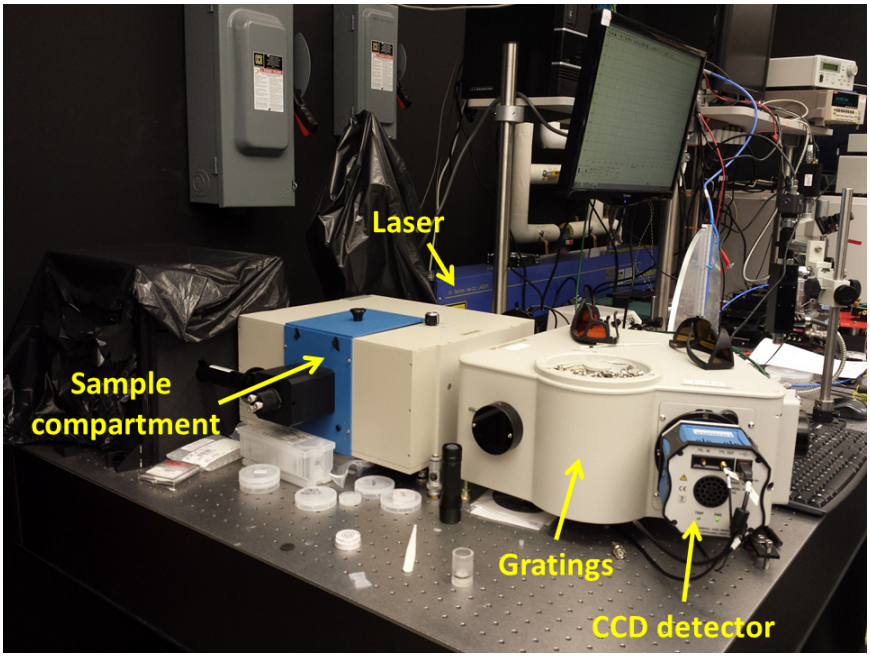

Figure 3.4: Horiba iHR320 PL system.

ranges from 200 nm to 850 nm is used to collect the emitted photons. Figure 3.5 shows the PL intensity of the blue LED with laser beam incident the sample at angle 45°. The distinct peak emission wavelength observed at ∼450 nm with a narrow full-width half maximum of ∼20 nm indicates high material purity in the active region of the blue LED. In addition, negligible defect peak at ∼550 nm as compared to the 450 nm blue emission peak also demonstrates good crystalline quality for the blue LED.

3.3.2 Electroluminescence

Electrical characterizations including current-voltage (IV) measurement, angle-dependent electroluminescence (EL) measurement and light output power measurement have been performed after the blue LED devices are fabricated. A custom-built system has been used for the electrical characterizations. Figure 3.6(a) shows the setup of angle-dependent EL measurement and Figure 3.6(b) shows the close-up view of the EL measurement setup. Optical fiber connected to Ocean

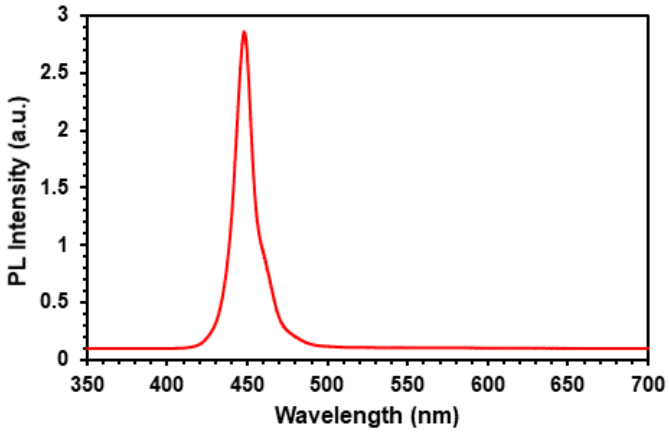

Figure 3.5: PL intensity of InGaN/GaN blue LED.

Optics spectrometer is used to collect the photons emitted from the blue LED devices. The setup for light output power measurement is shown in Figure 3.6(c) where a silicon detector placed at ∼2 cm above the sample is used for the power measurement.

Figure 3.7(a) plots the IV curve and light output power for the fabricated blue LED while the angle-dependent EL measurement result at current injection of 4 mA is presented in Figure 3.7(b). The turn-on voltage of ∼3 V [Figure 3.7(a)] and Lambertian emission pattern [Figure 3.7(b)] show that the fabricated blue LED has similar electrical properties reported in the literature for planar structure InGaN/GaN blue LEDs [69]. This implies that the LED fabrication process developed in the cleanroom at RIT is not detrimental to the LED structure.

3.4 Conclusion

In summary, the etch recipe for III-nitride materials has been developed, and the first planar structure top-emitting InGaN/GaN blue LED devices have been successfully fabricated for the first time at RIT cleanroom. A turn-on voltage of ∼3 V and Lambertian emission pattern can be observed from the fabricated blue LED devices.

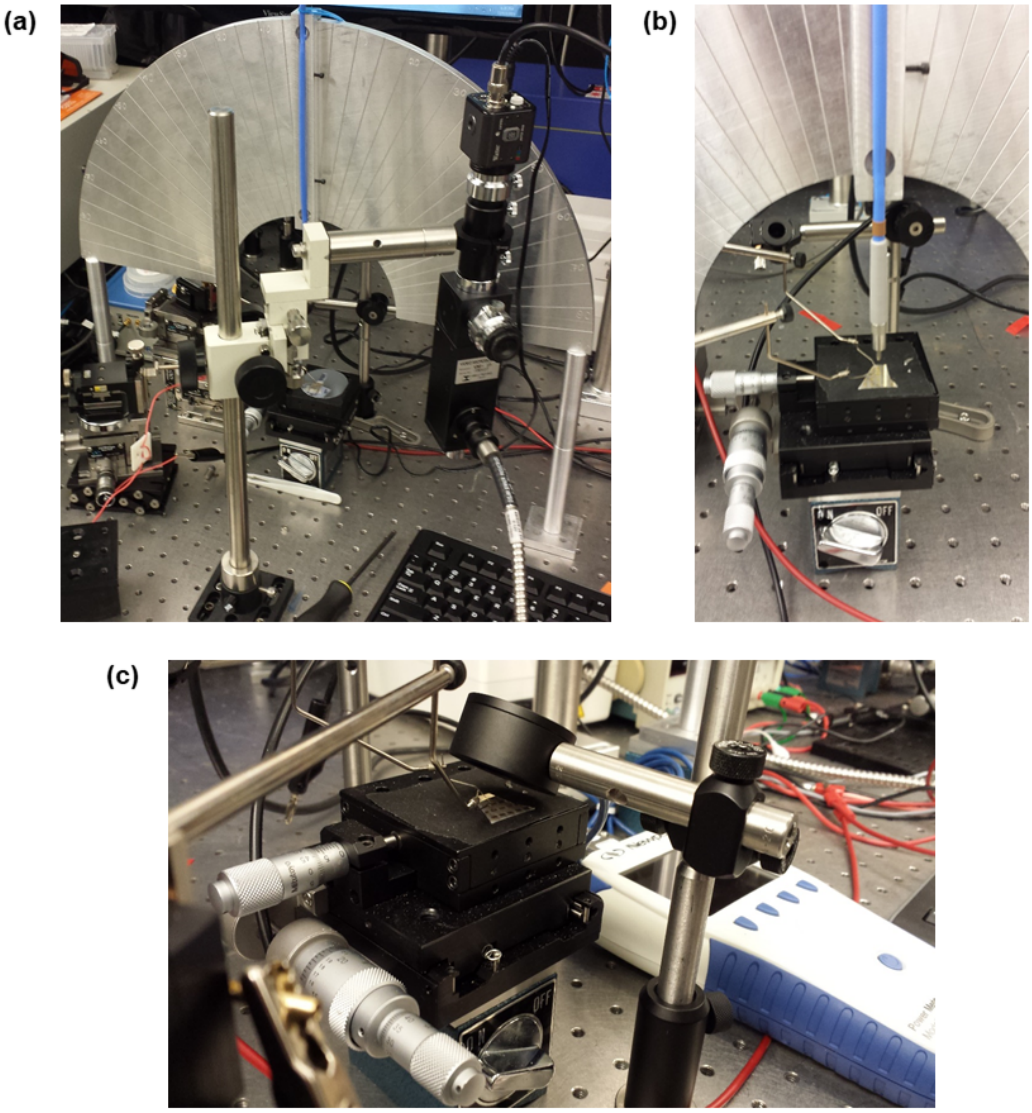

Figure 3.6: (a) Setup for angle-dependent EL measurement; (b) close-up view of the EL measurement setup showing sample stage holder, probes and optical fiber for light intensity measurement; (c) close-up view of the EL measurement setup showing sample stage holder, probes and silicon detector for light output power measurement.

Further optimization of the etch recipe for various device structures, such as nanowire, is necessary as the current etch recipe does not examine the sidewall damage arisen from the ion bombardment during RIE.

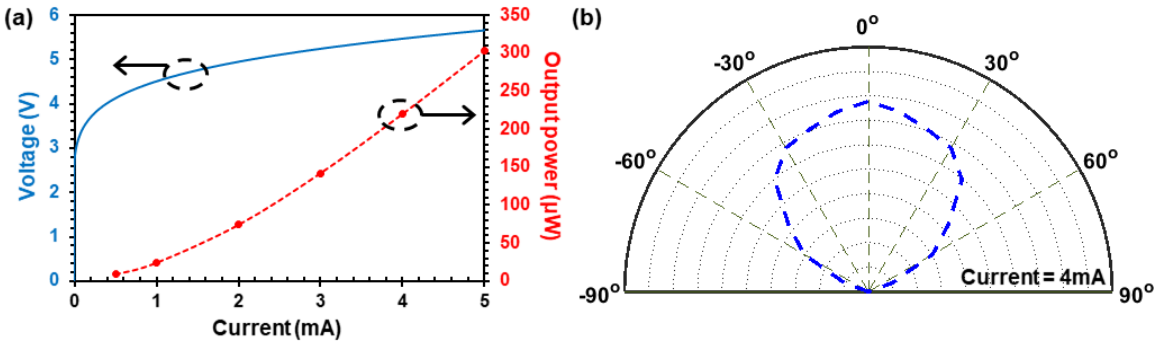

Figure 3.7: (a) IV curve and output power versus current injection for blue LED; (b) angle-dependent EL measurement for blue LED at current injection of 4 mA.

Chapter 4

III-Nitride UV LEDs with Patterned Sapphire Substrate

In this chapter, polarization-dependent light extraction efficiency ($\eta_{extraction}$) of AlGaN-based flip-chip ultraviolet (UV) light-emitting diodes (LEDs) emitting at 230 nm and 280 nm with microdome-shaped patterning on the sapphire substrate has been investigated using three-dimensional (3D) finite-difference time-domain (FDTD) method. Three types of patterned sapphire substrates (PSSs) have been analyzed: bottom-side PSS, top-side PSS and double-sided PSS. Simulation results show that microdome-shaped patterning on the sapphire substrate is predominantly beneficial in enhancing transverse-magnetic (TM)-polarized output. Specifically, TM-polarized $\eta_{extraction}$ enhancement of up to ∼4.5-times and ∼2.2-times can be obtained for 230 nm and 280 nm UV LEDs with bottom-side PSS respectively, and ∼6.3-times and ∼1.8-times for 230 nm and 280 nm UV LEDs with top-side PSS respectively. By employing double-sided PSS, up to ∼11.2-times and ∼2.6-times enhancement in TM-polarized $\eta_{extraction}$ can be achieved for 230 nm and 280 nm UV LEDs respectively. In contrast, the microdome-shaped PSS act as a reflector for

transverse-electric (TE)-polarized photons which leads to severe limitation in light extraction for both 230 nm and 280 nm flip-chip UV LEDs.

4.1 Introduction

The use of PSS has received significant attention due to reduced fabrication complexities, and minimized dislocation density from epitaxial growths, which reduces the possibility of photons trapping in the defect sites [19, 61]. Recent experimental work on 282 nm AlGaN-based UV LEDs with nano-PSS has reported 3.45% of external quantum efficiency (η_{EQE}) (∼98% enhancement as compared to LED with flat sapphire surface) [19] while experimental study on 275 nm flip-chip UV LEDs with PSS has recorded maximum η_{EQE} >16% (∼4-times larger than flip-chip LED with flat sapphire substrate) [21]. In spite of these encouraging experimental results, there has been very limited works exploring the polarization-dependent $\eta_{extraction}$ for flip-chip UV LEDs with PSS, which is particularly important for AlGaN-based UV LEDs as emission from AlGaN quantum wells (QWs) with $\lambda < 230 - 240$ nm is primarily TM [$\boldsymbol{E} \parallel$ c-axis] dominant whereas $\lambda < 250$ nm is mostly TE [$\boldsymbol{E} \perp$ c-axis] dominant [35, 41].

In this work, the light extraction mechanisms for flip-chip UV LEDs with microdome-shaped array patterning on the sapphire substrate has been examined using the 3D FDTD method. The patterning of the sapphire substrate on the bottom-side (the epitaxial growth side) has been commonly used in experimental work to minimize dislocation density [19, 61] but very limited work has been devoted to investigating the effect of PSS on the $\eta_{extraction}$, particularly the top-side and double-sided patterning on the sapphire substrate. Therefore, this study focuses on the polarization dependence $\eta_{extraction}$ of 230 nm (typically TM-dominant emission peak [35, 29]) and 280 nm (typically TE-dominant emission peak [35])

AlGaN-based flip-chip UV LEDs with microdome-shaped array patterning on bottom-side, top-side and double-sided of a sapphire substrate arranged in a hexagonal pattern.

4.2 Numerical Simulation of UV LEDs with Patterned Sapphire Substrate

The $\eta_{extraction}$ for AlGaN-based multiple QW (MQW) flip-chip UV LEDs emitting at 230 nm and 280 nm with microdome-shaped array patterning on sapphire substrate have been investigated using 3D FDTD method, which is commonly used in analyzing the optical properties of III-nitride emitters [23, 24, 25, 29, 67, 70, 71]. The layer structure of the UV LEDs used in the simulations are illustrated in Figure 4.1, which consist of 500 nm sapphire substrate, 200 nm AlN buffer layer, 100 nm n-AlGaN layer, 50 nm thick AlGaN layer to represent the MQW active region, 15 nm p-AlGaN electron blocking layer (EBL), 10 nm p-AlGaN layer and 20 nm p-GaN contact layer. A metallic layer that acts as a perfect mirror is attached to the bottom of the LED to reflect all photons incident upon it. Figure 4.1(a) shows the UV LED with microdome-shaped array patterning on the bottom surface of sapphire substrate, Figure 4.1(b) shows the UV LED with microdome-shaped array patterning on the top surface of sapphire substrate, and Figure 4.1(c) shows the UV LED with microdome-shaped array patterning on both sides of sapphire substrate. The microdomes with diameter D, height H, and spacing S, are arranged in a hexagonal pattern on the sapphire substrate, as depicted in Figure 4.1 (d). Since this work focuses on comparing the $\eta_{extraction}$ for UV LEDs with various positions of the microdome-shaped array on a sapphire substrate, only D is set as a variable in the study while H and S are fixed at 50 nm and 100 nm respectively. The values for H and S are determined from our internal comprehensive analysis where the TM-polarized $\eta_{extraction}$ drops

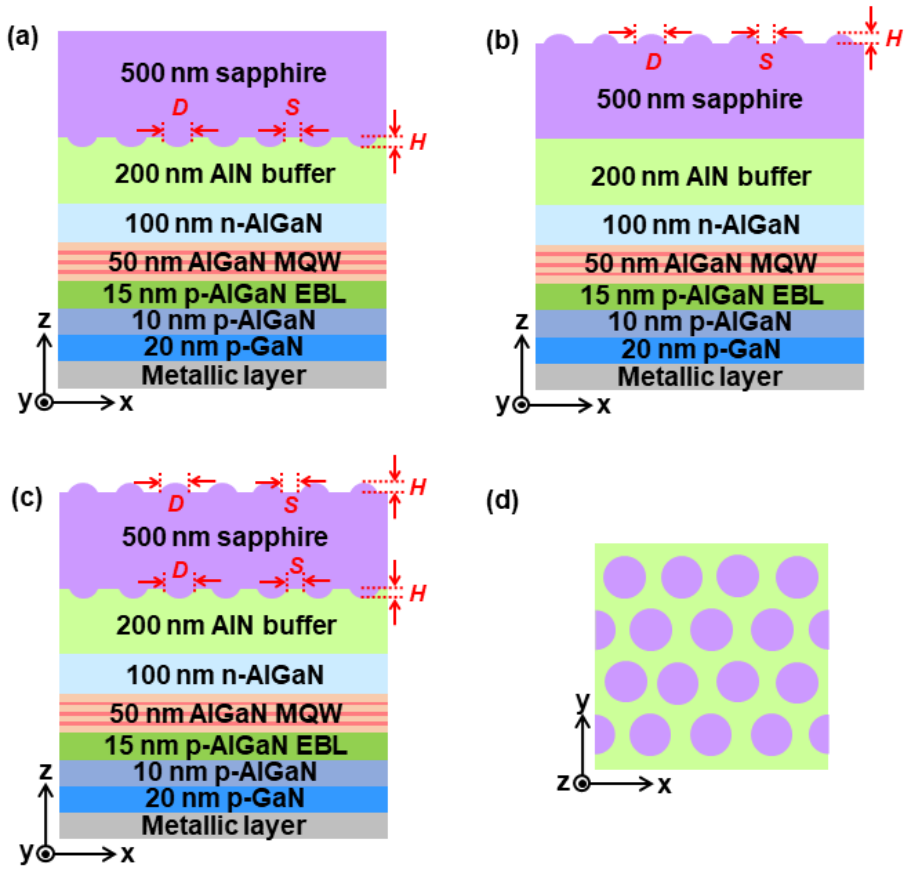

Figure 4.1: Schematic side view of simulated AlGaN-based flip-chip UV LED with microdome-shaped array patterning on (a) bottom-side, (b) top-side and (c) double-sided of a sapphire substrate. The diameter, spacing and height of the microdomes are labeled as D, S, and H respectively. (d) Top view showing the microdome-shaped array on a sapphire substrate arranged in a hexagonal pattern.

substantially to <10% when S > 100 nm while larger H will result in significantly improved $\eta_{extraction}$. However, considering the practicality and complexity in forming taller microdomes on the sapphire substrate during the fabrication process, $H = 50$ nm is chosen in this study.

The refractive indexes and absorption coefficients for AlN, GaN and sapphire are taken from Refs. [23, 72, 73]. Linear extrapolation between AlN and GaN is used in calculating the refractive indexes and absorption coefficients for ternary AlGaN layers where the Al-content for the corresponding emission wavelength are determined from Ref. [74]. To be more specific, the Al composition for 230 nm emission wavelength is

deduced as 98% for p-AlGaN EBL, 77% for AlGaN MQW, and 86% for both the n- and p-AlGaN while for 280 nm emission wavelength is deduced as 93% for p-AlGaN EBL, 42% for AlGaN MQW, and 64% for both the n- and p-AlGaN. As 3D FDTD simulation consumes a large amount of memory and computation time, the simulation domain is set to 5 μm $\times$ 5 μm in the lateral direction in order to ensure computation efficiency. A non-uniform grid size of 10 nm in the bulk and 5 nm near the edges is used in the simulation. The perfectly matched layer boundary condition is applied to the lateral and top boundaries while perfect electric conductor boundary condition is applied to the bottom boundary. A single dipole source is placed at the center of the AlGaN MQW active region where TE-polarization is defined as the major electric field travels in the in-plane direction (parallel to the x and y directions labeled in Figure 4.1) while TM-polarization is represented by the major electric field travels in the out-of-plane direction (parallel to the z direction labeled in Figure 4.1). Single dipole source is used in this work as the use of multiple dipole sources will result in non-physical interference pattern [75], which is undesirable for analysis of the optical properties of LEDs. A source power monitor surrounding the dipole source is used to measure the total power monitor generated in the active region while one output power monitor is placed at distance λ away from the sapphire top surface to measure the light output power radiated out of the LED structure. The $\eta_{extraction}$ is calculated as the ratio of the light output power measured by the output power monitor to the total power dissipated by the dipole source in the active region [23, 71]. A two-dimensional (2D) field monitor has also been placed at the center of the XZ plane defined in Figure 4.1 to record the propagation of the electric field for the simulated structure.

4.2.1 Flip-Chip UV LEDs with Flat Sapphire Substrate

Flip-chip UV LED with a flat sapphire substrate is first being investigated as a reference in this work. For 280 nm UV LED, the calculated TM- and TE-polarized $\eta_{extraction}$ is ∼0.74% and ∼13% respectively. As spontaneous emission from 280 nm AlGaN QW is largely TE-polarized [29], high η_{EQE} is expected from the 280 nm flip-chip UV LED with a flat sapphire substrate. Thus, the study on the effect of PSS to the polarization-dependent $\eta_{extraction}$ for 280 nm flip-chip UV LEDs is essential to further enhance the η_{EQE} and for realizing high efficiency mid-UV LEDs.

On the other hand, for 230 nm UV LED, the calculated TM-polarized $\eta_{extraction}$ is ∼0.13% while the calculated TE-polarized $\eta_{extraction}$ is ∼13%. Although significantly larger TE-polarized $\eta_{extraction}$ can be obtained from planar UV LED with a flat sapphire substrate, the TM-polarized output at 230 nm is ∼20-times higher than the TE-polarized output [29]. As TM-polarized light is primarily propagating in the lateral direction, a very limited amount of photons can be extracted from the top and bottom sides of the device, which results in extremely low TM-polarized $\eta_{extraction}$. Consequently, it is very challenging to achieve high η_{EQE} for conventional planar structure 230 nm UV LEDs. Therefore, it is strongly motivated to investigate the polarization-dependent $\eta_{extraction}$ of 230 nm flip-chip UV LEDs with PSS in order to further improve the TM-polarized $\eta_{extraction}$.

4.2.2 Flip-Chip UV LEDs with Microdome-Shaped Patterning on Bottom Side of Sapphire Substrate

The $\eta_{extraction}$ for flip-chip UV LEDs with microdome-shaped array on the bottom surface of the sapphire substrate is plotted in Figure 4.2 as a function of *D*. Figures 4.2(a) and 4.2(b) present the $\eta_{extraction}$ of flip-chip UV LEDs with microdome-shaped patterning on the bottom surface of sapphire substrate for 230

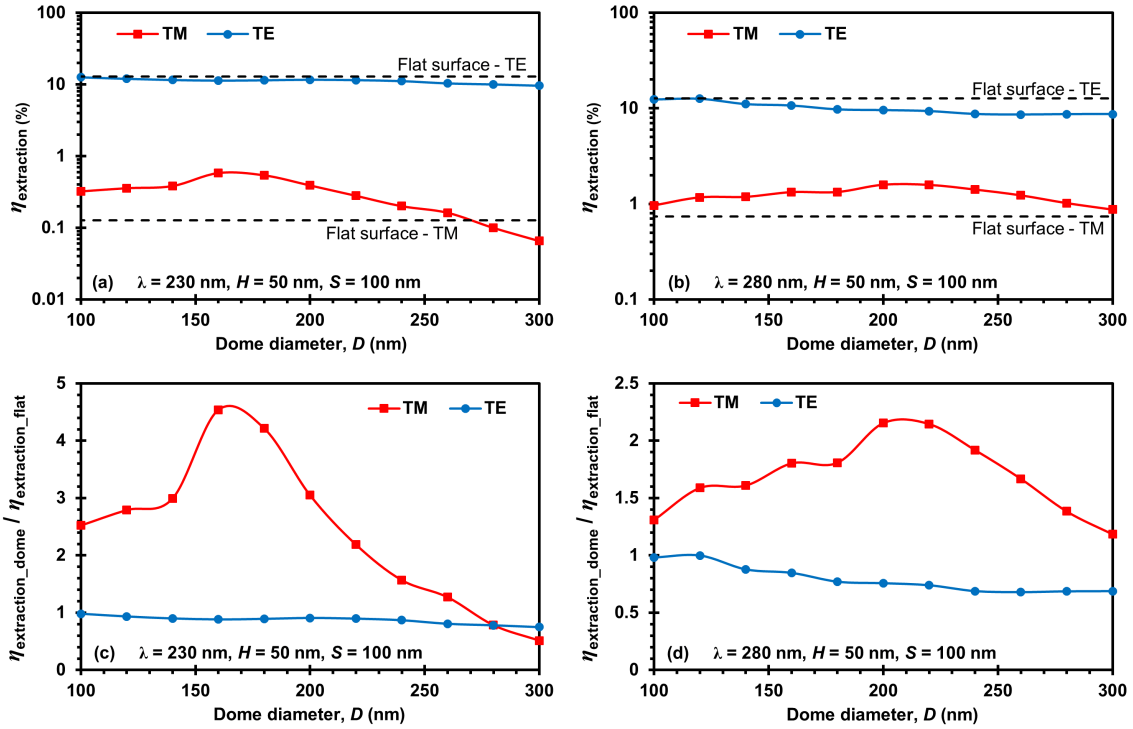

Figure 4.2: The $\eta_{extraction}$ for AlGaN-based flip-chip UV LEDs with bottom side PSS at (a) $\lambda = 230$ nm and (b) $\lambda = 280$ nm as a function of D. The $\eta_{extraction}$ for UV LEDs with a flat sapphire substrate are represented by the black dashed lines. Ratio of the $\eta_{extraction}$ for UV LEDs with bottom-side PSS ($\eta_{extraction\_dome}$) to the $\eta_{extraction}$ for flip-chip UV LEDs with flat sapphire substrate ($\eta_{extraction\_flat}$) for (c) $\lambda = 230$ nm and (d) $\lambda = 280$ nm as a function of D.

nm and 280 nm respectively. The $\eta_{extraction}$ for conventional flip-chip UV LEDs with a flat sapphire substrate is also plotted for comparison purpose. As illustrated in Figures 4.2(a) and 4.2(b), the TE-polarized $\eta_{extraction}$ for both 230 nm and 280 nm UV LEDs are consistently higher than TM-polarized $\eta_{extraction}$ (>1 order of magnitude) when D changes from 100 nm to 300 nm. For instance, the ratios between TE and TM polarizations are observed as ~40-times and ~13-times for 230 nm and 280 nm UV LEDs respectively when $D = 100$ nm, and ~20-times and 8-times for 230 nm and 280 nm UV LEDs respectively when $D = 160$ nm. Since TM-polarized light tends to emit at large angles with respect to c-axis (parallel to the z direction labeled in Figure 4.1) while the planar LED structure favors light

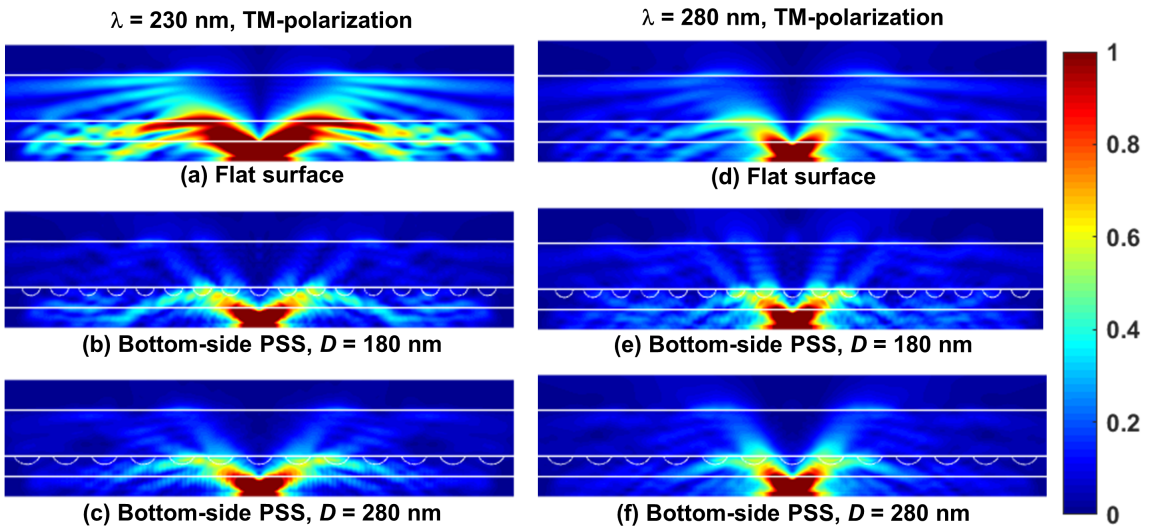

Figure 4.3: Cross-sectional near-field electric field intensity of 230 nm [(a) – (c)] and 280 nm [(d) – (f)] TM-polarized flip-chip UV LEDs with flat sapphire substrate [(a) & (d)], bottom-side PSS with D = 180 nm [(b) & (e)], and bottom-side PSS with D = 280 nm [(c) & (f)].

extraction along c-axis, majority of the TM-polarized output is trapped inside the LED structure which results in lower TM-polarized $\eta_{extraction}$ as compared to TE-polarized $\eta_{extraction}$ for both emission wavelengths.

Despite lower TM-polarized $\eta_{extraction}$ than TE-polarized $\eta_{extraction}$ is observed, the TM-polarized $\eta_{extraction}$ for both 230 nm and 280 nm UV LEDs with bottom-side PSS demonstrate strong dependence on the microdome diameter as D changes from 100 nm to 300 nm. The use of PSS could act as extractor or reflector, depending on the ratio of light being scattered out of the structure to light being scattered back into the structure. When the fraction of light being scattered out of the structure is larger than the fraction of light being scattered back into the structure, the PSS serves as an extractor which could lead to enhanced $\eta_{extraction}$. Otherwise, the PSS will serve as a reflector that inhibits light extraction through the sapphire substrate. From the results presented in Figure 4.2, the microdome-shaped array on the bottom side of the sapphire substrate with $D < 280$ nm acting more like an extractor for TM-

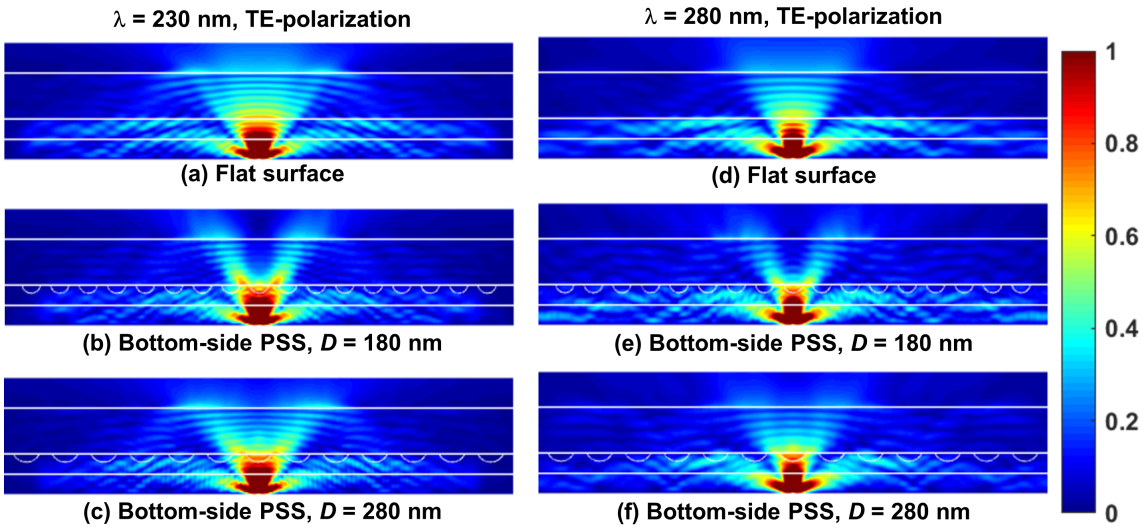

Figure 4.4: Cross-sectional near-field electric field intensity of 230 nm [(a) – (c)] and 280 nm [(d) – (f)] TE-polarized flip-chip UV LEDs with flat sapphire substrate [(a) & (d)], bottom-side PSS with D = 180 nm [(b) & (e)], and bottom-side PSS with D = 280 nm [(c) & (f)].

polarized photons but as a reflector for TE-polarized photons. This is evidenced in the cross-sectional near-field electric field intensity plots shown in Figures 4.3 and 4.4 for TM and TE polarizations respectively. The electric field intensity distribution for UV LEDs with a flat sapphire substrate [Figures 4.3(a) and 4.4(a) for 230 nm UV LEDs and Figures 4.3(d) and 4.4(d) for 280 nm UV LEDs] are also plotted for comparison. The cross-sectional electric field intensity plots clearly illustrated strong photons scattering caused by the microdome-shaped PSS in both the 230 nm and 280 nm UV LEDs. In particular, the PSS acts as an extractor for TM-polarized light [Figures 4.3(b), 4.3(c), 4.3(e) and 4.3(f)] and as a reflector for TE-polarized light [Figures 4.4(b), 4.4(c), 4.4(e) and 4.4(f)]. As a result, up to ∼4.5-times and ∼2.2-times enhancement in TM-polarized $\eta_{extraction}$ can be obtained for 230 nm and 280 nm UV LEDs with bottom-side PSS respectively while lower TE-polarized $\eta_{extraction}$ for UV LEDs with bottom-side PSS than with flat sapphire substrate is observed for both 230 nm and 280 nm when D changes from 100 nm to 300 nm [Figures 4.2(c)

and 4.2(d)]. Specifically, for TM-polarization, the peak $\eta_{extraction}$ enhancement is observed when D is ∼70 – 80 nm below the emission wavelength for flip-chip UV LEDs with bottom-side PSS.

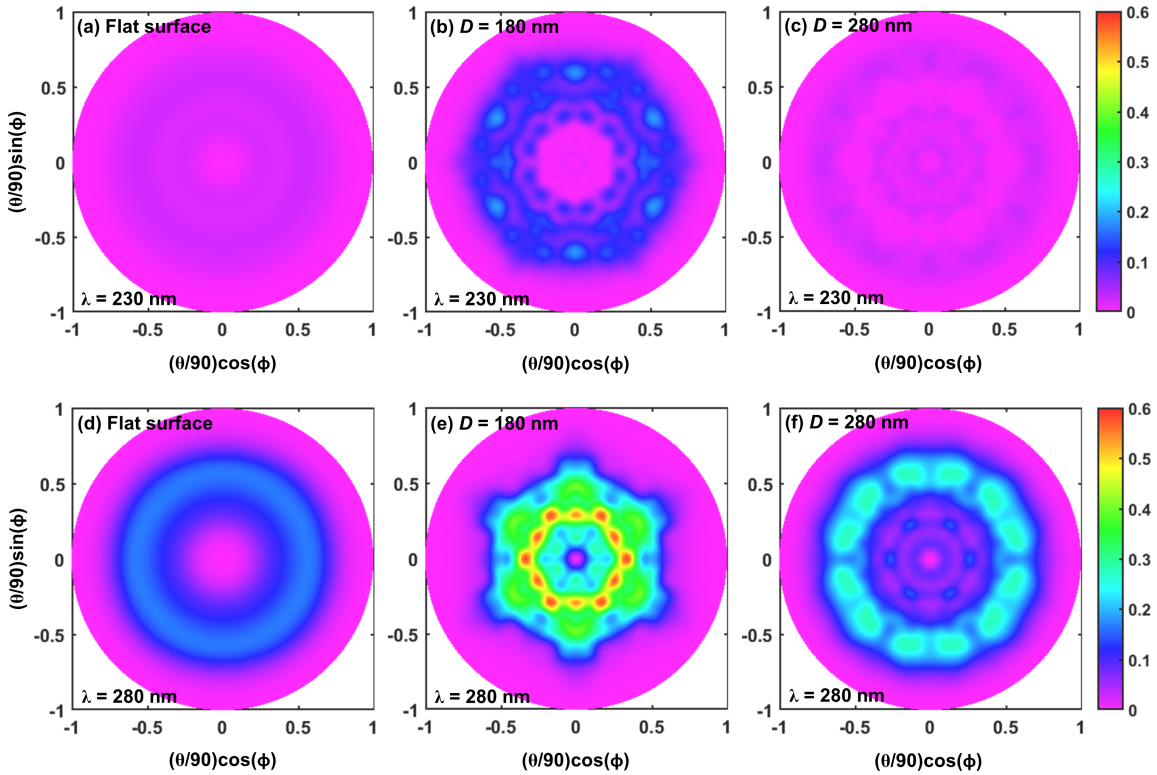

Figure 4.5: TM-polarization far-field radiation patterns of 230 nm [(a) – (c)] and 280 nm [(d) – (f)] flip-chip UV LEDs with flat sapphire substrate [(a) & (d)], bottom-side microdome-shaped PSS with D = 180 nm [(b) & (e)] and bottom-side microdome-shaped PSS with D = 280 nm [(c) & (f)].

As described previously, the use of PSS enhances the scattering of photons, which results in a modified light radiation pattern and the $\eta_{extraction}$. For conventional flip-chip UV LEDs with a flat sapphire substrate, both the 230 nm and 280 nm TM-polarized light exhibits symmetric donut-shaped radiation patterns with peak intensity at ∼30° with respect to c-axis [Figures 4.5(a) and 4.5(d)]. Lower intensity is observed for 230 nm UV LED as compared to 280 nm UV LED due to the larger refractive index contrast between the AlGaN/GaN layers, sapphire and air medium as well as higher absorption in the AlGaN/GaN materials for 230 nm. For both

emission wavelengths, when D = 180 nm, UV LEDs with bottom-side PSS show higher radiation intensity over large angle range (∼25° to ∼40° for 230 nm and ∼10° to ∼40° for 280 nm) [Figures 4.5(b) and 4.5(e)]. In addition, overall higher radiation intensity can also be observed attributed to the curvature surfaces of the microdomes that result in larger photon escape cone as compared to conventional UV LEDs. This spread-out distribution of high intensity radiation pattern for the investigated UV LEDs with bottom-side PSS has contributed to the larger TM-polarized $\eta_{extraction}$ (∼4.2-times and ∼1.8-times for 230 nm and 280 nm respectively) than conventional UV LEDs with a flat sapphire substrate.

For the case of D = 280 nm, the bottom-side PSS is suppressing the extraction of 230 nm TM-polarized photons [Figure 4.5(c)], which results in lower $\eta_{extraction}$ (∼0.8-times) than the UV LEDs with a flat sapphire substrate. However, substantial improvement in the TM-polarized $\eta_{extraction}$ (∼1.4-times) for 280 nm UV LEDs can still be obtained attributed to the high radiation intensity at angles between 20° and 40° [Figure 4.5(f)]. These results suggest that the optimum microdome design on the bottom side of the sapphire substrate is with smaller D than the UV LED emission wavelength, preferably ∼70 – 80 nm below the emission wavelength. Microdomes with large D should be avoided to prevent the bottom-side microdome-shaped PSS to act as reflector that limit the extraction of TM-polarized light through the sapphire substrate, as evidenced by the cases of D >260 nm for 230 nm UV LEDs.

As opposed to TM-polarization, the bottom-side PSS acts as reflector that inhibit TE-polarized light extraction through the sapphire substrate. As illustrated in Figure 4.6, significantly lower radiation intensity for both 230 nm and 280 nm UV LEDs with bottom-side microdome-shaped PSS is observed as compared to UV LEDs with a flat sapphire substrate. For UV LEDs with a flat sapphire substrate [Figures 4.6(a) and 4.6(d)], the TE-polarized light intensity is primarily concentrated at the center region. Although the use of bottom-side PSS could

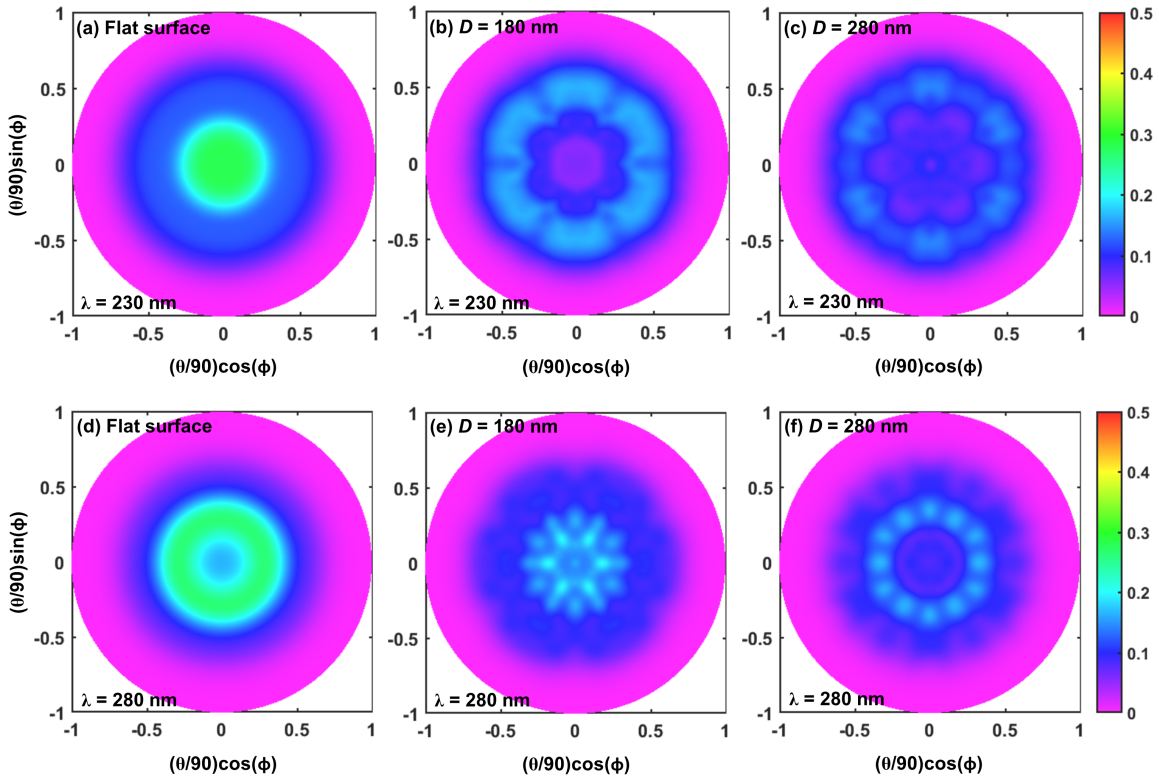

Figure 4.6: TE-polarization far-field radiation patterns of 230 nm [(a) – (c)] and 280 nm [(d) – (f)] flip-chip UV LEDs with flat sapphire substrate [(a) & (d)], bottom-side PSS with $D = 180$ nm [(b) & (e)] and bottom-side PSS with $D = 280$ nm [(c) & (f)].

redirect the light radiation pattern [Figures 4.6(b), 4.6(c), 4.6(e) and 4.6(f)], it scatters more TE-polarized photons back into the LED structure than extracting them out through the sapphire substrate. To be more specific, as D increases from 180 nm to 280 nm, the TE-polarized $\eta_{extraction}$ drops from ∼0.9-times and ∼0.8-times for 230 nm and 280 nm UV LEDs respectively to ∼0.8-times and ∼0.7-times for 230 nm and 280 nm UV LEDs respectively. This degraded TE-polarized $\eta_{extraction}$ is also supported by the lower radiation intensity distributions observed in Figures 4.6(b), 4.6(c), 4.6(e) and 4.6(f).

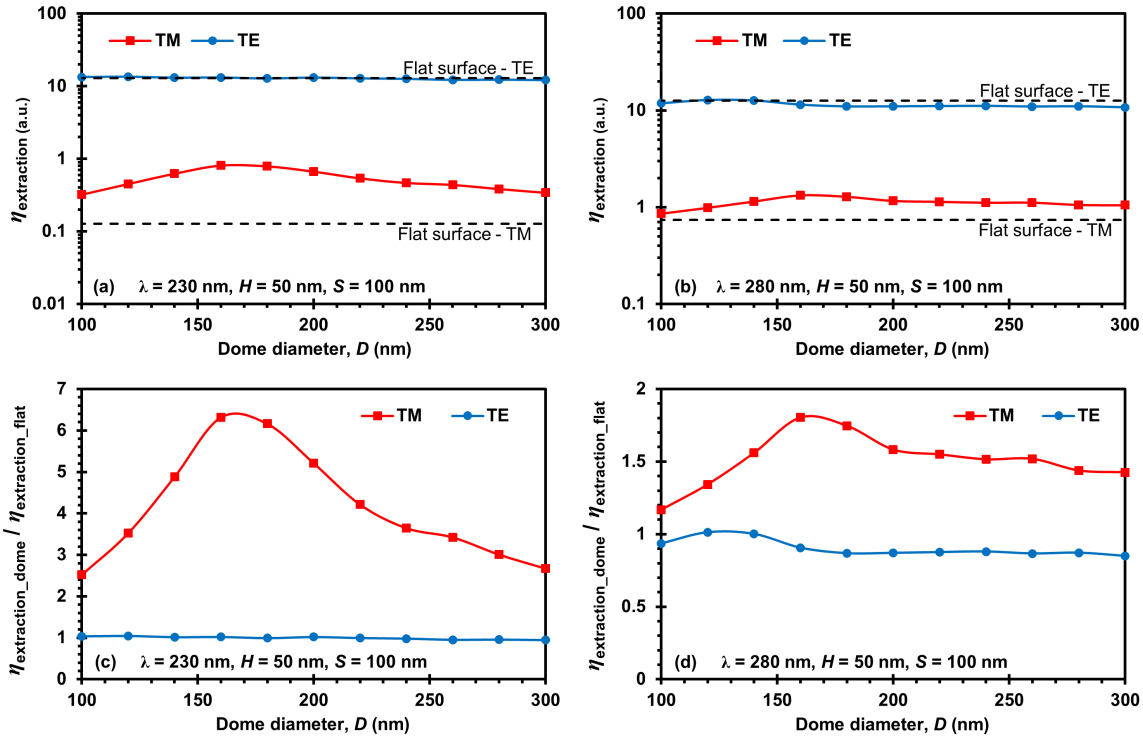

Figure 4.7: The $\eta_{extraction}$ for AlGaN-based flip-chip UV LEDs with microdome-shaped patterning on the top side of sapphire substrate emit at (a) $\lambda = 230$ nm and (b) $\lambda = 280$ nm as a function of D. The $\eta_{extraction}$ for UV LEDs with a flat sapphire substrate are represented by the black dashed lines. Ratio of the $\eta_{extraction}$ for UV LEDs with top-side microdome-shaped PSS ($\eta_{extraction\_dome}$) to the $\eta_{extraction}$ for flip-chip UV LEDs with flat sapphire substrate ($\eta_{extraction\_flat}$) for (c) $\lambda = 230$ nm and (d) $\lambda = 280$ nm as a function of D. The $\eta_{extraction}$ for UV LEDs with bottom-side microdome-shaped PSS are represented by dashed lines.

4.2.3 Flip-Chip UV LEDs with Microdome-Shaped Patterning on Top Surface of Sapphire Substrate

The enhancement of $\eta_{extraction}$ for flip-chip UV LEDs with top-side microdome-shaped PSS has been investigated here to understand the influence of microdome patterning to the mid- and deep-UV LED $\eta_{extraction}$. From the results presented in Figure 4.7, TE-polarized $\eta_{extraction}$ are consistently higher than TM-polarized $\eta_{extraction}$ (>1 order of magnitude) for both 230 nm and 280 nm UV LEDs with top-side PSS. Nevertheless, significant enhancement in TM-polarized $\eta_{extraction}$ (up to ~6.3-times and ~1.8-times

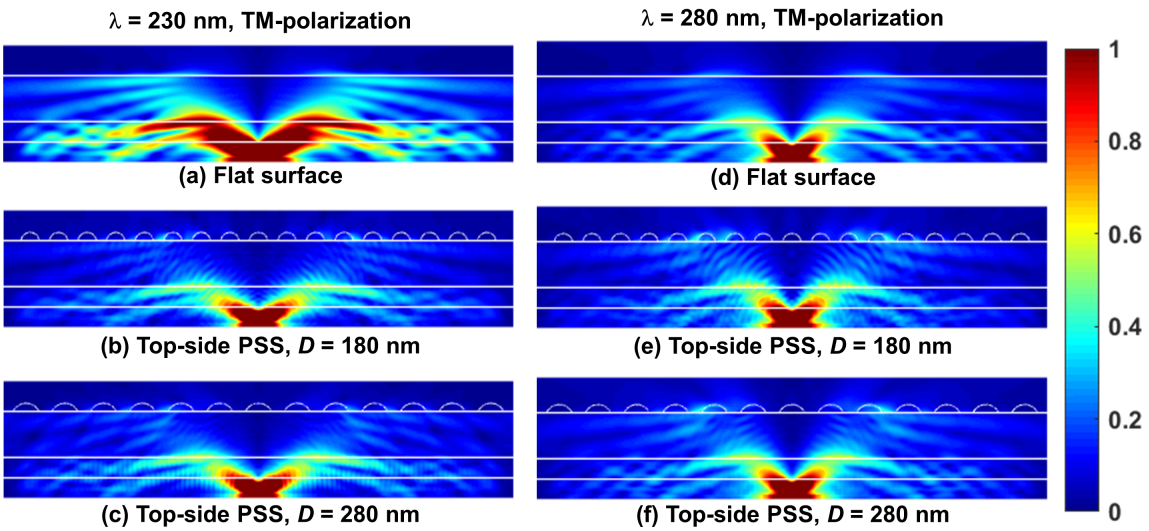

Figure 4.8: Cross-sectional near-field electric field intensity of 230 nm [(a) – (c)] and 280 nm [(d) – (f)] TM-polarized flip-chip UV LEDs with flat sapphire substrate [(a) & (d)], top-side PSS with D = 180 nm [(b) & (e)], and top-side PSS with D = 280 nm [(c) & (f)].

for 230 nm and 280 nm UV LEDs respectively) is observed as compared to TE-polarized $\eta_{extraction}$ (<5% enhancement for both 230 nm and 280 nm UV LEDs). As previously stated, TM-polarized light primarily travels at large angles with respect to c-axis while TE-polarized light mostly travels along c-axis, the curvature surface of the microdomes on the sapphire substrate have more effects on extracting TM-polarized photons out of the LED structure than the TE-polarized photons. Comparable to the UV LEDs with bottom-side PSS, the UV LEDs with top-side PSS demonstrate strong dependence on D for TM-polarized $\eta_{extraction}$ but has negligible effect on TE-polarized $\eta_{extraction}$. Again, this is attributed to the function of the PSS that acts as an extractor for TM-polarized output and as a reflector for TE-polarized output, as illustrated in Figures 4.8 and 4.9. As TM-polarized photons are primarily traveling at large angles with respect to c-axis, the majority of the TM-polarized output is trapped inside the LED structure, which results in low $\eta_{extraction}$. The use of PSS enhances the photons scattering effect, thus can enable more TM-polarized photons to escape

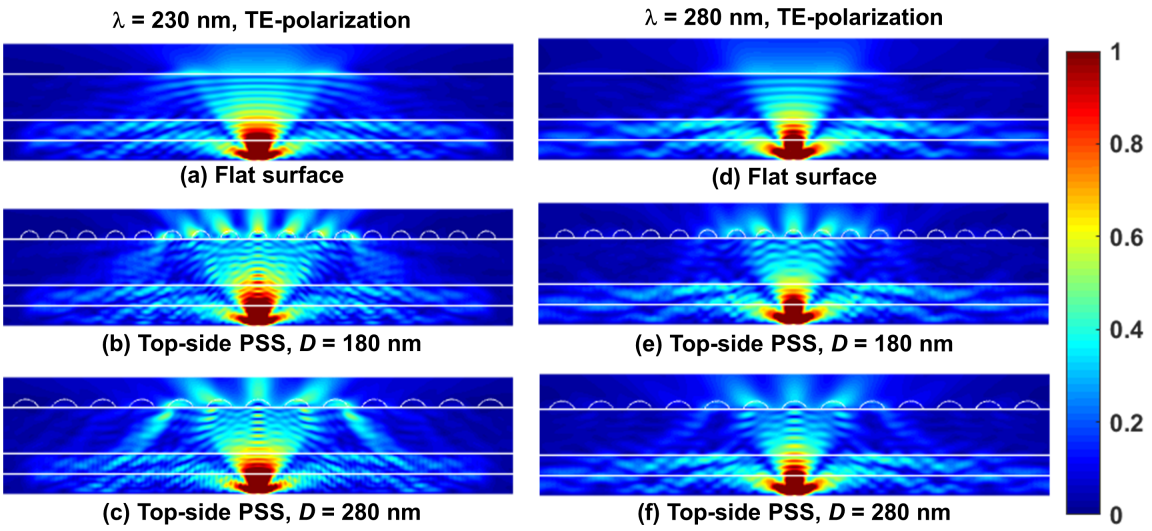

Figure 4.9: Cross-sectional near-field electric field intensity of 230 nm [(a) – (c)] and 280 nm [(d) – (f)] TE-polarized flip-chip UV LEDs with flat sapphire substrate [(a) & (d)], top-side PSS with D = 180 nm [(b) & (e)], and top-side PSS with D = 280 nm [(c) & (f)].

the UV LED structure when acting like an extractor. On the other hand, since the TE-polarized light primarily travels along c-axis, the scattering effect introduced by the chosen dimension of PSS has a detrimental influence on the TE-polarized photons in UV LEDs with PSS than the UV LEDs with a flat sapphire surface. Specifically, the PSS acts as a reflector that inhibits TE-polarized light extraction through the sapphire substrate. As presented in Figures 4.7(c) and 4.7(d), ∼2.5-times to ∼6.3-times and ∼1.1-times to ∼1.8-times enhancement in TM-polarized $\eta_{extraction}$ for 230 nm and 280 nm UV LEDs with top-side PSS respectively can be obtained for D ranges between 100 nm and 300 nm. Conversely, the ratio of TE-polarized $\eta_{extraction}$ for UV LEDs with top-side PSS to UV LEDs with flat sapphire substrate drops from ∼1.04-times to ∼0.95-times for 230 nm and ∼1.01-times to ∼0.85-times for 280 nm when D changes from 100 nm to 300 nm.

Similar to the case of bottom-side PSS, the microdome-shaped array patterning on the top-side of the sapphire substrate also acts as a strong photons scattering

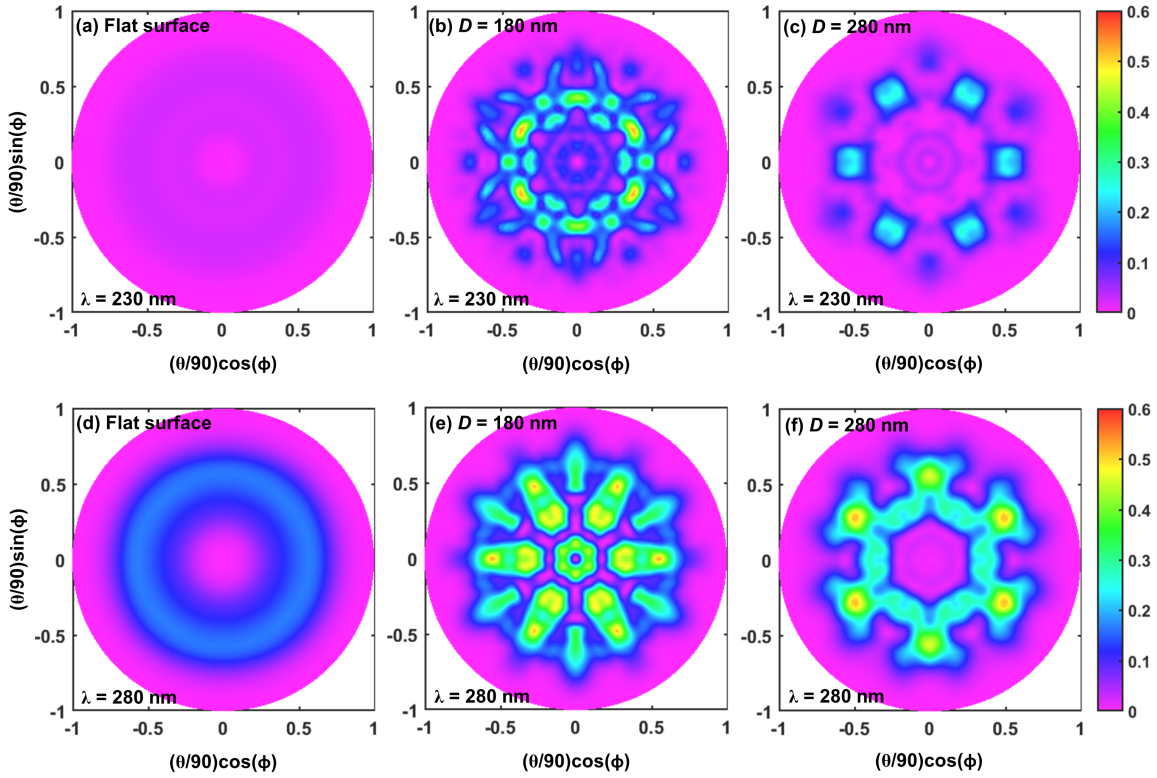

Figure 4.10: TM-polarization far-field radiation patterns of 230 nm [(a)–(c)] and 280 nm [(d)–(f)] flip-chip UV LEDs with flat sapphire substrate [(a) & (d)], top-side PSS with D = 180 nm [(b) & (e)] and top-side PSS with D = 280 nm [(c) & (f)].

center, which will impact the light extraction for the LED device. From the far-field radiation patterns shown in Figure 4.10, significantly higher radiant intensity can be observed for both 230 nm and 280 nm UV LEDs with top-side PSS at an angle between ∼10° and ∼50° while the conventional UV LEDs with flat sapphire substrate exhibit symmetric donut-shaped radiation patterns with peak intensity at ∼30°. This is primarily attributed to the curvature surfaces of the microdomes that result in larger photon escape cone than the conventional UV LEDs with a flat sapphire substrate. Consequently, this spread-out distribution of high intensity radiation pattern leads to higher TM-polarized $\eta_{extraction}$ (up to ∼6.3-times and ∼1.8-times for 230 nm and 280 nm respectively) as compared to conventional UV LEDs with flat sapphire substrate.

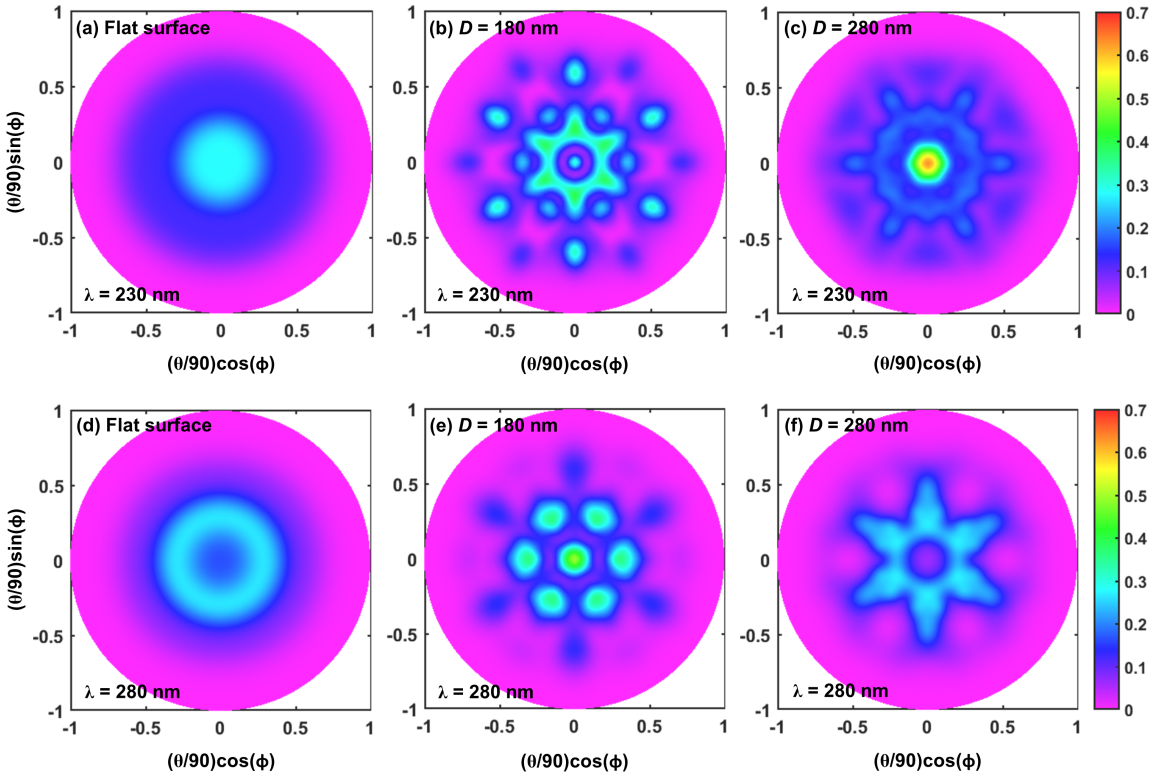

Figure 4.11: TE-polarization far-field radiation patterns of 230 nm [(a) – (c)] and 280 nm [(d) – (f)] flip-chip UV LEDs with flat sapphire substrate [(a) & (d)], top-side PSS with D = 180 nm [(b) & (e)] and top-side PSS with D = 280 nm [(c) & (f)].

For TE-polarization, employing top-side PSS for both the 230 nm and 280 nm UV LEDs has very similar effect as those with bottom-side PSS. From the far-field radiation plots presented in Figure 4.11, it is obvious that the top-side PSS for both the 230 nm and 280 nm UV LEDs are not a good extractor to enable TE-polarized photons to escape through the sapphire substrate. Even though the top-side PSS acts as a strong scattering center and results in altered radiation patterns as compared to conventional UV LEDs with a flat sapphire substrate, the fraction of TE-polarized photons that can be extracted from the structure is not high enough to compensate for the fraction of photons being reflected back into the structure. In addition, even though higher radiation intensity can be observed in some regions of the far-field radiation plots presented in Figure 4.11, particularly when D = 280 nm for 230 nm

UV LEDs [Figure 4.11(c)], majority of the area still observed extremely low radiation intensity (dark blue and purple region). Consequently, lower TE-polarized $\eta_{extraction}$ for the UV LEDs with top-side PSS as compared to UV LEDs with flat sapphire substrate has been resulted.

4.2.4 Flip-Chip UV LEDs with Microdome-Shaped Patterning on Both Sides of Sapphire Substrate

The results for both 230 nm and 280 nm flip-chip UV LEDs with single-sided (bottom-side or top-side) microdome-shaped PSS in previous sub-sections have demonstrated significant enhancement for TM-polarized $\eta_{extraction}$ but degraded TE-polarized $\eta_{extraction}$ when D changes from 100 nm to 300 nm. Here, the effect of combining the bottom-side and top-side patterning on the TE- and TM-polarized $\eta_{extraction}$ for both 230 nm and 280 nm flip-chip UV LEDs has been studied. The enhancement ratio for the UV LEDs with double-sided patterning normalized to conventional UV LEDs with a flat sapphire substrate are presented in Figure 4.12(a) for $\lambda = 230$ nm and Figure 4.12(b) for $\lambda = 280$ nm. The $\eta_{extraction}$ ratio for UV LEDs with top-side and bottom-side PSS represented by dotted lines and dashed lines respectively are also plotted in Figure 4.12 for comparison.

From the results presented in Figure 4.12, the use of double-sided PSS will result in even higher TM-polarized $\eta_{extraction}$ than the single-sided PSS where up to $\sim$11.2-times and $\sim$2.6-times enhancement can be obtained for 230 nm and 280 nm UV LEDs respectively as compared to UV LEDs with a flat sapphire substrate. These substantial improvements for TM-polarized $\eta_{extraction}$ by employing double-sided PSS are attributed to the strong light scattering effects coming from both the top-side and bottom-side patterning, which is evidenced in the cross-sectional near-field electric field intensity plots presented in Figures 4.13 and 4.14. The scattering effect introduced by the microdome-shaped PSS also

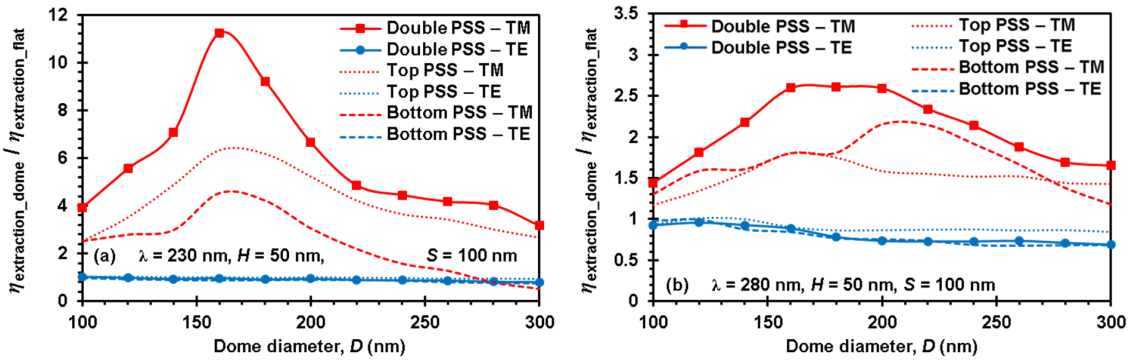

Figure 4.12: Ratio of the $\eta_{extraction}$ for flip-chip UV LEDs with double-sided PSS ($\eta_{extraction\_dome}$) to the $\eta_{extraction}$ for flip-chip UV LEDs with flat sapphire substrate ($\eta_{extraction\_flat}$) for (a) λ = 230 nm and (b) λ = 280 nm as a function of D. The $\eta_{extraction}$ for flip-chip UV LEDs with top-side and bottom-side PSS are represented by the dotted lines and dashed lines respectively.

resulted in modified far-field radiation patterns. In particular, the TM-polarized $\eta_{extraction}$ for the double-sided PSS is very similar to as taking the superposition of the TM-polarized $\eta_{extraction}$ for the bottom-side and top-side patterning. Nevertheless, the enhancement ratio is not exactly the same as by adding the TM-polarized $\eta_{extraction}$ from the bottom-side and top-side patterning due to the destructive interference. For 230 nm UV LEDs with double-sided PSS, the peak TM-polarized $\eta_{extraction}$ enhancement occurs at D = 160 nm, which is the same as those with bottom-side or top-side PSS [Figure 4.12(a)]. However, for the case of 280 nm UV LEDs, as the peak TM-polarized $\eta_{extraction}$ enhancement for bottom-side and top-side PSS occurs at different D (200 nm for bottom-side PSS and 160 nm for top-side PSS), a broad TM-polarized $\eta_{extraction}$ enhancement ratio peak for double-sided PSS has been observed [Figure 4.12(b)]. Specifically, the TM-polarized $\eta_{extraction}$ enhancement ratio for 280 nm UV LEDs with double-sided PSS are approximately ~2.6-times for D ranges between 160 nm and 200 nm.

In order to prove that the significantly enhanced TM-polarized $\eta_{extraction}$ for the UV LEDs with double-sided PSS are resulted from the superposition of the bottom-

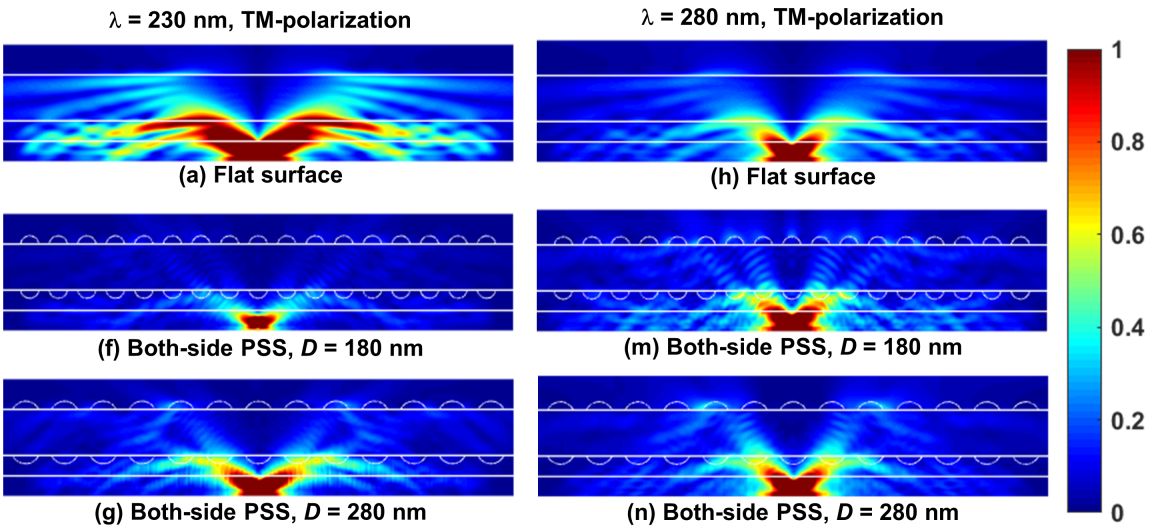

Figure 4.13: Cross-sectional near-field electric field intensity of 230 nm [(a) – (c)] and 280 nm [(d) – (f)] TM-polarized flip-chip UV LEDs with flat sapphire substrate [(a) & (d)], both-side PSS with $D = 180$ nm [(b) & (e)], and both-side PSS with $D = 280$ nm [(c) & (f)].

side and top-side patterning, the TM-polarized far-field radiation patterns for UV LEDs with double-sided PSS have been plotted in Figure 4.15. Figures 4.15(a) – 4.15(c) show the TM-polarized far-field radiation patterns for 230 nm UV LEDs and Figures 4.15(d) – 4.15(f) show the TM-polarized far-field emission patterns for 280 nm UV LEDs. By comparing the TM-polarized far-field radiation plots for the UV LEDs with double-sided PSS [Figure 4.15] to those with bottom-side PSS [Figure 4.5] and top-side PSS [Figure 4.10], it is obvious that the radiation patterns for UV LEDs with double-sided patterning are basically the combination of the far-field radiation patterns from the top-side and bottom-side patterning. As an example, for the case of $D = 180$ nm for 230 nm UV LEDs, the UV LED with bottom-side PSS has emission patterns at angle ranges from $\sim 25^\circ$ to $\sim 40^\circ$ [Figure 4.5(b)] while the UV LED with top-side PSS has emission patterns at angle ranges from $\sim 10^\circ$ to $\sim 50^\circ$ [Figure 4.10(b)]. From Figure 4.15(b), it is obvious that the 230 nm UV LED with double-sided PSS has very similar emission patterns as those with bottom-side patterning and top-side

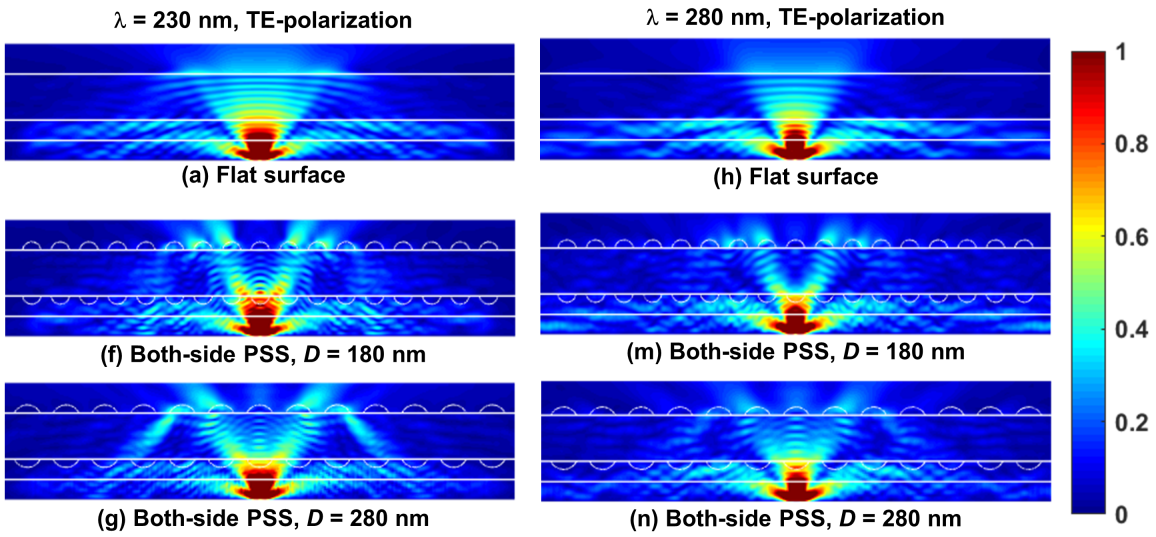

Figure 4.14: Cross-sectional near-field electric field intensity of 230 nm [(a) – (c)] and 280 nm [(d) – (f)] TE-polarized flip-chip UV LEDs with flat sapphire substrate [(a) & (d)], both-side PSS with $D = 180$ nm [(b) & (e)], and both-side PSS with $D = 280$ nm [(c) & (f)].

patterning at angles between ∼10° to ∼50°. In particular, large radiation intensity can be observed at angles between ∼25° and ∼40°.

On the contrary, the use of double-sided PSS for both 230 nm and 280 nm flip-chip UV LEDs does not lead to enhanced TE-polarized $\eta_{extraction}$ when D ranges between 100 nm and 300 nm (blue solid lines in Figure 4.12), which is similar to the phenomena observed for the case of flip-chip UV LEDs with bottom-side PSS and top-side PSS (blue dashed lines and dotted lines in Figure 4.12). This has been expected as the single-sided PSS has been observed to primarily act as a reflector to prevent TE-polarized photons extraction through the sapphire substrate. As a result, smaller TE-polarized $\eta_{extraction}$ has been obtained as compared to UV LEDs with a flat sapphire substrate. In addition, the TE-polarized $\eta_{extraction}$ for UV LEDs with double-sided PSS is primarily limited by the bottom-side patterning as the bottom reflector only allow a very minimum amount of TE-polarized photons to pass through. As can been seen from the TE-polarized far-field radiation patterns plotted in Figure 4.16,

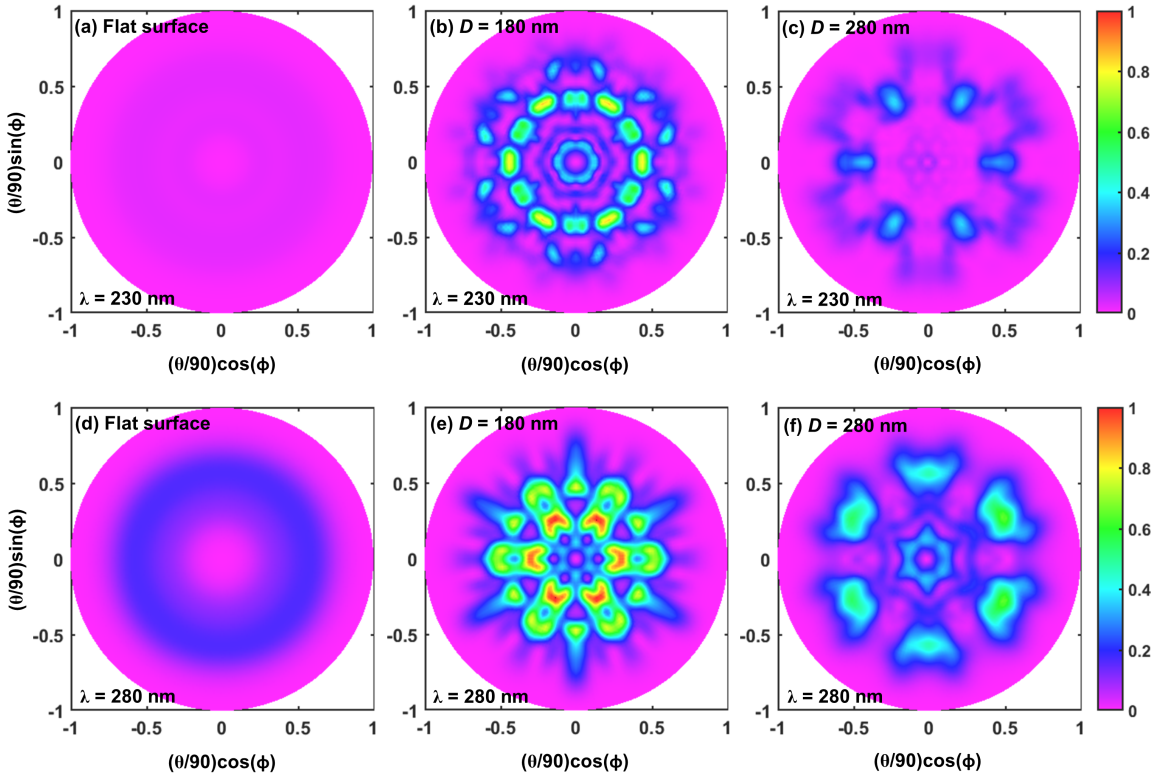

Figure 4.15: TM-polarization far-field radiation patterns of 230 nm [(a) – (c)] and 280 nm [(d) – (f)] flip-chip UV LEDs with flat sapphire substrate [(a) & (d)], double-sided PSS with $D = 180$ nm [(b) & (e)] and double-sided PSS with $D = 280$ nm [(c) & (f)].

the emission patterns for TE-polarized 230 nm and 280 nm UV LEDs with double-sided PSS are primarily the combination radiation patterns of those with bottom-side patterning (Figure 4.6) and top-side patterning (Figure 4.11). For instance, for the case of $D = 280$ nm for 280 nm UV LEDs, the UV LED with bottom-side PSS exhibits circular-shaped far-field emission pattern [Figure 4.6(f)] while the UV LED with top-side PSS has a star-shaped like far-field emission pattern [Figure 4.11(f)].

4.3 Conclusion

The TE- and TM-polarized $\eta_{extraction}$ for 230 nm and 280 nm flip-chip UV LEDs with microdome-shaped array patterning on the sapphire substrate have been investigated. In particular, the TE- and TM-polarized $\eta_{extraction}$ for UV LEDs with bottom-side

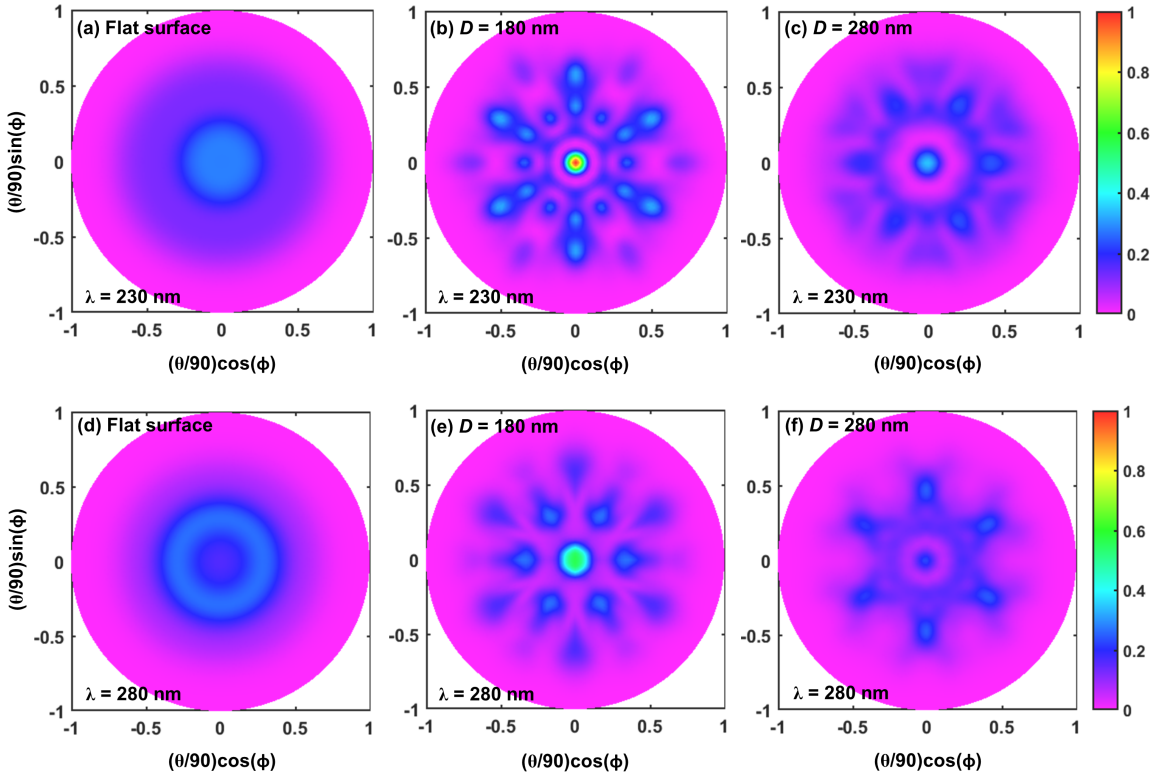

Figure 4.16: TE-polarization far-field radiation patterns of 230 nm [(a) – (c)] and 280 nm [(d) – (f)] flip-chip UV LEDs with flat sapphire substrate [(a) & (d)], double-sided PSS with $D = 180$ nm [(b) & (e)] and double-sided PSS with $D = 280$ nm [(c) & (f)].

patterning, top-side patterning, and double-sided patterning have been studied and compared. The analysis shows that microdome-shaped PSS with $H = 50$ nm, $S = 100$ nm, and $D = 100 – 300$ nm are particularly efficient in enhancing TM-polarized $\eta_{extraction}$ where up to ∼4.5-times and ∼2.2-times can be obtained for 230 nm and 280 nm flip-chip UV LEDs with bottom-side PSS respectively, and ∼6.3-times and ∼1.8-times for 230 nm and 280 nm flip-chip UV LEDs with top-side PSS respectively. The significant improvement obtained in the TM-polarized $\eta_{extraction}$ is attributed to the enhanced scattering effect introduced by the microdome-shaped array that enables the TM-polarized photons to escape from the LED structure. As a result, the use of double-sided PSS could result in even higher TM-polarized $\eta_{extraction}$ where up to ∼11.2-times and ∼2.6-times improvement can be achieved for 230 nm and

280 nm flip-chip UV LEDs respectively. For both emission wavelengths, the peak TM-polarized $\eta_{extraction}$ is observed when D is ∼70 – 100 nm below the emission wavelength. Accordingly, higher η_{EQE} from UV LEDs employing PSS is expected as a result of dominant TM-polarized spontaneous emission and larger TM-polarized $\eta_{extraction}$. On the contrary, the use of the microdome-shaped PSS does not lead to enhanced TE-polarized $\eta_{extraction}$ for both the 230 nm and 280 nm flip-chip UV LEDs. The PSS is actually acting as a reflector that reflects the majority of the TE-polarized light back into the structure. Consequently, lower TE-polarized $\eta_{extraction}$ for flip-chip UV LEDs with microdome-shaped PSS as compared to flip-chip UV LEDs with a flat sapphire substrate has resulted.

Note that the fabrication of the proposed LEDs with microdome-shaped PSS has not been implemented in this work due to the resources constraint issue. Nevertheless, the realization of the proposed PSS is possible through chemical wet etching as well as dry etching of the sapphire substrate. For example, nanosized SiO_2 patterning on a sapphire substrate, which can be formed by nickel nanoislands on top of SiO_2 film, can serve as a mask for sapphire etching in hot phosphoric acid [76]. Nanosphere lithography method by the use of SiO_2 nanospheres as a mask for dry etching the sapphire substrate in chlorine chemistry [77] can also be employed to fabricate the nanostructure PSS. Therefore, it is expected that the analysis presented in this study will shed light on the design of flip-chip UV LEDs with nanostructure PSS for both mid- and deep-UV regimes to achieve high-efficiency AlGaN-based UV LEDs.

Chapter 5

Fabrication of III-Nitride Nanowires

The fabrication process for planar structure III-nitride light-emitting diodes (LEDs) has been discussed in Chapter 3. In this chapter, the fabrication process of III-nitride nanowires utilizing the cleanroom facility at Rochester Institute of Technology (RIT) is presented. In particular, nanospheres lithography process has been developed to form III-nitride nanowires via top-down etching. The use of KOH-based solution in suppressing surface states on nanowire sidewalls due to plasma etch damage has also been discussed.

5.1 Introduction

Nanowires have emerged as a promising nanostructure for III-nitride emitters due to their unique electronic and optical properties. Studies have reported that III-nitride nanowires are largely free from strain and dislocations attributed to the effective lateral strain relaxation associated with the large surface-to-volume ratios and high aspect ratios [78, 66, 79, 80, 81]. Consequently, reduced threshold current densities and lower power consumption are anticipated from nanowires as compared to their

planar counterparts. In addition, higher light extraction efficiency ($\eta_{extraction}$) is also anticipated owing to the one-dimensional nature of nanowire that results in carriers confinement in two dimensions and photons propagation in only the third dimension.

The fabrication methods of nanowires generally can be categorized into two approaches: bottom-up growth and top-down etching. For the bottom-up approach, nanowires are synthesized onto substrate layer-by-layer in atomic scale while for the top-down approach, nanowires are formed through lithographic and etching steps. This chapter discusses the nanosphere lithography process to fabricate nanowires via top-down etching. As the nanowires are formed through physical bombardment to remove redundant materials, surface damage on the nanowire sidewalls will induce non-radiative recombination, which significantly degrades the quantum efficiency and output power of the nanowires. Therefore, the use of KOH-based solutions with various concentrations and temperatures in suppressing the surface states on nanowires have also been investigated.

5.2 Nanosphere Lithography

Nanosphere lithography process has been developed to fabricate III-nitride nanowire LEDs via top-down etching. Figure 5.1 summarizes the process flow. The fabrication processes of nanosphere lithography using silica spheres and polystyrene spheres as a mask for reactive-ion etching (RIE) has been developed. However, silica sphere is preferred for forming high aspect ratios nanowires as it is more resistant to chlorine-based RIE than polystyrene sphere. This section describes the nanosphere lithography using silica spheres to form nanowires while the procedure for using polystyrene spheres can be found in [82].

To begin with, an InGaN/GaN multiple quantum wells LED sample is cleaned with acetone and isopropyl alcohol (IPA), and then rinsed with deionized water (DI)

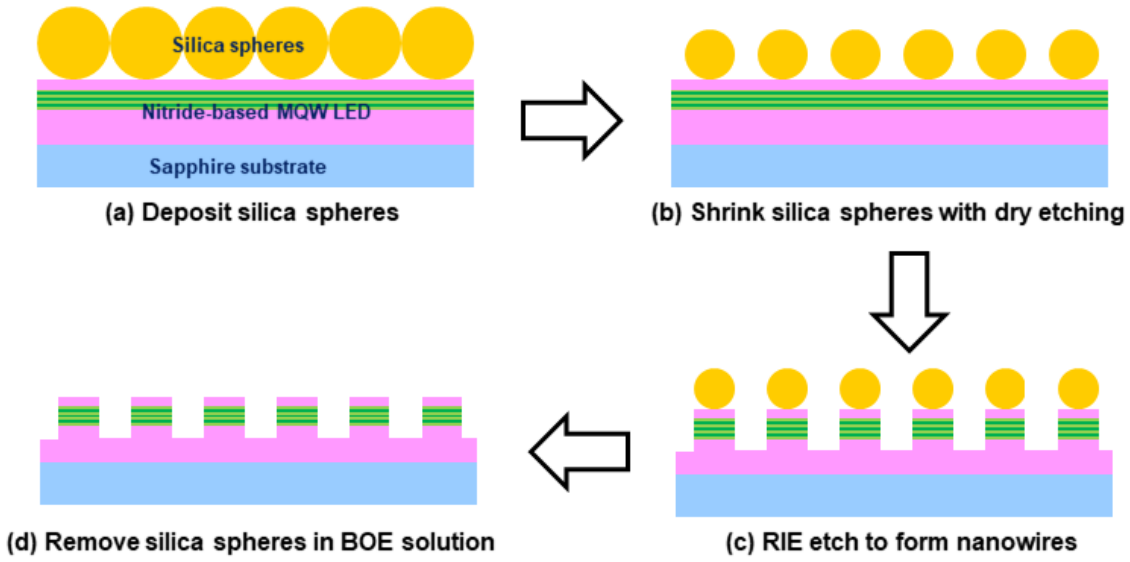

Figure 5.1: Process flow of fabricating III-nitride nanowires using nanosphere lithography and dry etching.

water. Next, oxygen (O_2) plasma treatment is performed on the sample surface to increase the surface hydrophilicity. Drytek 482 Quad Etcher is used for the surface treatment for 20 seconds at O_2 flow rate of 100 standard cubic centimeter per minute (sccm), RF power of 30 W and a chamber pressure of 100 mTorr. After O_2 treatment, a monolayer of silica spheres are then spin coated on the sample [Figure 5.1(a)]. The diameter of the silica spheres is critical for the nanowire dimension, such as nanowire diameter, nanowire height, and spacing between nanowires. Larger spheres diameter can sustain longer etching time during RIE to form high aspect ratio nanowires but also resulted in larger nanowires diameter.

For this experiment, 10 weight percent (wt%) silica spheres solution with sphere mean diameter of 700 nm is used as the mask to form the nanowires. The silica spheres are spin coated on the sample at the speed of 900 revolutions per minute (rpm) for 80 seconds. From the optical image shown in Figure 5.2(a), a large area of monolayer silica spheres can be observed on the substrate. The image capture using

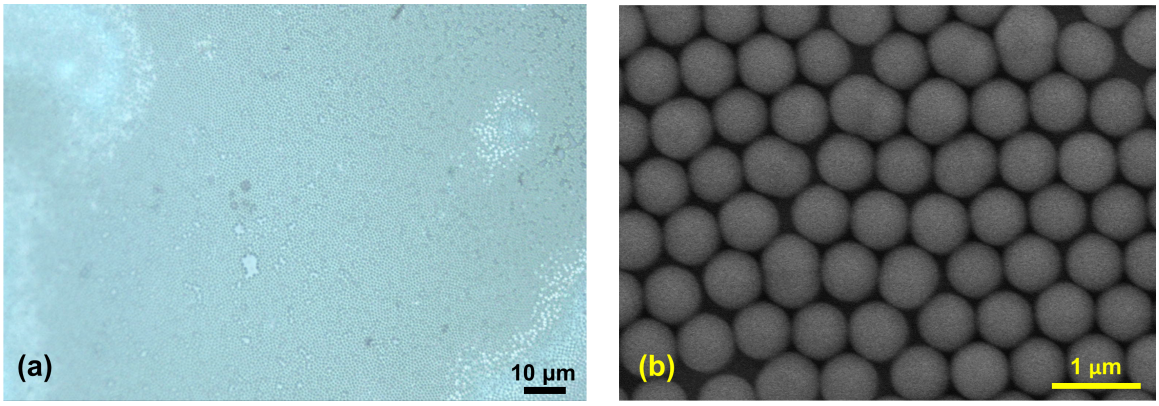

Figure 5.2: (a) Monolayer of 700 nm silica spheres spin-coated on the substrate under an optical microscope. (b) SEM image of the sample with a monolayer of 700 nm silica spheres on the substrate.

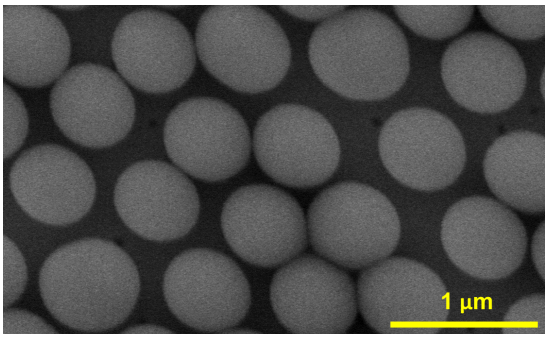

Figure 5.3: SEM image of the sample with a monolayer of silica spheres on the substrate after 40 seconds of RIE to shrink the silica spheres.

Hitachi S-4000 scanning electron microscope (SEM) in Figure 5.2(b) shows that those monolayer silica spheres are in hexagonally closed packed arrangement.

Next, the sample is loaded to Drytek 482 Quad Etcher for 40 seconds to shrink the silica spheres [Figure 5.1(b)]. The recipe with 90 sccm of SF_6, 30 sccm of O_2, RF power of 250 mW and a chamber pressure of 150 mTorr is used for this spheres shrinking step. Longer etching time can also be used to create larger spacing between the spheres, which will then resulted in larger spacing between the nanowires. Figure 5.3 shows the SEM image of the sample with silica spheres after 40 seconds of RIE. The etch rate of the 700 nm silica spheres is determined as $\sim$3 nm/sec.

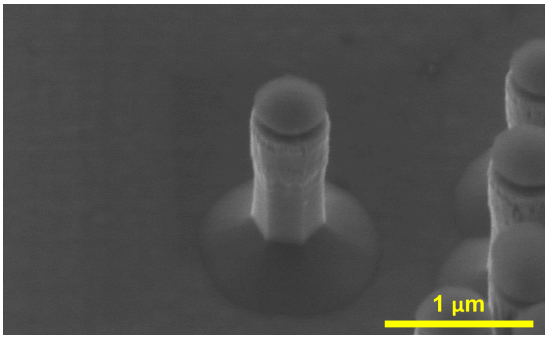

Figure 5.4: SEM image of the sample at 45° angle view showing nanowire structure with silica spheres on top after 50 minutes of RIE.

Then, nanowires are formed on the substrate through chlorine-based RIE using LAM 4600 [Figure 5.1(c)]. The same RIE recipe (30 sccm of Cl_2, 25 sccm of BCl_3, 8 sccm of $CHCl_3$, 20 sccm of Ar, RF power of 125 W and a chamber pressure of 100 mTorr) used to create LED mesa patterns described in Chapter 3.2 is used here for the formation of nanowires. Figure 5.4 shows the SEM image of the sample after 50 minutes of RIE. The etch rate of the silica spheres is calculated as ∼1.5 nm/min while the etch rate for the GaN is determined as ∼20 nm/min. As described in Chapter 3, this etch recipe has not been optimized for nanostructures. Higher etch rate can be achieved by varying the gases flow rates, for example, with reduced BCl_3 and $CHCl_3$, and the use of higher RF power [83]. In addition, a tapered base is observed for the nanowires due to shadowing effect and strong anisotropic etch during the RIE. By using lower chamber pressure, a more crystallographic base can be obtained [83]. This is particularly important for forming high aspect ratios nanowires.

Afterwards, the sample is dipped in buffered oxide etch (BOE) solution to remove the silica spheres [Figure 5.1(d)]. The final structure of the nanowires form through top-down etching using nanosphere lithography is presented in Figure 5.5(a). As can be seen from the SEM image, the ion bombardment during RIE is causing rough surface on the nanowire sidewalls. The bridges between the nanowires can be avoided by shrinking the silica spheres further to enable a larger

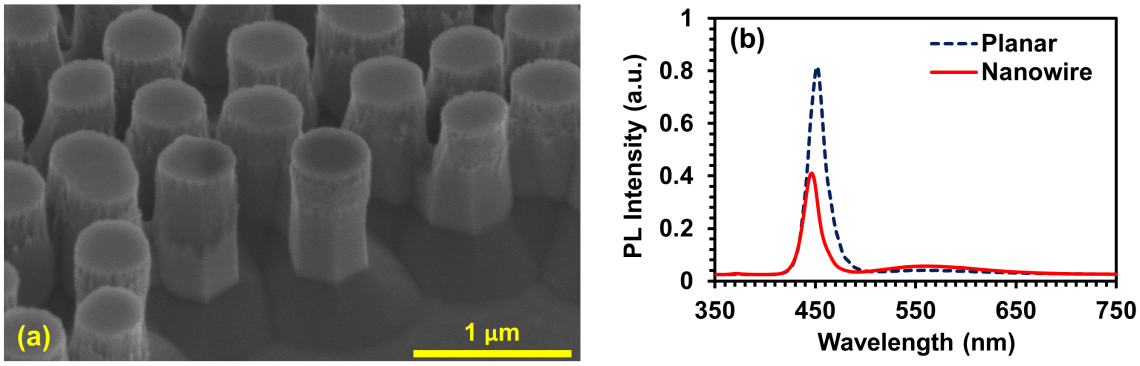

Figure 5.5: (a) SEM image of the sample at 45° angle view showing nanowire structure after removing silica spheres. (b) Comparison of PL intensity for planar structure and nanowire structure blue LEDs.

area of exposure for the ion bombardment to occur. The damage on the nanowire sidewalls gives rise to undesired non-radiative recombination, which significantly degrades the quantum efficiency and light output power of the nanowires. As evidenced by the photoluminescence (PL) intensity plot presented in Figure 5.5(b), the nanowire structure has ∼2-times lower blue emission peak than the planar structure. Moreover, larger defect peak at ∼550 nm can also be observed for the nanowires as compared to the planar structure. Therefore, surface passivation for suppressing the surface states on the nanowire sidewalls is critical for nanowires formed through top-down etching method.

5.3 Suppression of Surface States with KOH Wet Etching

The presence of high density of surface states due to the large surface area of nanowires is detrimental as the existence of these surface defects causes non-radiative recombination, which significantly limits the quantum efficiency and output power of the nanowires. As a result, methods to effectively reduce the

surface recombination arising from these surface states are essential to enhance the nanowires performance. Various surface passivation materials, such as inorganic sulfides, Si_3N_4, SiO_2, parylene, and undoped Al(Ga)N [84, 85, 86, 87] have been explored in the past to suppress the surface states on the nanowire sidewalls. On the other hand, wet etching method using NaOH [88], KOH [63], or TMAH [89] has also been investigated to remove the surface damage arisen from plasma etch.

Here, the use of AZ 400K solution, which is a KOH-based developer, for suppressing the surface states on nanowire sidewalls through wet etching has been carried out. In particular, the effectiveness of KOH solutions with various concentrations and temperatures in removing the nanowire sidewall roughness and tapered base are investigated. The concentrations of KOH are determined by the ratio of AZ 400K to DI water. Glass beakers containing various concentrations of AZ 400K solutions covered by aluminum foil are placed on a hot plate to heat the solutions to 45°C and 80°C. Solutions at room temperature are left on the wet bench without hotplate. A thermometer is used to monitor the temperature of the solutions. As-etched III-nitride nanowires are then dipped into the solutions and SEM images are captured at 10, 30, and 60 minutes.

Figure 5.6 shows the etch evolution of nanowires in 5% AZ 400K at room temperature (23°C) [Figures 5.6(a) – (c)], 45°C [Figures 5.6(d) – (f)], and 80°C [Figures 5.6(g) – (i)]. Slow etch rate with relatively small etch step is being observed for AZ 400K at room temperature, as evidenced by Figure 5.6(c), where a significant amount of surface damage can still be observed on the nanowires sidewalls even after 180 minutes etch. On the other hand, for AZ 400K at 80°C, fast etch rate can be obtained. However, there is a trade off between obtaining smooth nanowire sidewalls and removing the tapered base. Considerably smooth sidewall surface can be achieved after 30 minutes etch in AZ 400K at 80°C but with a staircase pattern tapered base [Figure 5.6(h)]. Further dipping the nanowires in the

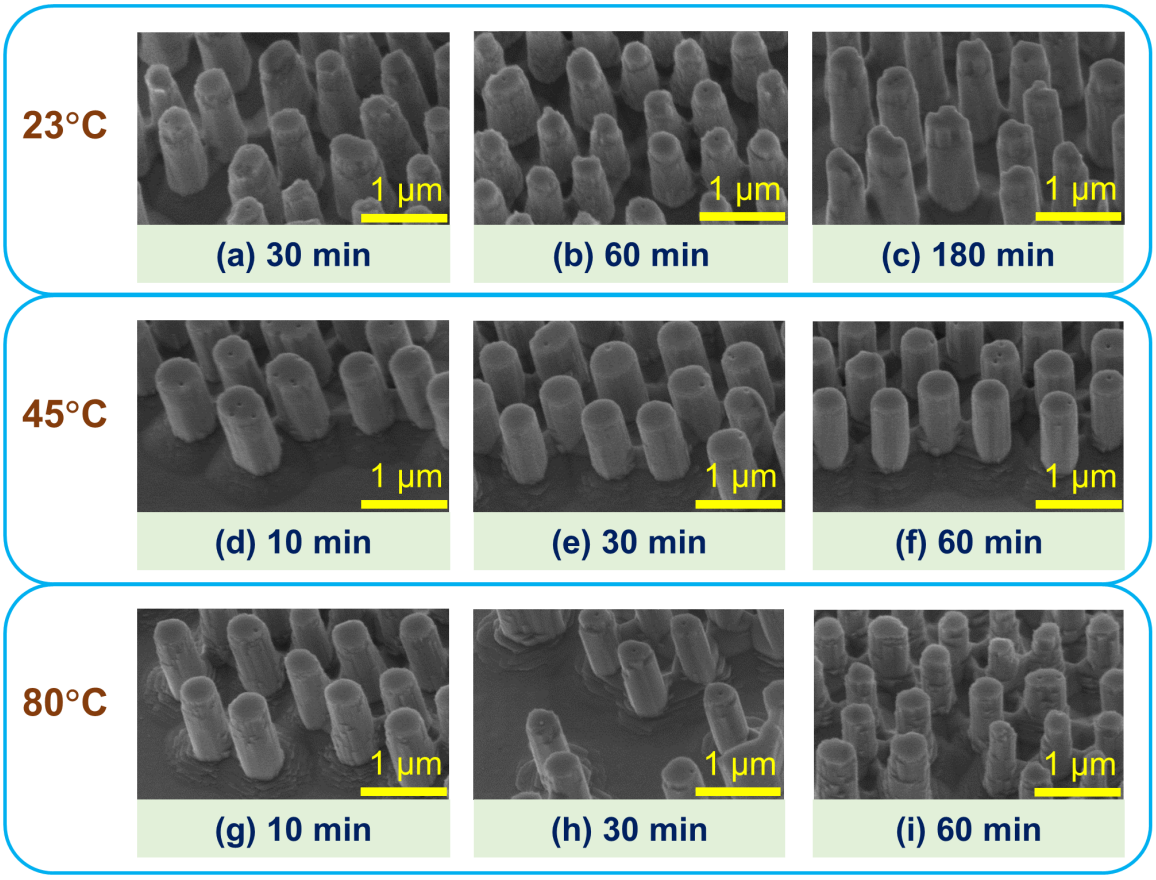

Figure 5.6: SEM images showing etch evolution of nanowires in 5% AZ 400K solutions at 23°C [(a) – (c)], 45°C [(d) – (f)], and 80°C [(g) – (i)].

solution for another 30 minutes can substantially eliminate the tapered base but with very rough sidewall surface [Figure 5.6(i)]. The removal of sidewall surface roughness as well as the tapered base can be expected by dipping the sample into the AZ 400K solution for an even longer time, however, this will result in significantly reduced nanowires diameter.

Considering the difficulty in controlling the etch rate of KOH solution at high temperature at the same time maintaining maintaining the diameter of the nanowires, the use of 5% AZ 400K at 45°C has been investigated. The SEM images show that relatively smooth sidewall surface can be achieved after 10, 30 and 60 minutes etch in AZ 400K at 45°C [Figures 5.6(d) – (f)]. The slower etch rate for AZ 400K at

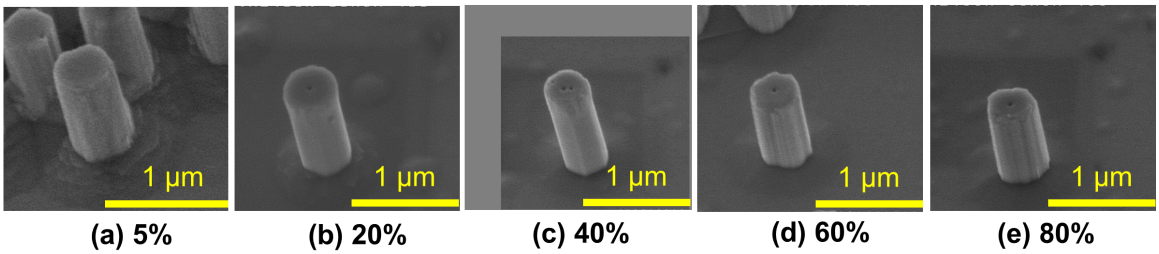

Figure 5.7: SEM images of nanowires after dipping in (a) 5%, (b) 20%, (c) 40 %, (d) 60%, and (e) 80% of AZ 400K solution for 30 minutes at 45°C.

45°C than the solution at 80°C does not introduce more roughness to the nanowires sidewalls after etching the sample for a longer time. Nevertheless, this also resulted in the requirement of dipping the nanowires in the solution for an extended period of time in order to completely remove the tapered base.

Alternatively, AZ 400K solutions with higher concentrations at 45°C can be used to get rid of the tapered base. Figure 5.7 shows the SEM images of the nanowires etched for 30 minutes in various concentration of AZ 400K at 45°C. As the concentrations increases from 5% to 80%, higher etch rate is observed where the nanowire sidewall changes from staircase-like pattern to more column morphology within a shorter period of time. The tapered base is also observed to disappear faster at higher concentration of AZ 400K. In particular, the tapered base started to vanish at 20% of AZ 400K [Figure 5.7(b)], and has been completely removed at a concentration of 40% or higher [Figures 5.7(c) – (e)].

The KOH-based solution has near zero etch rate for c-plane [Figure 5.8(a)] while relatively fast etch rate for m-plane [Figure 5.8(b)]. Consequently, the rough nanowire sidewalls can be removed while maintaining the height of the nanowires during the etch. In addition, faster etch rates for r-plane [Figure 5.8(c)] and $(10\bar{1}1)$-plane [Figure 5.8(d)] than the sidewall facets (m-plane) can effectively remove the tapered base to form high aspect ratios nanowires. With extended etching time or higher concentrations of KOH solutions at elevated temperatures,

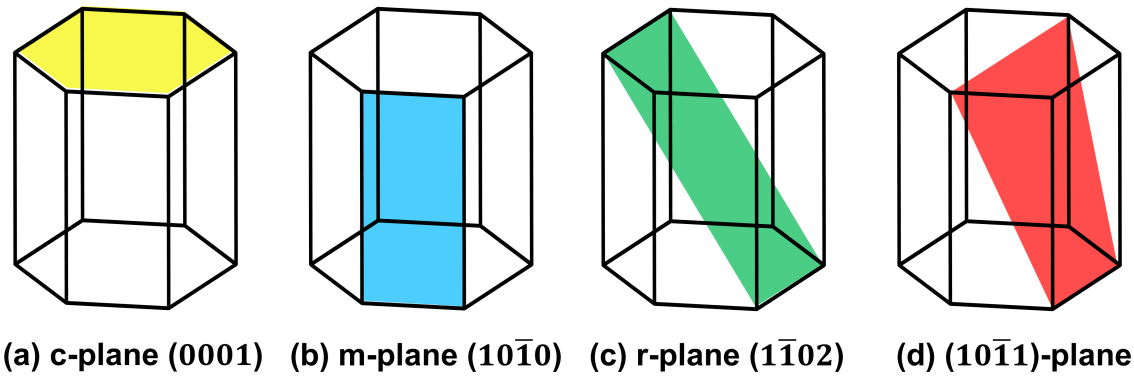

Figure 5.8: Representative atomic planes of wurtzite GaN crystals for (a) c-plane, (b) m-plane, (c) a-plane, (d) r-plane, and (e) (10$\bar{1}$1)-plane.

the r-plane will slowly transform into (10$\bar{1}$1)-plane, and then the (10$\bar{1}$1)-plane will develop into m-plane [90], which eventually resulted in smooth vertical nanowire sidewalls with crystallographic base.

5.4 Conclusion

In summary, nanosphere lithography has been developed to fabricate III-nitride nanowires via top-down etching. The RIE recipe used in this preliminary study has not been optimized for faster etch rate, and for fabricating nanowires without taper base. Further optimization of the etch recipe by altering the gases flow rates, chamber pressure and RF power would be necessary in order to resolve these issues. In addition, investigation of KOH-based solutions with various concentrations and temperatures in removing nanowires sidewall surface damage arisen from the plasma etch as well as taper base has also been performed. Results show that AZ 400K solution with a concentration of 40%, at temperature of 45°C is adequate to achieve smooth nanowires with crystallographic base after etching for 30 minutes.

The work discussed in this chapter is a collaborative work with two other graduate students at RIT, Xing Lei and Matthew Hartensveld, and part of this work has been

presented in their Master theses [82, 83]. In particular, Lei's thesis [82] discussed the preliminary experimental effort in developing the nanosphere lithography via transfer method where a monolayer of nanospheres formed on the water surface is scooped up to transfer to GaN substrate. While Lei and Hartensveld were working on the transfer method, my work focused on developing the nanosphere lithography using spin coating method, where nanospheres are spin-coated on the GaN substrate to form the monolayer. We then worked together on the KOH wet etching of GaN, and this has been discussed in Hartensveld's thesis [83]. In addition to the KOH wet etching study, Hartensveld's thesis [83] also has detailed information on the optimization study for the dry etching process with various gases flow rates, chamber pressures. and RF powers.

Chapter 6

Nanowire Structure III-Nitride UV LEDs

In this chapter, polarization-dependent light extraction efficiency ($\eta_{extraction}$) of AlGaN-based nanowire light-emitting diodes (LEDs) in deep-ultraviolet (DUV) regime has been investigated using three-dimensional (3D) finite-difference time-domain (FDTD) method. Specifically, the light extraction properties of 230 nm nanowire LEDs with various nanowire diameters and heights as well as with different dielectric materials as passivation layer have been analyzed. Simulation results showed that up to ∼48% transverse-magnetic (TM)-polarized $\eta_{extraction}$ and ∼41% transverse-electric (TE)-polarized $\eta_{extraction}$ could be obtained with nanowire structure as compared to ∼0.2% TM-polarized $\eta_{extraction}$ and ∼2% TE-polarized $\eta_{extraction}$ from a conventional planar structure.

6.1 Introduction

The efficiency of AlGaN-based UV LEDs, especially for DUV LEDs with emission wavelength (λ) < 250 nm, is still extremely low compared to its visible counterparts that are based on InGaN active regions. In particular, the external quantum efficiency

(η_{EQE}) of AlGaN quantum well (QW) ultraviolet (UV) LEDs with planar structure has been reported to be less than 10% for $\lambda < 300$ nm, and further drops to ~1% when λ is below 250 nm [91, 92]. One of the factors that cause this extremely low performance for AlGaN-based UV LEDs is the valence subbands crossover [35, 41, 42, 43, 7] at high Al-composition AlGaN QW active region that results in dominant TM polarized output in DUV regime.

Recent studies on AlGaN-based nanowire structure have reported encouraging device performance for mid- and DUV LEDs [26, 27, 28]. Experimental studies on nanowire UV LEDs have demonstrated substantial improvement in the internal quantum efficiency (η_{IQE}) for peak emission wavelength of 340 nm [26] down to 210 nm [28] attributed to dislocation-free materials and improved p-type doping. Another key advantage of the use of nanowire design is the enhancement of $\eta_{extraction}$ due to the significantly improved surface-to-volume ratios [26, 27, 28, 67]. Nanowire design with a larger surface area than the conventional planar structure can allow more light to escape through the sidewall, which in turn will lead to larger $\eta_{extraction}$. While experimental studies have demonstrated promising results for UV LEDs with nanowire structures, there has been very limited work devoted to investigating the polarization-dependent $\eta_{extraction}$ for AlGaN-based nanowire UV LEDs which is of great importance due to the existence of the valence subbands crossover [35, 41] that results in TM-dominant spontaneous emission in the DUV regime.

Note that previous works [67, 70] have theoretically investigated the light extraction properties of the 280 nm AlGaN nanowire LEDs and concluded dominant TM-polarized light extraction from those structures. However, due to the significantly low TM-polarized spontaneous emission rate (R_{sp}) at 280 nm [35, 41], it is still very difficult to achieve a promising η_{EQE}. On the other hand, it is important to note that the TM-R_{sp}will become dominant for wavelengths at 230 nm

as the crystal-field split-off (CH) subband occupies the highest energy level in conventional AlGaN-based active region with high Al-compositions [35, 41]. Nevertheless, the polarization-dependent light extraction mechanism has not been studied yet for this DUV regime.

Therefore, in this study, the TE- [$\boldsymbol{E} \perp$ c-axis] and TM- [$\boldsymbol{E} \parallel$ c-axis] polarized $\eta_{extraction}$ of AlGaN-based nanowire DUV LEDs have been examined using 3D FDTD method, which has been widely used in optical property analysis of III-nitride emitters [25, 23, 24]. In particular, the light extraction properties of 230 nm nanowire LEDs with various nanowire sizes and passivation layer materials have been investigated, and the results have been compared with conventional planar AlGaN QW DUV LEDs.

6.2 Numerical Simulation of AlGaN-Based Nanowire UV LEDs

In this study, 3D FDTD simulations are used to analyze the $\eta_{extraction}$ and field distributions for AlGaN-based nanowire DUV LEDs at 230 nm. The layer structure of the simulated nanowire UV LED investigated in this study, as depicted in Figure 6.1(a), consists of 200 nm sapphire substrate, 1.5 μm n-AlN, 50 nm AlGaN layer to represent the multiple quantum wells (MQWs) active region, 100 nm p-AlGaN layer, and 25 nm SiO_2 passivation layer. The nanowire consists of a hexagonal shape MQW core of diameter D and height H surrounded by a 25-nm thick SiO_2 shell layer [Figure 6.1(b)], and is oriented along the c-axis, which is parallel to the z-direction labeled in Figure 6.1. The refractive indexes for sapphire, AlN, AlGaN, and SiO_2 layers are set as 1.9, 2.3, 2.4 and 1.52 respectively [72] while the absorption coefficients of the n-AlN, AlGaN active region and p-AlGaN are assumed to be 10 cm^{-1}, 1000 cm^{-1} and 11500 cm^{-1} respectively [70, 72]. The

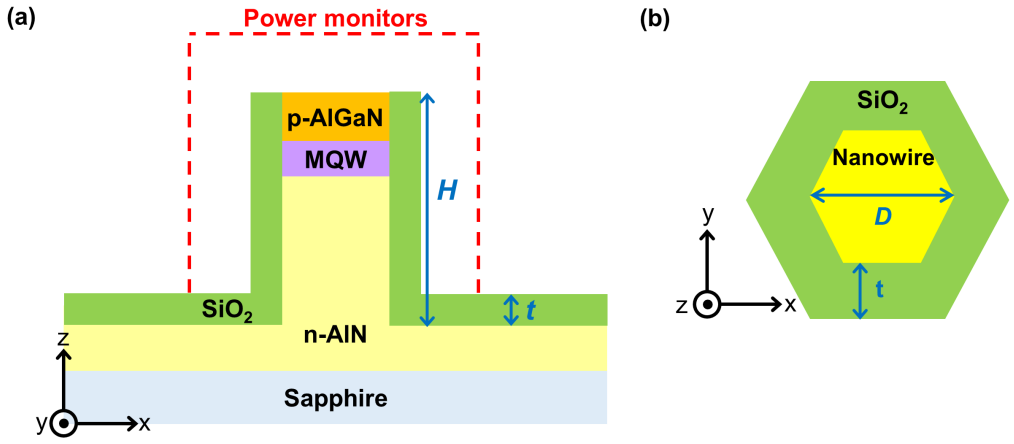

Figure 6.1: (a) Schematic of AlGaN-based nanowire UV LED with SiO_2 passivation layer, (b) cross-sectional view of nanowire from the top.

simulation domain is set to $\sim 2\lambda + D$ with non-uniform grid size (5 nm in the bulk and 2.5 nm at the edge). Perfectly matched layer (PML) boundary condition is applied to all the boundaries to absorb all outgoing waves incident upon it.

A single dipole source with $\lambda = 230$ nm is placed at the center of the AlGaN MQW active region where TE-polarization is defined as the major electric field travels in the in-plane direction [$\boldsymbol{E} \perp$ c-axis] while TM-polarization is represented by the major electric field travels in the out-of-plane direction [$\boldsymbol{E} \parallel$ c-axis]. Single dipole source has been used in this work as previous study has pointed out that the use of multiple dipole sources will result in non-physical interference pattern [75], which is undesirable for analysis of the optical properties of LEDs. A source power monitor surrounding the dipole source is used to measure the total power generated in the active region while output power monitors are placed at distance λ away from the nanowire to measure the light output power radiated out of the LED device. One field monitor is positioned at the center of the nanowire x-z plane to track the near-field electric field distribution along the nanowire. The $\eta_{extraction}$ is calculated as the ratio of the light output power measured by the output power monitors to the total emitted

power in the active region measured by the source power monitor [70]. Note that a single AlGaN-based nanowire structure is used here for analysis, which is commonly employed in the study of the optical properties of nanowire structure LEDs in both experimental and theoretical works [70, 93, 94, 95, 96].

A planar UV LED with a similar layer structure and thickness as the investigated nanowire UV LED depicted in Figure 6.1 has been investigated for comparison purposes. Due to the limitation of computation resources, the lateral simulation domain is set to 4 μm $\times$ 4 μm [23] with a non-uniform grid size of 5 nm in the bulk and 2.5 nm at the edge. The refractive indexes and absorption coefficients for AlN and sapphire layers are taken from Ref. [72] while for GaN layer is taken from Ref. [73]. Linear extrapolation between AlN and GaN is used in calculating the refractive indexes and absorption coefficients for p-AlGaN layer and AlGaN active region, where the Al-content for the corresponding emission wavelength is determined from Ref. [74]. In addition, a single output power detection plane located at distance λ away from the top of the p-type layer is used to measure the light output power radiated out of the planar LED device [23].

6.2.1 Planar Structure UV LEDs

Planar structure UV LEDs for $\eta_{extraction}$ ranges from 210 nm to 310 nm have been investigated for comparison purpose. Figure 6.2(a) illustrates the schematic of the planar structure AlGaN-based MQW UV LED with the corresponding layers thicknesses. The $\eta_{extraction}$ for each polarization as a function of λ is presented in Figure 6.2(b). The result shows that the planar LED always has higher TE-polarized $\eta_{extraction}$ ($\sim$1 – 4%) than TM-polarized $\eta_{extraction}$ ($\sim$0.1 – 0.4%) as λ changes from 210 to 310 nm, which is consistent with the result reported in previous analytical study for AlGaN-based UV LED emits at 280 nm ($\sim$4% for TE polarization and $\sim$0.4% for TM polarization) [70]. As planar structure favors light

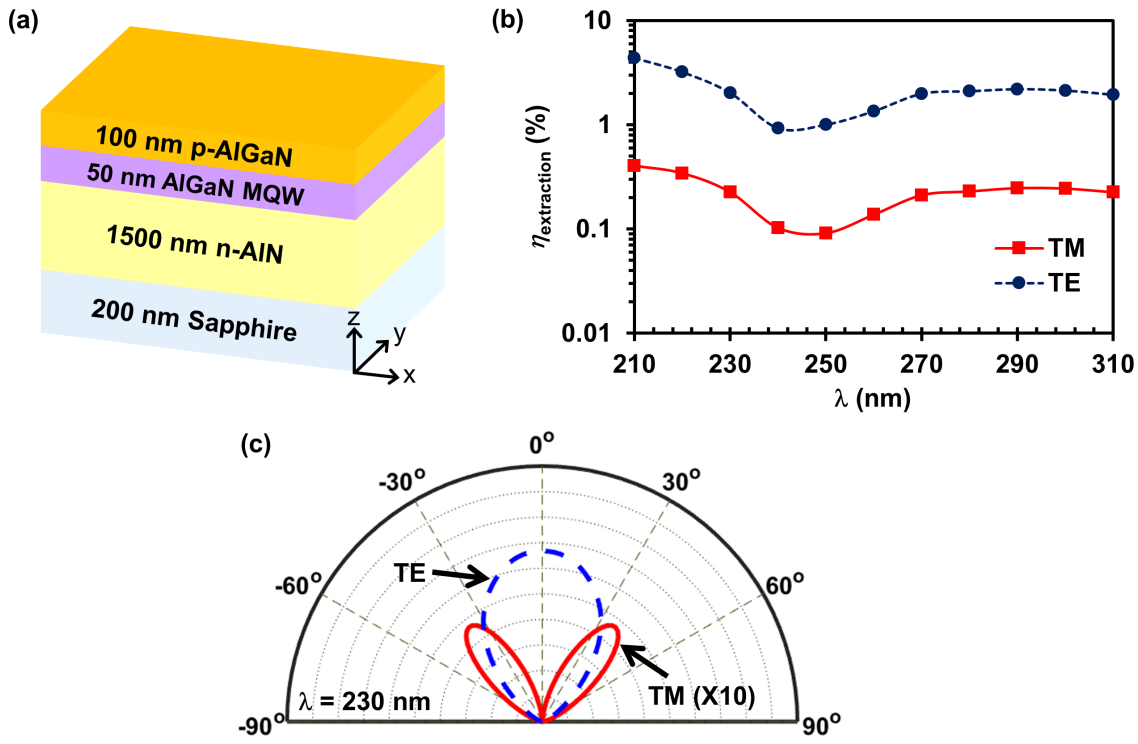

Figure 6.2: (a) Schematic of planar structure UV LED, (b) $\eta_{extraction}$ of the planar UV LEDs as a function of λ, (c) polar plot of far-field intensities of planar UV LEDs for $\lambda = 230$ nm.

extraction from the top/bottom surface (along c-axis) while TM-polarized light tends to emit at large angles with respect to c-axis, as evidenced by polar plot of the far-field intensities in Figure 6.2(c), majority of TM-polarized output will be trapped inside the planar structure due to total internal reflection, and eventually being re-absorbed by the LED device. As a result, smaller TM-polarized $\eta_{extraction}$ ($\sim$0.1 – 0.4%) is obtained, which is approximately one order of magnitude lower than the TE-polarized $\eta_{extraction}$ ($\sim$1 – 4%).

Despite the fact that the TE-polarized $\eta_{extraction}$ for AlGaN MQW planar LED is significantly higher than the TM-polarized $\eta_{extraction}$ for $\lambda \sim 210 - 310$ nm, it is very challenging to achieve large TE-R_{sp} for such wavelength regime, as shown in Figure 6.3. The spontaneous emission spectra of AlGaN/AlN QW with Al-content ranging from 50% to 80% at carrier density (n) of 5×10^{18} cm^{-3} presented in Figure 6.3

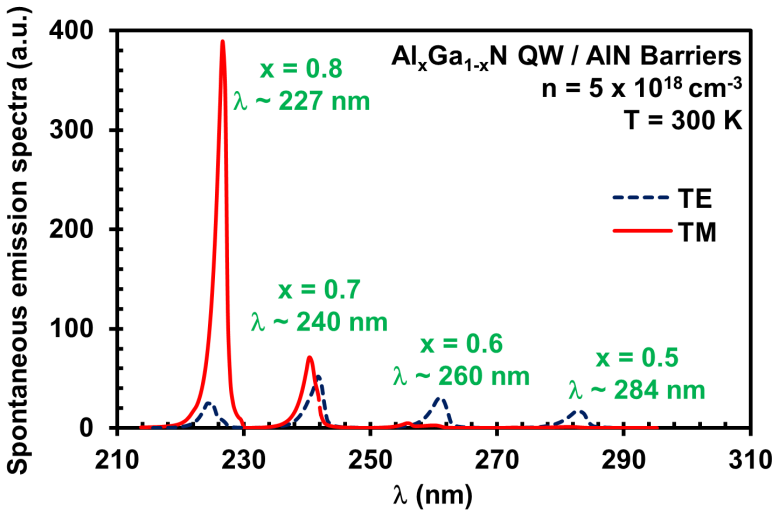

Figure 6.3: Spontaneous emission spectra for $Al_xGa_{1-x}N$ QW with various Al-composition plotted as a function of its corresponding emission wavelength at room temperature with carrier density, n = 5×10^{18} cm^{-3}.

were calculated based on the 6-band k·p formalism and taking into account strain effect, valence band mixing, spontaneous and piezoelectric polarization, as well as carrier screening effect [35, 97]. Due to the valence subbands crossover from the AlGaN QWs, only significantly large TM-polarized R_{sp} can be obtained at ~230 nm due to the dominant conduction band to CH subband transition (C-CH). However, even with this large TM-R_{sp} at 230 nm, it is still extremely challenging to realize high-efficiency planar structure 230 nm LEDs due to the extremely low TM-polarized $\eta_{extraction}$ (~0.2%) [Figure 6.2(b)]. Consequently, this provides a strong motivation to investigate the polarization-dependent $\eta_{extraction}$ of AlGaN-based nanowire UV LEDs, especially in the 230 nm regime, if a strong TM-polarized $\eta_{extraction}$ can be obtained otherwise.

6.2.2 Nanowire UV LEDs

The $\eta_{extraction}$ of the 230 nm nanowire LEDs for both TE- and TM-polarizations are examined here, and the results are presented in Figure 6.4 as a function of nanowire

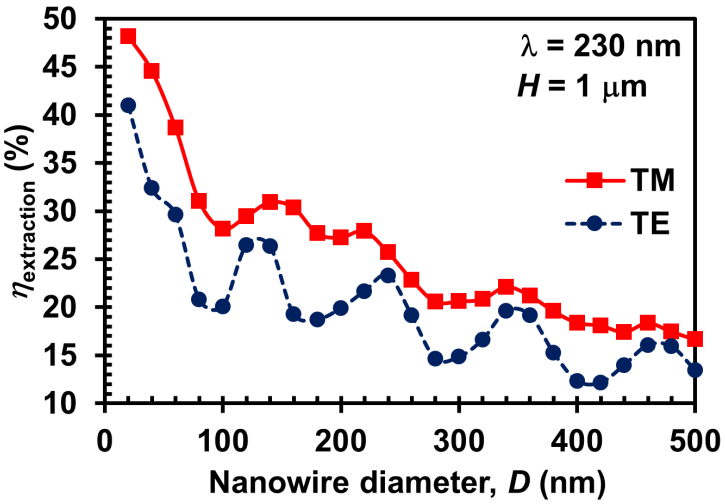

Figure 6.4: The $\eta_{extraction}$of the investigated nanowire UV LEDs as a function of diameter (D) ranges from 20 nm to 500 nm with $H = 1$ μm.

diameter (D) ranging from 20 nm to 500 nm with nanowire height (H) of 1 μm. The result shows that the nanowire structure favors TM-polarized emission, as the TM-polarized $\eta_{extraction}$ is consistently higher than the TE-polarized $\eta_{extraction}$ for the investigated nanowire D range. As an example, $\sim$45% of $\eta_{extraction}$ can be achieved for TM-polarized emission while $\sim$32% of $\eta_{extraction}$ is obtained for TE-polarized emission when $D = 40$ nm, which corresponding to $\sim$238-times and $\sim$17-times enhancement in the TM- and TE-polarized $\eta_{extraction}$ respectively as compared to the conventional planar structure. As D increases to 100 nm, the $\eta_{extraction}$ drops to $\sim$28% for TM-polarization and $\sim$20% for TE-polarization, but still, the $\eta_{extraction}$ is $\sim$149-times for TM-polarization and $\sim$10-times for TE-polarization higher than the conventional planar structure. In addition, the fluctuations in the $\eta_{extraction}$ for both TM- and TE-polarizations are due to the formation of resonant modes inside the nanowire core [70]. In contrast to the planar structure UV LEDs, nanowire structure with larger sidewall surface area is more efficient in extracting TM-polarized emission. As the dominant R_{sp} would be TM-polarized (Figure 6.3) for the corresponding AlGaN QW employed in the nanowire LED active region, significantly improved η_{EQE} would be expected

for the investigated nanowire UV LEDs as a result of the high TM-polarized $\eta_{extraction}$ and large TM-polarized R_{sp}. It is also interesting to point out that as D increases from 20 nm to 500 nm, the general trend of the $\eta_{extraction}$ for both TE- and TM-polarizations is gradually declined due to the slight decrease in the surface-to-volume ratio, which results in an increased portion of the light being trapped inside the LED nanowire structure.

Note that the effects of small nanowire D on the η_{IQE} is also an important consideration for the overall LED performance. Previous studies have shown that nanowire structure exhibits significantly reduced defect density, which in turn decreases the probability of non-radiative recombination at the defect sites. In addition, the reduced strain distribution in the nanowire structure induces smaller piezoelectric polarization field that results in negligible quantum confined Stark effect in the nanowire [26, 98, 99, 100, 101]. Therefore, the use of nanowire structure which favors TM-polarized light extraction, in conjunction with improved η_{IQE}, it is expected that the overall efficiency can be boosted which makes it an ideal candidate for high-efficiency TM-polarized DUV emitter.

The dependence of the $\eta_{extraction}$ for both TE- and TM-polarizations for the investigated nanowire UV LEDs with various nanowire H is presented in Figure 6.5. As H changes from 200 nm to 800 nm, the TM-polarized $\eta_{extraction}$ increases sharply from $\sim$21% to $\sim$44%, and levels off at $\sim$45% for $H > 800$ nm. Conversely, the nanowire H has less effect on the TE-polarized $\eta_{extraction}$ where it primarily oscillates between $\sim$30% and $\sim$35% as H changes from 200 nm to 1500 nm. The minimal changes in the $\eta_{extraction}$ for the TM-polarization emission when H varies from 800 nm to 1500 nm are due to the lateral propagation direction of TM-polarized photons that lead to strong photons extraction near the active region. Accordingly, longer nanowire will not result in significant photons extraction along the nanowire sidewall that is further away from the active region. For the case of

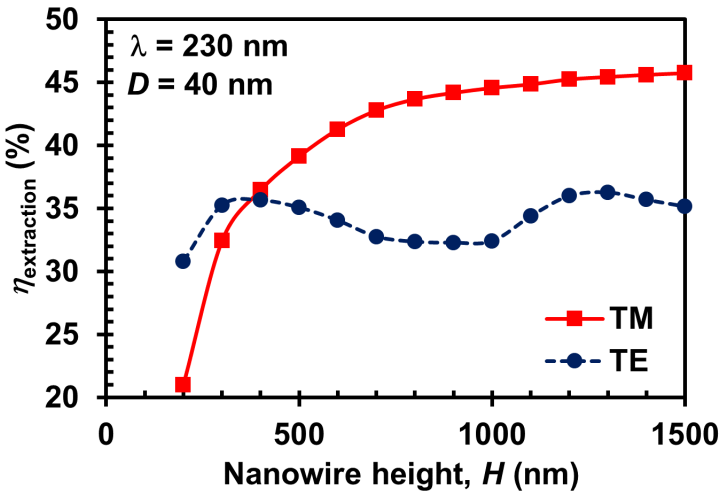

Figure 6.5: The $\eta_{extraction}$of the investigated nanowire UV LEDs as a function of H ranges from 200 nm to 1500 nm with D = 40 nm.

TE-polarization emission, since the majority of the TE-polarized photons are traveling in the vertical direction and being trapped inside the nanowire, only a small portion of TE-polarized photons can leak out through the nanowire sidewall. As a result, the formation of resonant modes inside the nanowire due to the severe photons trapping is causing the TE-polarized $\eta_{extraction}$ to fluctuate. Therefore, optimum nanowire H ranges between 800 nm and 1000 nm is preferable for the investigated nanowire UV LEDs when D = 40 nm.

In order to better understand the photon extraction by the use of nanowire structure, Figure 6.6 shows the electric field intensity distribution for the investigated nanowire UV LEDs at the x-z plane with various nanowire D. The nanowire H is fixed at 1 μm. For TM-polarized emission (top row figures of Figure 6.6), the majority of the light is traveling in the lateral direction while very limited photons are propagating in the vertical direction. As a result, TM-polarized light can easily escape through the nanowire sidewall, especially for nanowire structure with small D [Figure 6.6(a)], which results in significantly improved TM-polarized $\eta_{extraction}$ (~45% for the case of D = 40 nm) as compared to the

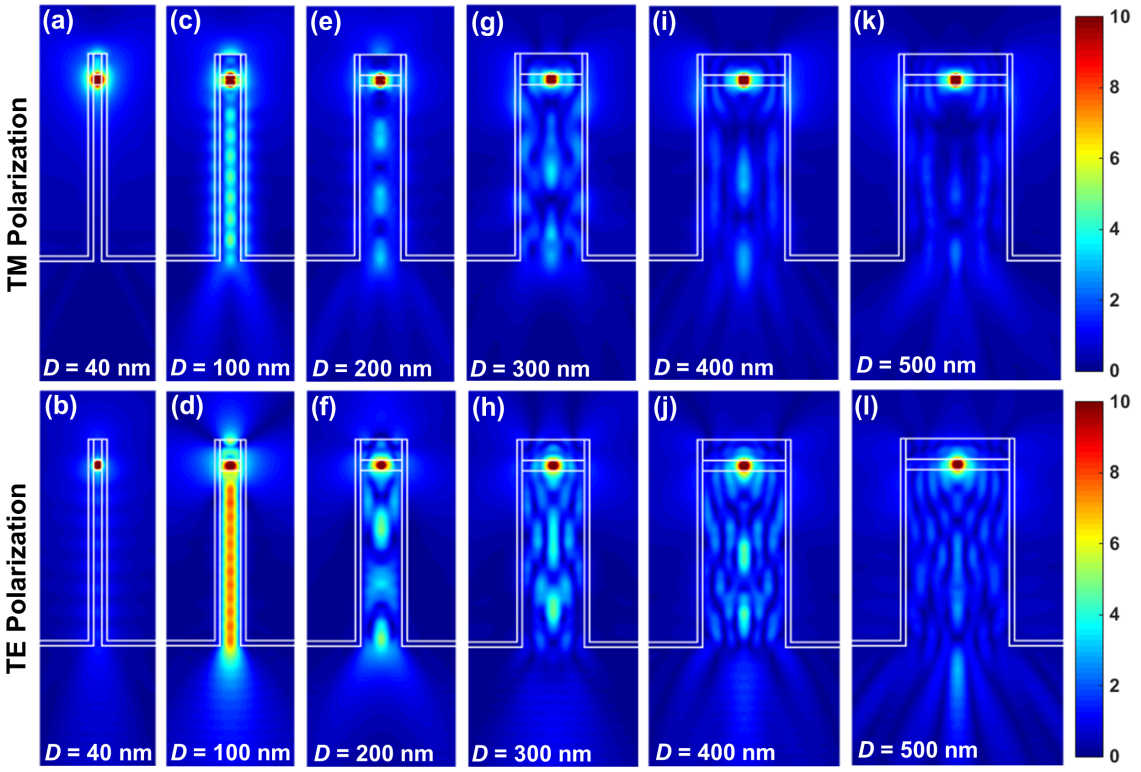

Figure 6.6: Cross-sectional near-field electric field intensity of the investigated nanowire UV LEDs with $H = 1$ μm and various D for TM-polarization (top row figures) and TE-polarization (bottom row figures) at the x-z plane.

conventional planar structure (∼0.2%). In contrast, TE-polarized photons (bottom row figures of Figure 6.6) are mainly propagating in the vertical direction which can only be extracted out from the top and bottom sides of the nanowire while very limited photons are emitted in the lateral direction to be extracted out through the nanowire sidewall. Due to the absorption by the p-AlGaN layer and the undesired bottom emitting through the sapphire substrate, lower TE-polarized $\eta_{extraction}$ is obtained as compared to the TM component [Figure 6.4(a)]. Nevertheless, the $\eta_{extraction}$ for both TM- and TE-polarizations by the use of nanowire structure is still larger than the conventional planar structure. For nanowire structure which has a large surface-to-volume ratio, photons can be escaped into the air medium much easier through the nanowire sidewall than conventional planar structure as photons

in conventional planar structure can only be extracted out through the top or bottom surface of the devices. As the emission from 230 nm LED is strongly TM-polarized (Figure 6.3), strong sidewall TM-polarized photons extraction by the use of nanowire structure is expected to improve the overall UV LED performance significantly.

The electric field intensity plots presented in Figure 6.6 also provide insight into the impact of nanowire structural parameters on the $\eta_{extraction}$. For nanowire UV LED with D = 40 nm and H = 1 μm, majority of TM-polarized photons are escaped through the sidewall of the nanowire [Figure 6.6(a)] while TE-polarized photons are generally trapped along the nanowire [Figure 6.6(b)]. As D increases to 100 nm [Figures 6.6(c) and 6.6(d)], the trapping of photons becomes more obvious for both TM- and TE-polarizations due to the weak micro-cavity effect. Nevertheless, significant amount of photons can still be extracted out through the nanowire sidewall for TM-polarized emission, even though the strong photons confinement inside the nanowire structure for both polarizations result in a lower $\eta_{extraction}$ ($\sim$28% and $\sim$20% for TM- and TE-polarizations respectively) as compared to the case of D = 40 nm ($\sim$45% and $\sim$32% for TM- and TE-polarizations respectively). Further increases the nanowire D [Figures 6.6(e) – 6.6(l)] will lead to more photons trapping inside the nanowire structure and fewer photons extraction. However, due to the increment of photon absorption by the larger p-type layer area and weaker resonant effect in larger dimension nanowire, the electric field intensity along the nanowire is getting weaker as compared to the case of D = 100 nm. For that reason, the ideal nanowire DUV LED is recommended to avoid nanowire design that strongly confines TM-polarized photons as well as nanowire structure with a large area of p-type doping layer, which is $D > 80$ nm for the investigated nanowire UV LED structures with H = 1 μm, in order to achieve high efficiency DUV LEDs. While the nanowire D undeniably plays a vital role in

the $\eta_{extraction}$, it is worth noting that longer nanowire with extended n-AlN region does not contribute to significant photons extraction since most of the near-field electric field intensity is concentrated around the AlGaN MQW active region. As a result, the light extraction through the nanowire sidewall region that is further away from the active region is very limited, especially for the case of $D \geq 100$ nm [Figures 6.6(c) – 6.6(l)]. Therefore, the $\eta_{extraction}$ remains nearly constant (∼45% for TM-polarization and ∼30 – 35% for TE-polarization) even though the nanowire H increases from 800 nm to 1500 nm [Figure 6.4(b)].

6.2.3 Passivation Layer for Nanowire UV LEDs

The large surface area for nanowire structure gives rise to the presence of high surface density state that contributes significantly to non-radiative recombination near the surface, which in turn will lead to degraded quantum efficiency and lower output power for nanowire devices [87, 102]. Therefore, the passivation layer for nanowire structure plays an important role in suppressing the surface recombination arising from the surface states. On the other hand, the choice of passivation layer material and its corresponding thickness are critical for $\eta_{extraction}$ as the passivation layer could possibly impede the light extraction if the design is not optimized. Ideally, it is preferred for the passivation layer to appear transparent in the LED emission range, and have smaller refractive index than the nanowire core structure to minimize the cavity effects that cause severe photons trapping within the nanowire core. This increases the possibility of photon extraction which in turn contributes to larger $\eta_{extraction}$.

In order to examine the effect of the passivation layer on the TM-polarized $\eta_{extraction}$ for nanowire DUV LED, the nanowire UV LEDs with 3 different commonly used passivation layers for nitride-based LED – SiO_2, SiN_x and AlN, have been studied. At $\lambda = 230$ nm, the refractive indexes of SiO_2, SiN_x and AlN are 1.52,

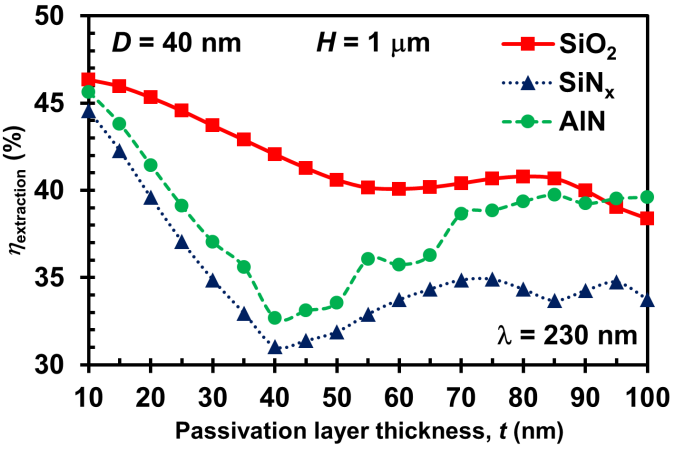

Figure 6.7: The TM-polarized $\eta_{extraction}$ of the investigated nanowire UV LEDs with different passivation layer materials as a function of passivation layer thickness (t) with nanowire $H = 1$ μm and $D = 40$ nm.

2.35 and 2.3 respectively [72]. SiO_2 layer appears transparent for the investigated wavelength regime ($\lambda = 230$ nm) with negligible absorption while SiN_x and undoped AlN layers are assumed to have absorption coefficient of 11000 cm^{-1} and 10 cm^{-1} respectively [70, 72]. The TM-polarized $\eta_{extraction}$ presented in Figure 6.7 as a function of passivation layer thickness (t) ranges from 10 nm to 100 nm shows that nanowires with SiO_2 passivation layer exhibit the highest $\eta_{extraction}$than nanowires with SiN_x or AlN passivation layer. The SiO_2 passivation layer with smaller refractive index ($n = 1.52$) than the nanowire core ($n = 2.4$) can prevent the existence of strong cavity effect inside the nanowire core that traps photons due to reduced total internal reflection. At the same time, SiO_2 also has the lowest absorption coefficient compared to SiN_x and AlN, which in turn will lead to more photons extraction that contributes to higher $\eta_{extraction}$. For SiN_x and AlN, even though the refractive indexes for these two materials are very similar, SiN_x has larger photon absorption than AlN. As a result, smaller $\eta_{extraction}$ are observed for nanowires with SiN_x passivation layer.

Although both refractive index and absorption coefficient of the passivation layer are critical to the $\eta_{extraction}$, varies passivation layer thicknesses will also affect the photon extraction through the nanowire sidewall. As shown in Figure 6.7, nanowire UV LEDs with 40 nm nanowire D, 1 μm nanowire H and 10 nm thin passivation layer for all 3 different passivation layer materials exhibit very similar TM-polarized $\eta_{extraction}$ ($\sim$45 – 47%) as the properties of the extremely thin passivation layer only have minor effect on the photons. When t increases to 40 nm, which is similar to the nanowire D, the TM-polarized $\eta_{extraction}$ for nanowire with SiN_x and AlN passivation layer declines substantially to $\sim$31 – 33% due to total internal reflection and the coupling of resonant modes between the nanowire core and the passivation layer, while the TM-polarized $\eta_{extraction}$ for nanowire with SiO_2 passivation layer only decreases marginally to 42%. Further increasing the SiO_2 passivation layer thickness beyond 40 nm will result in even smaller TM-polarized $\eta_{extraction}$ ($\sim$38% with t = 100 nm) due to photons trapping inside the thick passivation layer that lead to larger coupling effects between the passivation layer and the nanowire core. However, for the case of the nanowire with SiN_x and AlN passivation layer, thicker passivation layer ($>$ 40 nm) is resulting in less severe photons trapping inside the nanowire core as the refractive indexes for SiN_x and AlN is very similar with the nanowire core. TM-polarized photons that travel laterally can easily move around the passivation layer and the nanowire core, which results in the formation of weak resonant modes in these two layers. Consequently, the weak coupling effects between resonant modes in the nanowire core and the passivation layer will lead to a gradual increase in the TM-polarized $\eta_{extraction}$. For example, $\eta_{extraction}$ of $\sim$35% and $\sim$39% are achieved for 75-nm thick SiN_x and AlN as passivation layer respectively. For nanowire with AlN passivation layer $t > 75$ nm, the TM-polarized $\eta_{extraction}$ remains nearly constant, and is very similar to that of the nanowire with SiO_2 passivation layer ($\sim$40% for both cases) attributed to the weaker resonant modes in the thick AlN passivation layer

and subsequently smaller coupling effects. The TM-polarized $\eta_{extraction}$ for nanowire with SiN_x passivation layer stays below ~35% as $t > 75$ nm due to the large photon absorption by the SiN_x material.

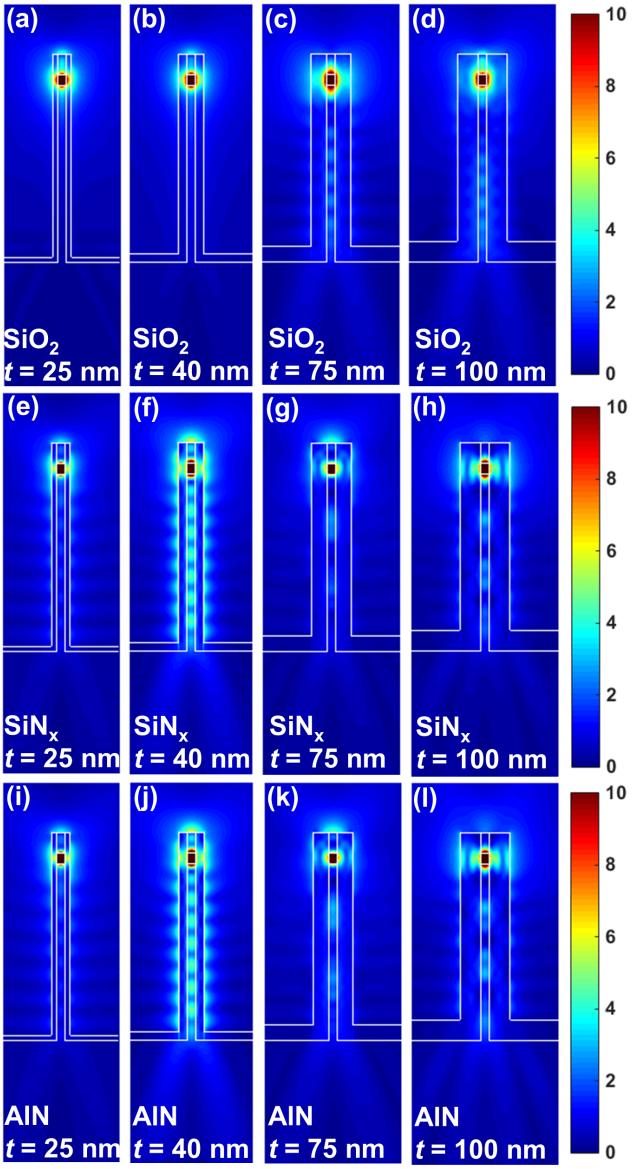

Figure 6.8: Cross-sectional near-field electric field intensity of the investigated nanowire UV LEDs with various passivation layer materials for TM-polarization at the x-z plane. The nanowire D and H are fixed at 40 nm and 1 μm respectively.

To further understand the effect of various passivation layer designs to the TM-polarized $\eta_{extraction}$, the electric field intensity distribution of nanowire with 25 nm,

40 nm, 75 nm, and 100 nm thick passivation layer for SiO_2, SiN_x and AlN materials are presented in Figure 6.8. The nanowire H and D are fixed at 1 μm and 40 nm respectively. As clearly illustrated in the electric field intensity plots, for nanowire with thin SiO_2 passivation layer (t $\leq$ 40 nm) [Figures 6.8(a) and 6.8(b)], the TM-polarized photons, which are primarily concentrated near the active region, can easily penetrate through the thin passivation layer and result in large $\eta_{extraction}$ ($\sim$42 – 47%). Further increases the SiO_2 passivation layer thickness will result in some photons trapping along the nanowire core and the thick SiO_2 passivation layer [Figures 6.8(c) and 6.8(d)]. Consequently, the coupling of light between the nanowire core and SiO_2 passivation layer is resulting in a marginal reduction in the TM-polarized $\eta_{extraction}$ to $\sim$38% when $t = 100$ nm. For the case of 25 nm and 40 nm thin SiN_x or AlN passivation layers [Figures 6.8(e), 6.8(f), 6.8(i) and 6.8(j)], majority of the TM-polarized photons suffer from total internal reflection which result in severe photons trapping along the nanowire core. As a result, the TM-polarized $\eta_{extraction}$ drops significantly from $\sim$45 – 46% with $t = 10$ nm to $\sim$31 – 33% with $t = 40$ nm. As t increases beyond 40 nm [Figures 6.8(g), 6.8(h), 6.8(k) and 6.8(l)], despite the formation of resonant modes inside the thick passivation layer, the photons trapping along the nanowire core is less severe than the case of $t = 40$ nm. Subsequently, it leads to an upsurge in the TM-polarized $\eta_{extraction}$, $\sim$34% and $\sim$40% for nanowire with 100 nm thick SiN_x and AlN passivation layer respectively.

Therefore, in order to counterbalance the benefit of the passivation layer in suppressing high surface density states and the negative impact of the passivation layer on the $\eta_{extraction}$, SiO_2 and AlN are the preferred choices over SiN_x as the passivation layer materials for the investigated DUV nanowire LEDs. In particular, varying the thickness of SiO_2 passivation layer only has minimal impact on the TM-polarized $\eta_{extraction}$, which make it an ideal candidate as a nanowire passivation layer. Nevertheless, considering the needs of a much straightforward fabrication

step, AlN is in favor over SiO_2 as the former material can be grown in the same growth chamber as the nanowire core. It is recommended for nanowire with AlN passivation layer to have different passivation layer thickness than the nanowire D to minimize the strong coupling of resonant modes between the nanowire core and the passivation layer. In addition, previous experimental studies on Nitride-based nanowire with AlGaN shell structure has reported that the use of rich Al-content AlGaN shell layer can effectively suppress the non-radiative recombination [26, 103], which can lead to improved η_{IQE}. Accordingly, thick AlN (> 75 nm) is expected to achieve high η_{EQE} for nanowire UV LEDs with AlN as a passivation layer.

6.3 Conclusion

The TE- and TM-polarized $\eta_{extraction}$ of AlGaN-based nanowire LEDs emit at 230 nm with various nanowire structural parameters and passivation layers have been investigated intensively. Simulation results show that TM-polarized $\eta_{extraction}$ up to $\sim$48% and TE-polarized $\eta_{extraction}$ up to $\sim$41% can be achieved with nanowire structure of various nanowire D and H as compared to the conventional planar structure ($\sim$0.2% for TM-polarization and $\sim$2% for TE-polarization). Smaller nanowire D (< 60 nm) enables more photons to leak out through the nanowire sidewall that results in higher $\eta_{extraction}$ while increases the nanowire H beyond 800 nm has less impact on the $\eta_{extraction}$. In addition, the choice of passivation layer material and its corresponding thickness are also critical to the $\eta_{extraction}$. The use of SiO_2 as a passivation layer which has a smaller refractive index than the nanowire core can result in larger $\eta_{extraction}$ as compared to SiN_x and AlN. While varying the SiO_2 passivation layer thickness has minimal impact on the $\eta_{extraction}$, the thicknesses of SiN_x and AlN passivation layers are affecting the $\eta_{extraction}$ substantially. In summary, the investigated 230 nm nanowire LEDs with $D < 60$

nm, H ranges between 800 nm and 1000 nm, and thick SiO_2 or AlN ($>$ 75 nm) passivation layer are anticipated to improve the η_{EQE} significantly attributed to the high TM-polarized $\eta_{extraction}$ and large TM-polarized R_{sp}, which are expected to be promising solutions to high-efficiency TM-polarized DUV emitters. Future work to address the impact of various nanowire design within an array of nanowires such as uniformity in nanowire diameter, height, spacing, and peak emission wavelength as well as QW position is desired in order to provide more comprehensive modeling of the nanowire LED performance.

Chapter 7

III-Nitride Plasmonic Nanowire LEDs

This chapter presents an alternative approach to enhance the performance of III-nitride light-emitting diodes (LEDs) by the use of surface plasmonic effect. In particular, green plasmonic LEDs with nanowire structure coated with 5 nm of Al_2O_3 as a dielectric layer and various Ag cladding layer thicknesses are investigated using three dimensional (3D) finite-difference time-domain (FDTD) method. The results show that a Purcell factor of ∼80 can be obtained for the investigated plasmonic nanowire LEDs with light extraction efficiency ($\eta_{extraction}$) of ∼65% when the Ag thickness > 60 nm. Strong near-field electric field intensity at the dielectric/metal interface confirms the existence of plasmonic effect in the active region.

7.1 Introduction

A novel method to enhance the efficiency of III-nitride LEDs utilizing surface plasmonic effects have drawn tremendous attention in the past decades. The mechanism is based on the energy coupling effect between the emitted photons from

the LED and metallic layer to result in enhanced radiative recombination efficiency (η_{rad}). A plasmon is a quasiparticle describing the collective oscillation of free electron gas in a metal, and surface plasmon (SP) refers to those plasmons that are confined at the interface between a dielectric material and a metal. The coupling of surface plasmon with photon creates another quasiparticle called surface plasmon polariton (SPP). As the SPP is one of the electromagnetic wave modes, it can interact with light waves at the interface to bring novel optical properties to the materials. The primary advantage of employing SPPs in III-nitride emitters is its short lifetime that leads to higher recombination rate of SPPs as compared to radiative and non-radiative recombination processes in the LEDs. As a result, higher internal quantum efficiency (η_{IQE}) can be achieved.

Investigation on the various designs of surface plasmon-based III-nitride LEDs with planar structure have reported promising results in the LED performance, especially in the visible light region [104, 105, 31, 30, 106, 107, 108, 109, 110, 111], as SP energy of Ag and Au on GaN are approximately 2.76 eV (450 nm) and 2.2 eV (560 nm) respectively [112]. For instance, a 14-fold enhancement in peak photoluminescence (PL) intensity is observed from the Ag-coated InGaN LED [111], and the use of a double metallic Au/Ag layers has reported up to 8.3-times enhancement in PL intensity in green spectral regime [30]. Implementation of green LEDs with Ag nanoparticles has also demonstrated up to 150% enhancement in electroluminescence (EL) peak intensity [109]. Due to the exponential decay of the evanescent SPP field, the metal has to place in close proximity to the quantum well (QW). Previous study has shown that the enhancement factor in PL intensity reduced from 14 with 10 nm distance to 4 with 40 nm distance [111]. This poses technological challenges for planar structure III-nitride LEDs as a thick p-type layer is typically desired to allow better holes injection to the LED device. On the other hand, large sidewall surface area for nanowires expose the active region and

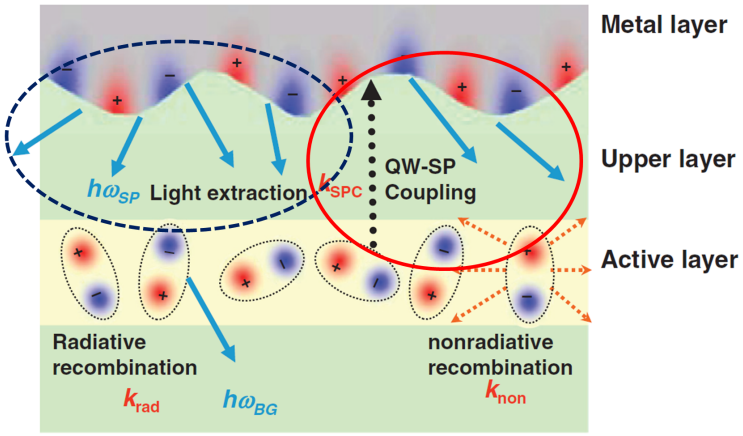

Figure 7.1: Schematic diagram of the electron-hole pair recombination and quantum well-surface plasmon coupling mechanism [112].

eliminate the requirement of a thin p-type layer, which can be an alternative structure for III-nitride plasmonic LEDs. Therefore, in this study, we propose and investigate the LED performance of III-nitride plasmonic nanowire LEDs of diameter 350 nm coated with 5 nm of Al_2O_3 as a dielectric layer and various thicknesses of Ag cladding layer.

7.2 Mechanism for Plasmon-Coupled Emission in III-Nitride LEDs

The mechanism for QW coupling and light extraction for plasmonic LED is illustrated in Figure 7.1. The enhancement in LED efficiency is coming from a two-step process: enhanced spontaneous emission (red solid line circle in Figure 7.1) followed by extraction of light from the SPP modes (blue dash line circle in Figure 7.1). For conventional LED without a metal layer on top, the carriers in the active layer are terminated by the radiative or non-radiative recombination, and the

η_{rad} is defined by the ratio of these two recombination processes as followed:

$$\eta_{rad} = \frac{k_{rad}}{k_{rad} + k_{non}} \tag{7.1}$$

where k_{rad} is the radiative recombination rate, and k_{non} is the non-radiative recombination rate. On the contrary, when a metal layer is deposited within the near field of the active layer for plasmonic LED, the electron-hole pairs in the active region can be coupled to SPP modes at the interface between the metallic layer and GaN (red solid line circle in Figure 7.1) if the band gap energy of the QW is close to the electron oscillation energy of SP at the metal/semiconductor interface. The new η_{rad} can then be expressed by the following equation:

$$\eta_{rad} = \frac{k_{rad} + Ck_{spc}}{k_{rad} + k_{non} + k_{spc}} \tag{7.2}$$

where k_{spc} is the SP coupling rate, and C is the probability of photon extraction from the SPs energy. The k_{spc} should be very fast because the density of states of SP modes are much larger than that of the electron-hole pairs in the QW, while C is decided by the ratio of light scattering and disposal of the SPP modes through non-radiative loss. If the k_{spc} is much faster than k_{rad} and k_{non}, the η_{IQE} should dramatically increase. The key requirements in this respect are near-field proximity between the active region and the metal surface, and close matching between the emission wavelength and the SPP resonance.

The emission efficiency enhancement of a radiating dipole near a metal can be interpreted with the Purcell effect, which quantifies the increase in spontaneous emission rate into a mode of interest by setting $C \approx 1$ [111]:

$$F_p = \frac{k_{rad} + k_{non} + k_{spc}}{k_{rad} + k_{non}} \approx \frac{1 - \eta_{rad}}{1 - \eta^*_{rad}} \tag{7.3}$$

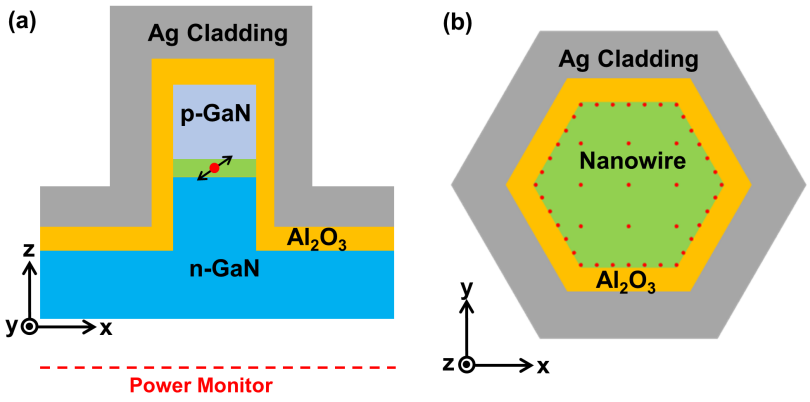

Figure 7.2: (a) Schematic of InGaN-based green plasmonic nanowire LED with Al_2O_3 dielectric layer and Ag thin film. (b) The cross-sectional view of plasmonic nanowire from the top with radius $R = 175$ nm. The red spots mark the location of dipole sources.

where η^*_{rad} is the enhanced radiative recombination rate from the plasmonic LED.

In addition to those photons generated in the active region, the SPP energy can also be extracted as light due to the scattering of high-momentum SPPs (blue dash line circle in Figure 7.1). Consequently, higher $\eta_{extraction}$ can be achieved from the extraction of both photons generated in the active region and from the SPPs.

7.3 Numerical Simulation of III-Nitride Plasmonic Nanowire LEDs

In this study, 3D FDTD method has been employed to analyze the $\eta_{extraction}$ and Purcell factor for InGaN-based green plasmonic nanowire LEDs. The layer structure of the simulated nanowire LED investigated in this study, as depicted in Figure 7.2(a), consists of 100 nm sapphire substrate, 800 nm n-GaN, 150 nm InGaN layer to represent the multiple quantum wells (MQWs) active region and 150 nm p-GaN layer. The nanowire consists of a hexagonal-shaped MQW core with radius $R = 175$ nm and height $H = 1$ μm (700 nm n-GaN, 150 nm InGaN MQWs and 150

nm p-AlGaN layer), surrounded by 5 nm of Al_2O_3 and Ag thin film [Figure 7.2(b)], and is oriented along the c-axis, which is parallel to the z-direction labeled in Figure 7.2. The dimension of the nanowire (R = 175 nm and H = 1 μm) used in this study is chosen based on the nanowires fabricated in house using nanosphere lithography method discussed in Chapter 5. The refractive indexes for sapphire, GaN, InGaN, Al_2O_3 and Ag layers are set as 1.78, 2.39, 2.5, 1.54 and $0.13+3.15i$ respectively [72, 71] while the absorption coefficients of the GaN and InGaN are assumed to be 10 cm^{-1} and 2000 cm^{-1} respectively [71]. The simulation domain is set to 700 nm $\times$ 700 nm with a non-uniform grid size of 10 nm in the bulk and 2.5 nm at the edge. Perfectly matched layer (PML) boundary condition is applied to all the boundaries to absorb all outgoing waves incident upon it.

A dipole source with emission wavelength 530 nm is placed in the active region, and the simulation is repeated for each dipole source location marked in Figure 7.2(b). Single dipole source has been used for each simulation as previous study has pointed out that the use of multiple dipole sources will result in non-physical interference pattern [75], which is undesirable for analysis of the optical properties of LEDs. A power monitor is placed at 200 nm away from the bottom of the simulated structure to collect the light output power radiated out of the simulated device through the sapphire substrate. Only transverse electric (TE)-polarized light (major electric field travels in the in-plane direction) is considered in this study since emission from InGaN-based active region has been reported to be primarily TE-dominant [113]. A source power monitor surrounding the dipole source is used to measure the total power generated in the active region, and a field monitor is positioned at 7 nm above the InGaN active region to track the near-field electric field distribution in the x-y plane of the nanowire. The $\eta_{extraction}$ is calculated as the ratio of the light output power measured by the output power

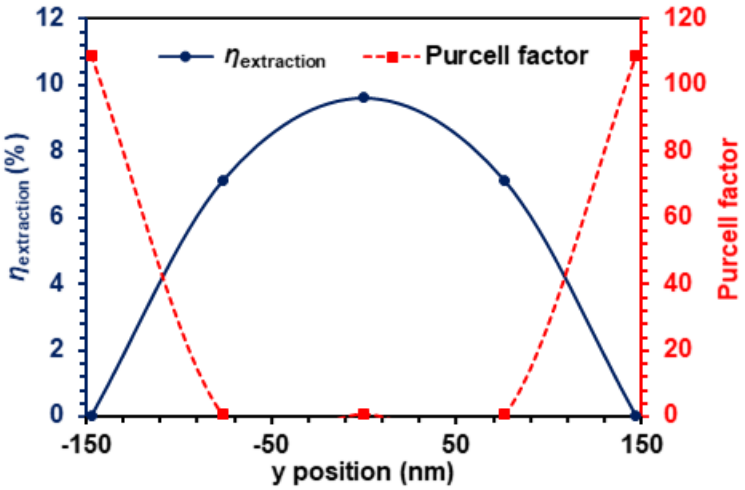

Figure 7.3: The $\eta_{extraction}$ and Purcell factor of the investigated plasmonic nanowire LEDs with dipole source at various locations along the y-axis in the active region.

monitor to the total emitted power in the active region measured by the source power monitor [70] while Purcell factor is calculated by averaging the source powers.

7.3.1 Various Dipole Emitter Locations

Figure 7.3 shows the $\eta_{extraction}$ and Purcell factor for the investigated plasmonic nanowire LEDs with the dipole emitter placed at various vertical locations along y-axis labeled in Figure 7.2 in the active region. The location of the dipole emitter is swept from y = -147 nm to 147 nm for nanowire with a radius of 175 nm and the silver thickness (H_{Ag}) of 40 nm. As shown in the results, the Purcell factor increases when the dipole emitter moves toward the silver cladding layer while the $\eta_{extraction}$ decreases. In particular, the Purcell factor for the plasmonic nanowire LED with Ag thickness of 40 nm increases from ∼1 when the dipole emitter is placed at the center of the nanowire (x = 0, y = 0) to ∼109 when the dipole source is located near the Ag cladding layer (x = 0, y = 147 nm), while the $\eta_{extraction}$ drops from ∼9.6% to 0.02%. The results show that there is a trade-off between the Purcell factor and the $\eta_{extraction}$. The dipole emitter located closed to the Ag cladding layer is experiencing

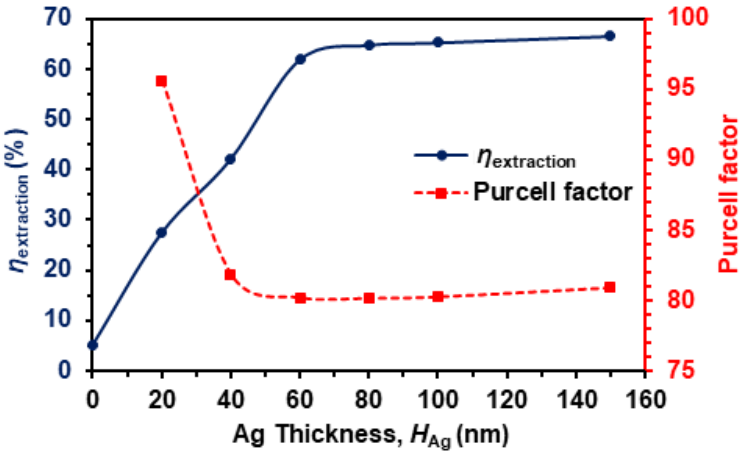

Figure 7.4: The $\eta_{extraction}$ and Purcell factor of the investigated plasmonic nanowire LEDs as a function of Ag cladding layer thickness.

strong plasmonic effect that results in higher Purcell factor as compared to those dipole emitters further away from the Ag cladding layer. At the same time, the $\eta_{extraction}$ reduces significantly due to the metal absorption when the dipole source moves closer to the Ag cladding layer. In order to minimize the effect of location-dependent $\eta_{extraction}$ and Purcell factor, the simulation is repeated by varying the location of the dipole emitter each time, as indicated in Figure 7.2(a), then taking the average of the results from all dipole emitters to calculate the $\eta_{extraction}$ and Purcell factor.

7.3.2 Various Ag Thicknesses

The $\eta_{extraction}$ and Purcell factor of the investigated plasmonic nanowire LEDs coated with 5 nm of Al_2O_3 and various Ag cladding layer thicknesses are presented in Figure 7.4. The $\eta_{extraction}$ and Purcell factor are calculated by averaging all results from all dipole emitters at various locations. For bare nanowire without Ag cladding layer ($H_{Ag} = 0$), the $\eta_{extraction}$ is shown to be ~5%. When 20 nm of Ag is deposited on the nanowire sidewalls, the $\eta_{extraction}$ increases to ~27% with Purcell factor around 96. Further increases the Ag cladding layer thickness to 60 nm is

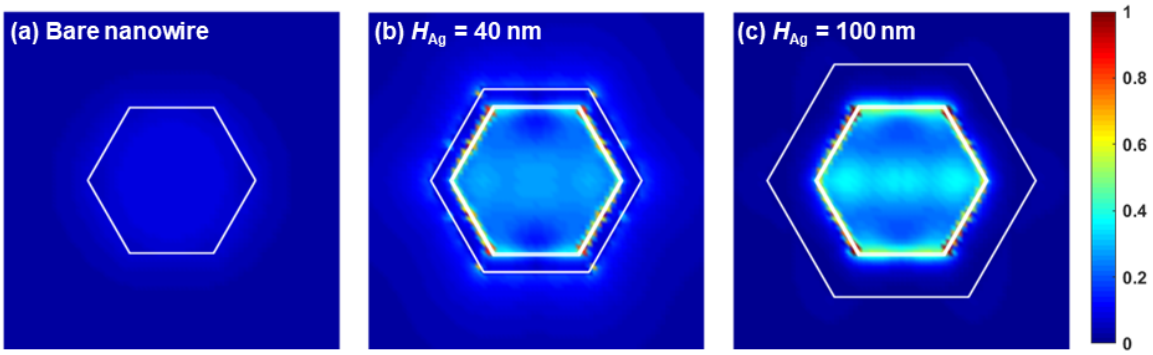

Figure 7.5: Cross-sectional near-field electric field intensity of (a) bare nanowire LED without Al_2O_3 and Ag cladding layer, and the investigated plasmonic nanowire LEDs with 5 nm of Al_2O_3 and Ag thickness of (b) 40 nm and (c) 100 nm.

found to further enhance the $\eta_{extraction}$ to ~62% attributed to better reflectance for the thicker metal film, and the $\eta_{extraction}$ tends to level off at ~65% even if H_{Ag} changes from 80 nm to 150 nm. On the contrary, the Purcell factor only drops minimally from 96 to 82 when H_{Ag} changes from 20 nm to 40 nm, and levels off at ~80 for $H_{Ag} > 40$ nm. From the analysis, 60 nm of Ag cladding layer is adequate to achieve high $\eta_{extraction}$ and large Purcell factor for the investigated plasmonic nanowire LEDs. The reflectance from thin Ag film ($H_{Ag} < 60$ nm) may not be sufficient to achieve maximum $\eta_{extraction}$ while thicker Ag cladding layer ($H_{Ag} > 60$ nm) may not be necessary since the Purcell factor only changes marginally. In fact, it is favorable to observe both $\eta_{extraction}$ and Purcell factor to be independent of the Ag thickness since it is an elaborating task to control and measure the thickness of the metal on the nanowire sidewalls deposited using evaporator.

The existence of plasmonic effect in the investigated plasmonic nanowire LEDs is evidenced by the cross-sectional near-field electric field intensity plots presented in Figure 7.5. The cross-sectional electric field for bare nanowire without Al_2O_3 dielectric layer and Ag cladding layer [Figure 7.5(a)] is shown for comparison while Figures 7.5(b) and 7.5(c) show the cross-sectional electric field plots for plasmonic nanowire LEDs with 5 nm of Al_2O_3, and 40 nm and 100 nm of Ag cladding layers

respectively. As can be observed in the figure, strong electric field exists at the dielectric/Ag interface attributed to the coupling of the photons to the SPPs. As a result, higher η_{IQE} can be expected if the photons extraction rate from the SPs energy is higher than the non-radiative decay rate of the SPPs (C parameter in Equation 7.2). Thus, a high Purcell factor is desired for high-speed operation. In addition, Figure 7.5 also shows that higher electric field intensity can be observed at the core of nanowire for plasmonic nanowire LEDs [Figures 7.5(b) and 7.5(c)] as compared to bare nanowire LED [Figure 7.5(a)] attributed to the reflectance from the Ag film, which results in higher $\eta_{extraction}$.

7.4 Conclusion

In summary, a preliminary study on III-nitride plasmonic nanowire green LEDs has been carried out, and the results show that large $\eta_{extraction}$ (∼65%) and high Purcell factor (∼80) can be achieved for the investigated plasmonic nanowire LEDs with $H_{Ag} > 60$ nm. Both the $\eta_{extraction}$ and Purcell factor are inferred to be uncorrelated with the thickness of the Ag cladding layer > 60 nm, which is desired due to the complication in controlling the metal thickness through evaporation. Future analysis on smaller nanowire diameters, various dielectric layer materials such as SiO_2 and TiO_2, as well as various designs of the nanowire, for instance, torchlight-shaped nanowires shown in Figure 2.10 which has larger surface area for the active region as compared to cylinder-shaped nanowires investigated in this study, are essential to provide a comprehensive analysis on the use of nanowire structure as plasmonic LEDs to enhance the LED performance. As stated previously, a high Purcell factor is desired for high-speed operation. However, this does not indicate enhancement in η_{IQE} as the latter is also depending on the probability of photons extraction from the SPs energy, as described in Equation 7.2.

Therefore, this theoretical analysis serves as a guide on the design of plasmonic nanowire LEDs in order to obtain large $\eta_{extraction}$ and Purcell factor, while experimental study is necessary to examine the decay rate of the SPPs.

Chapter 8

3D Printed Lens on III-Nitride LEDs

In this chapter, the integration of three-dimensional (3D) printing process with InGaN-based light-emitting diode (LED) as a straightforward and highly reproducible method to improve light extraction efficiency ($\eta_{extraction}$) as well as to achieve white color generation has been investigated. The use of optically transparent acrylate-based photopolymer with a refractive index of ∼1.5 as a 3D printed lens on blue LED has exhibited ∼9% enhancement in the output power at current injection of 4 mA as compared to blue LEDs without 3D printed lens. Finite-difference time-domain (FDTD) simulations investigating various geometries of the 3D printed lens also show that up to 1.61-times enhancement in $\eta_{extraction}$ can be obtained. By mixing the photopolymer with YAG:Ce phosphor powder, stable white color emission can be achieved with chromaticity coordinates around (0.27, 0.32) and correlated color temperature ∼8900 K at current injection of 10 mA.

8.1 Introduction

The issues associated with low $\eta_{extraction}$ for III-nitride LEDs are primarily caused by total internal reflection (TIR) at the GaN/air interface. Based on Snell′s Law, the critical angle (θ_c), which is the angle for the onset of TIR, for nitride-based LEDs is defined as

$$\theta_c = \arcsin \frac{n_{air}}{n_{GaN}} \tag{8.1}$$

where n_{air} and n_{GaN} are the refractive indexes of air and GaN respectively. By substituting $n_{GaN} = 2.5$ and $n_{air} = 1$ into Equation (8.1), the θ_c for GaN LED is calculated as $\sim$24°. This implies that photons generated in the active region of planar InGaN LED arrive at the GaN/air interface at an angle larger than 24° will be trapped inside the LED. For a conventional planar LED, the $\eta_{extraction}$ can then be approximated by the following equation:

$$\eta_{extraction} \approx \frac{1}{4n^2} \tag{8.2}$$

where n is the refractive index of the semiconductor. With $n_{GaN} = 2.5$, Equation (8.2) suggested that only $\sim$4% of light generated in the active region can be radiated out from the device [114]. This relatively low light output power is inadequate for realizing high-efficiency LEDs for solid-state lighting. Accordingly, various approaches such as surface roughening [15, 51], patterned sapphire substrate [16, 60], microstructure arrays [17, 115] and photonic crystals [64, 65, 18] have been attempted to enhance the $\eta_{extraction}$. Though these approaches have demonstrated substantial improvement in the $\eta_{extraction}$, they all involved elaborated fabrication steps that are not ideal for scalable production.

Thus, alternative approaches to realize white LEDs with a cost-effective and scalable process is highly demanded for solid-state lighting. Conventionally, blue-emitting LED is coated with yellow phosphor to achieve white light

generation [116, 117]. However, those phosphor-converted white LEDs require additional processing steps, such as the use of a mold to prepare the phosphor paste. On the other hand, phosphor-free approaches including multicolor-emitting quantum well structures [118, 119], multi-chip designs [120], as well as nanostructured designs [121, 122, 123, 124, 125, 126, 127, 128] have also been proposed. Nevertheless, these methods all require complex fabrication processes, which are challenging to be implemented into large scale production.

In light of the advancement of 3D printing technology, the integration of 3D printing process with InGaN-based LED is proposed in this work as a straightforward and highly-reproducible method to improve the $\eta_{extraction}$ as well as to achieve white color generation. Optical and electrical characterizations including refractive index measurement for 3D printed lens, angle-dependent electroluminescence (EL) and output power measurements for blue and white LEDs with 3D printed lens have been performed to examine the $\eta_{extraction}$ as well as to calculate the chromaticity coordinates. 3D FDTD simulations have also been carried out to investigate the effect of various lens designs on the $\eta_{extraction}$.

8.2 Characterization of 3D Printed Lens

Optically transparent acrylate-based curable photopolymer has been chosen as the lens material in this proof of concept study. The refractive index of the photopolymer is being characterized using Woollam VASE ellipsometer. A 1-mm thick square-shaped photopolymer with a side length of 25 mm is 3D printed on a bare silicon wafer using Formlabs Form 2 Stereolithography (SLA) 3D printer. To be more specific, CAD model of a 1 mm-thick square-shaped photopolymer is first designed using Solidworks and saved as an STL file. The STL file is then geometrically sliced into a series of 2D images that will be printed on top of the next by the 3D printer. For the printing

part, the build platform is first positioned in the tank of liquid photopolymer. For each layer to be printed, a galvanometer scans a 405 nm violet laser beam over the region of the liquid resin to be cured. The platform is then raised every time a layer is cured to make room for the next layer. For each new layer, uncured resin is spread and the laser scanning process is repeated until the whole geometry is printed. After the final layer is cured, the 3D printed lens is post-processed by rinsing in isopropyl alcohol to remove wet resin remaining on the surface of the wafer, followed by post-curing in curing oven for ∼30 minutes to improve its adhesion between the printed part and the silicon substrate.

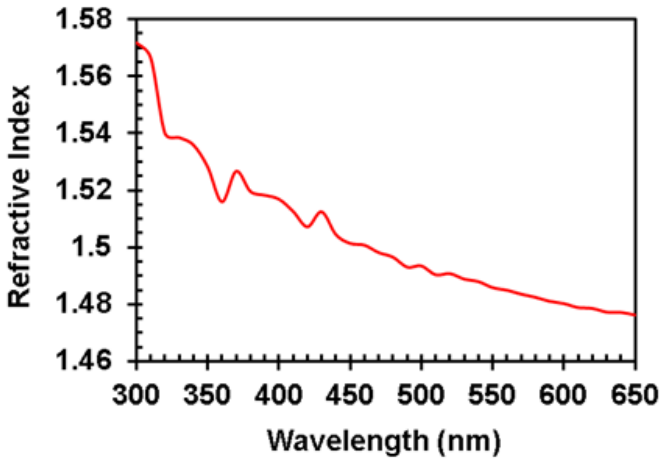

Figure 8.1: Refractive index of 1 mm-thick acrylate-based curable photopolymer as a function of wavelength.

The refractive index of the photopolymer as a function of wavelength is presented in Figure 8.1. As can be seen in Figure 8.1, the refractive index of the photopolymer at wavelength from 300 nm to 650 nm has been characterized as ∼1.48 to ∼1.57. As an example, by applying the refractive index of the photopolymer as 1.5 into Snell′s Law, the θ_c for InGaN/GaN LED emitting at 450 nm with the photopolymer on top is determined as ∼37°. This resulted in larger photon escape cone for the LED with photopolymer on top as compared to conventional planar LED without

the photopolymer ($\theta_{c,planarLED}$ ~24°). The presence of larger photon escape cone is desired as it enables more photons to be extracted out of the LED structure, which in turn can lead to higher $\eta_{extraction}$.

8.3 Blue LEDs with 3D Printed Lens

In order to verify the effectiveness of the photopolymer in enhancing $\eta_{extraction}$, a dome-shaped lens of diameter 500 μm has been 3D printed on a 500 × 500 μm^2 InGaN-based blue LED device, as illustrated in Figure 8.2. The LED structure consists of a 2.5 μm silicon-doped n-GaN layer on top of a sapphire substrate, followed by six periods of 2.5 nm/10 nm InGaN/GaN multiple quantum wells (MQW), and capped with a 200 nm magnesium-doped p-GaN layer. The doping concentration for the n- and p-doped GaN is 10^{18} cm^{-3} and 10^{17} cm^{-3} respectively. 20 nm Ti / 200 nm Au metal stack is evaporated as n-contact while 20 nm Ni / 200 nm Au metal stack is evaporated as metal stack for p-contact. A dome-shaped lens of diameter 500 μm is then 3D printed using Formlabs Form 2 3D printer, as described in the previous section.

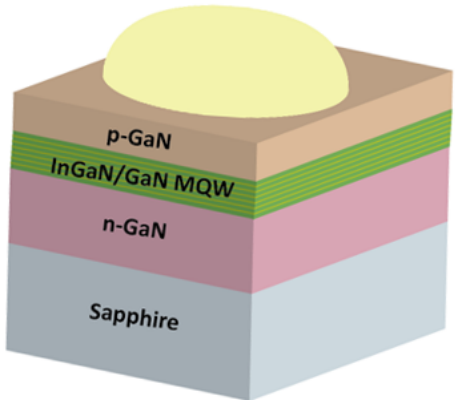

Figure 8.2: Schematic showing a 3D printed lens on an InGaN/GaN blue LED.

Figure 8.3(a) plots the output power of the blue LEDs with and without 3D printed lens as a function of current injection. The insets show the emission of blue LEDs

with and without 3D printed lens respectively at current injection of 4 mA. From the output power measurement results presented in Figure 8.3(a), it clearly indicates output power enhancement for the LED with a 3D printed lens as compared to LED without the lens. For example, up to ∼9% enhancement in the output power can be obtained at current injection of 4 mA. As evidenced by the angle-dependent EL measurement results presented in Figure 8.3(b), higher light intensity can be measured from all angles. In particular, significant output enhancement can be observed at angles between 0° and 30°. The enhancement in the measured light output power is attributed to the larger photon escape cone by the use of photopolymer with a refractive index of 1.5 as well as the curvature shape of the 3D printed lens.

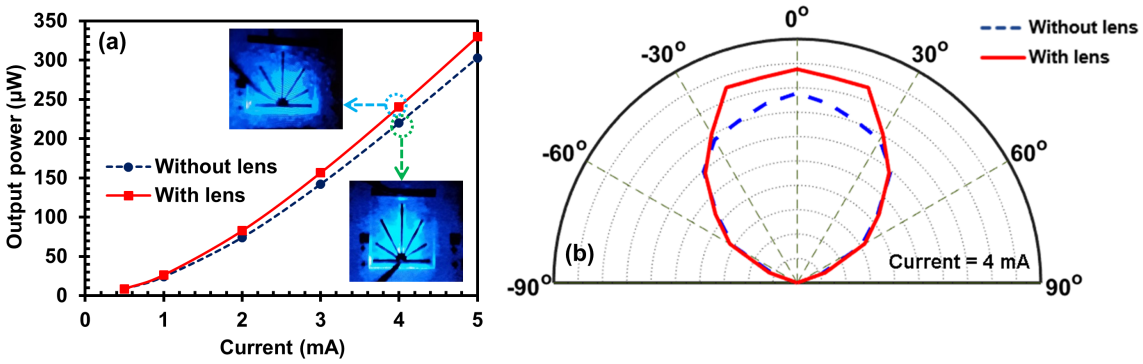

Figure 8.3: (a) Output power versus current injection for blue LEDs with and without the 3D printed lens. The photomicrograph insets show the emission of blue LEDs with (top inset) and without (bottom inset) 3D printed lens at current injection of 4 mA. (b) Angle-dependent EL measurements for blue LEDs with and without 3D printed lens at current injection of 4 mA.

As described in the previous section, the use of 3D printed lens with a refractive index of 1.5 on top of a planar structure blue LED can lead to a larger photon escape cope with θ_c ∼37° (as compared to $\theta_{c,planarLED}$ ∼24°). This enables more photons to enter the 3D printed lens that would have otherwise been trapped inside the LED due to total internal reflection. Attributed to the curvature surface of the 3D printed lens, the incident light inside the 3D printed lens would now have their own normal

for light refraction, as illustrated in Figure 8.4. As a result, all photons from the blue LED that has entered the 3D printed lens can be extracted out, which lead to the enhanced light output power observed in Figure 8.3(a).

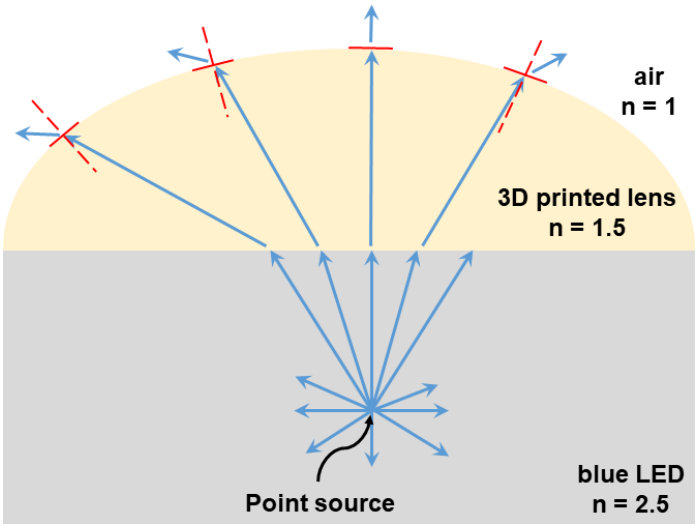

Figure 8.4: Schematic of a planar structure blue LED with a 3D printed lens showing the refraction of light in the 3D printed lens.

3D FDTD simulations [129] have also been performed to examine the effect of various lens designs on the $\eta_{extraction}$. The two lens designs investigated are depicted in Figure 8.5(a) for a dome-shaped lens design and Figure 8.6(a) for a dome-shaped lens on a cylinder base design. The height of the dome-shaped lens is labeled as h, and the height of the cylinder base is labeled as d. The layer structure of the simulated LEDs emitting at 450 nm, which consists of 200 nm sapphire substrate, 100 nm n-GaN layer, 50 nm InGaN/GaN MQW and 100 nm p-GaN layer are also depicted in Figures 8.5(a) and 8.6(a). The refractive indexes of the GaN, InGaN MQW, sapphire, and 3D printed lens are set as 2.5, 2.6, 1.8 and 1.5 respectively with absorption coefficient of 10 cm^{-1} for GaN and 2000 cm^{-1} for InGaN MQW [130, 71]. The simulation domain is set to 5×5 μm^2 with a non-uniform grid size of 10 nm in the bulk and 2.5 nm at the edge [71]. The perfectly matched layer boundary condition is applied to all the boundaries of the simulated structure. A single dipole source

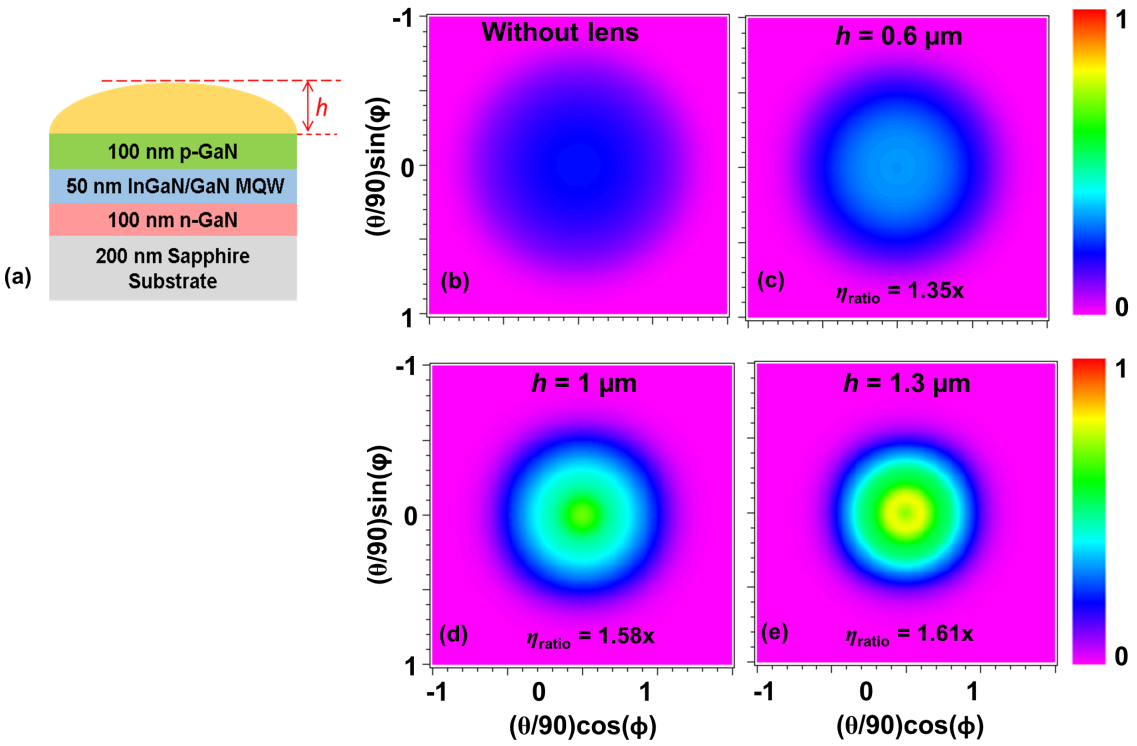

Figure 8.5: (a) Schematic side view of InGaN LED with dome-shaped lens; (b) far-field radiation pattern for conventional InGaN LED (b) without lens, with dome-shaped lens of (c) $h = 0.6$ μm, (d) $h = 1$ μm, and (e) $h = 1.3$ μm.

with emission wavelength 450 nm is placed at the center of the active region, and a power monitor is placed at 200 nm away from the top of the simulated structure to monitor the light output power radiated out of the simulated device. Only transverse electric (TE)-polarized light (major electric field travels in the in-plane direction) is considered in this study since emission from InGaN-based active region has been reported to be primarily TE-dominant [113]. The $\eta_{extraction}$ is calculated as the ratio of the light output power measured by the power monitor to the total power dissipated by the dipole source in the active region while the $\eta_{extraction}$ ratio (η_{ratio}) is calculated by normalizing the $\eta_{extraction}$ obtained from the LED with a 3D printed lens to the conventional LED without 3D printed lens.

The far-field radiation pattern for conventional LEDs without 3D printed lens are plotted in Figures 8.5(b) and 8.6(b) where typical Lambertian radiation pattern

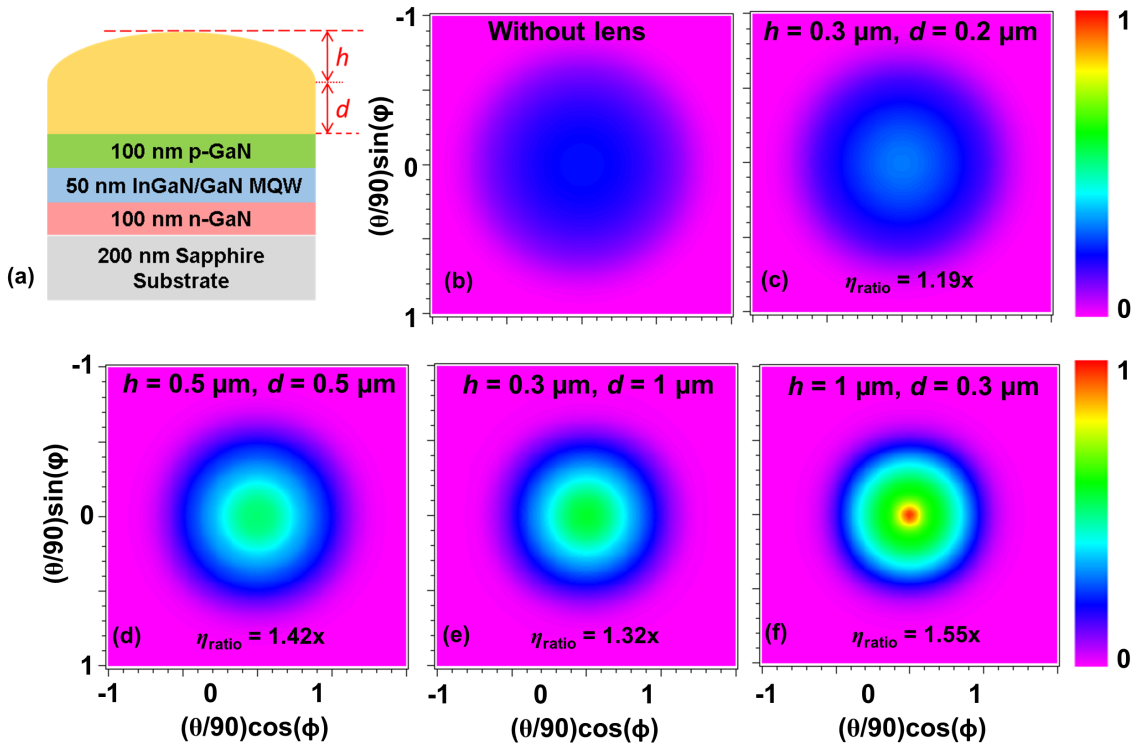

Figure 8.6: (a) Schematic side view of InGaN LED with dome-shaped lens on cylinder base; far-field radiation pattern for conventional InGaN LED (b) without lens, with dome-shaped lens on cylinder base of (c) $h = 0.3$ μm, $d = 0.2$ μm, (d) $h = 0.5$ μm, $d = 0.5$ μm, (e) $h = 0.3$ μm, $d = 1$ μm, and (f) $h = 1$ μm, $d = 0.3$ μm.

with angular (θ) dependent and symmetrically azimuthal (ϕ) distribution has been expected. By integrating a 3D printed lens with a refractive index of 1.5 on top of the InGaN LED, the same Lambertian radiation pattern can be observed for both lens designs, as depicted in Figures 8.5(c) – 8.5(e) and Figures 8.6(c) – 8.6(f). In particular, higher radiation intensity can be observed at the center region, which eventually contributes to larger $\eta_{extraction}$ than the conventional LEDs without 3D printed lens. From the η_{ratio} indicated in Figures 8.5(c) – 8.5(e) for LEDs with the dome-shaped lens of various h, the enhancement in the $\eta_{extraction}$ is observed to increase when the h is getting larger. Specifically, the η_{ratio} is calculated to increase from 1.35-times to 1.61-times when h changes from 0.6 μm [Figure 8.5(c)] to 1.3 μm [Figure 8.5(e)].

For the case of LEDs with a dome-shaped lens on a cylinder base, the same phenomena can also be observed where the $\eta_{extraction}$ increases when the total height of the lens ($h + d$) is increasing. For instance, the η_{ratio} is calculated to increase from 1.19-times to 1.55-times when the total height of the lens changes from 0.5 μm [Figure 8.6(c)] to 1.3 μm [Figure 8.6(f)]. However, when comparing the radiation plots and η_{ratio} of Figures 8.5(e), 8.6(e) and 8.6(f) where the total height of the lens is 1.3 μm, it is obvious that d parameter has less effect than h parameter on the $\eta_{extraction}$. This implies that the curvature shape of the lens is more critical than the total height of the lens in enhancing the $\eta_{extraction}$. To be more specific, the calculated η_{ratio} for LEDs with 1.3 μm total lens thickness increases from 1.32-times at $h = 0.3$ μm, $d = 1$ μm [Figure 8.6(e)] to 1.55-times at $h = 1$ μm, $d = 0.3$ μm [Figure 8.6(f)], and 1.61-times at $h = 1.3$ μm, $d = 0$ [Figure 8.5(e)]. Another comparison is the LEDs with a total lens thickness of 1 μm where the η_{ratio} with lens design of $h = 0.5$ μm, $d = 0.5$ μm [Figure 8.6(d)] is only 1.42-times while η_{ratio} for LEDs with lens design of $h = 0.5$ μm, $d = 0$ [Figure 8.5(d)] is determined to be 1.58-times.

Based on the results obtained from the FDTD analysis, two conditions related to the lens design have been exemplified: 1) the use of 3D printed lens with higher refractive index ($n_{lens} = 1.5$) than air medium ($n_{air} = 1$) is resulting in larger photon escape cone in the GaN/lens interface that can help to extract more photons out of the LED structure, and 2) the curvature shape of the 3D printed lens, which can help to enhance the light scattering effect, is more critical than the total lens thickness in light extraction. These two design considerations can be tuned easily by the use of 3D printing technology as the parameter h and d can be changed by modifying the CAD file while the simplicity in changing the photopolymer type in the 3D printer enables the possibility of experimenting with different lens materials of various refractive indexes. In addition, the use of the 3D printed lens as an encapsulation for LED devices can also achieve white color emission by mixing the

photopolymer with phosphor, which removes the need for extended fabrication procedure.

8.4 White LEDs with 3D Printed Lens

Based on the promising results obtained from blue LEDs with a 3D printed lens, the possibility of achieving high-efficiency white LEDs using 3D printed lens has been investigated. In pursuance of achieving white color emission, the mixture of photopolymer with yellow phosphor powder is 3D printed on blue LED devices. Commercial Ce-doped YAG phosphor powder with peak emission at 551 nm and an average particle size of 18 μm is used in this study. As it is impractical to prepare a large tank of photopolymer with phosphor powder mixture for the Formlabs Form 2 SLA 3D printer in this proof of concept study, System 30M 3D printer (Hyrel3D, USA) equipped with a standard SDS-5 extruder is used instead. The apparatus has a stepper motor with a gear reduction system to produce a low flow rate of the ink. The ink (a mixture of photopolymer and yellow phosphor powder in the ratio of 2:1 prepared using a mixer at 4000 rpm for 30 minutes) is loaded into a 5 cubic centimeter syringe and mounted on the SDS-5 extruder. A 34 gauge luer lock dispensing needle is used to print the desired pattern onto the blue LED devices. Parameters such as flow rate, standoff distance, and translational speed can be optimized based on the ink properties and lens design, which enable mass customization on a large scale. In addition, this printing process can also be easily transformed from the lab-scale process into large scale production through automation, for example, by defining how many times to repeat the printing process after the stepper motor moves for a certain distance.

Figure 8.7(a) shows that white color emission can be achieved from the blue LED by the use of the mixture of photopolymer and phosphor powder as 3D printed lens.

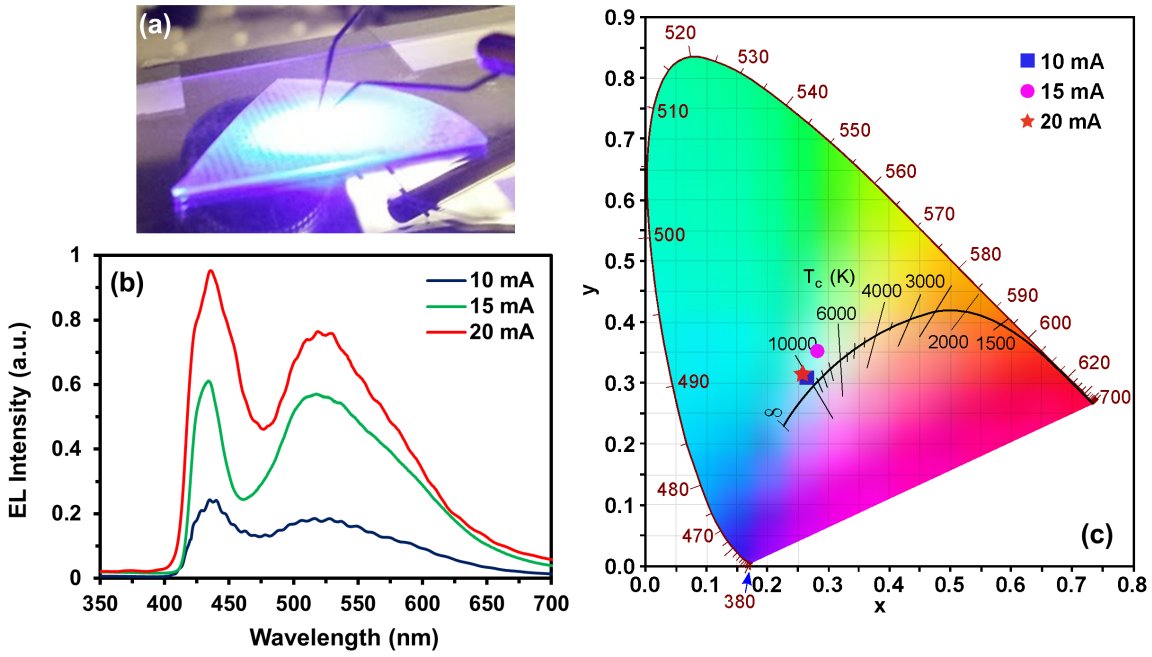

Figure 8.7: (a) White color emission from the proposed white LED with 3D printed lens; (b) EL intensities for white LEDs with 3D printed lens under various current injections; (c) Color coordinates of the light emission for white LEDs with 3D printed lens under various current injection on the CIE 1931 color space chromaticity diagram.

The EL intensities at various current injection presented in Figure 8.7(b) exhibit dual-wavelength emission peaks at ∼440 nm and ∼530 nm, which are critical for color mixing to achieve white color emission. To further demonstrate the white light emission from the proposed white LED with the 3D printed lens, the location of the light at various current injections are shown in the Commission Internationale de l'Eclairage (CIE) 1931 color space chromaticity diagram. As indicated in the CIE diagram, the coordinates are essentially in the white region as the current changes from 10 mA to 20 mA. In particular, the CIE coordinates are primarily located around (0.27, 0.32) with correlated color temperature (CCT) ∼8900 K at 10 mA, and approximately (0.26, 0.32) with CCT ∼9200 K at 20 mA, which is comparable to those nanostructured white LEDs, for example, disk-in-wire LEDs with CIE coordinate of (0.29, 0.37) at 50 A/cm^2 [127].

8.5 Conclusion

In summary, the integration of 3D printed lens with InGaN-based LED for enhanced $\eta_{extraction}$ and white color emission has been proposed and investigated in this study. As a proof of concept study, a dome-shaped lens of diameter 500 μm with a refractive index of 1.5 has been 3D printed on a blue LED device, where $\sim$9% enhancement in the light output power at current injection of 4 mA has been observed. FDTD analysis of various lens designs that show up to 1.61-times enhancement in $\eta_{extraction}$ has confirmed the feasibility of using the 3D printed lens to improve the $\eta_{extraction}$. In addition, white color emission has also been demonstrated from a blue LED with a 3D printed lens by mixing the photopolymer with yellow phosphors. Specifically, chromaticity coordinate of (0.27, 0.32) and CCT $\sim$8900 K has been reported at current injection of 10 mA. It is anticipated that the proposal of the integration of 3D printed lens with nitride-based LEDs presented in this study could open the door to cost-effective and scalable processes in realizing next-generation high-efficiency and high-brightness III-nitride LEDs.

Chapter 9

White LEDs with Ternary InGaN Substrate

In this chapter, the use of ternary InGaN substrate for high-efficiency monolithic tunable white light-emitting diodes (LEDs) has been investigated. Nanostructure engineering has been conducted in the multiple quantum wells (MQW) active region for LEDs on ternary InGaN substrate to achieve white color illumination. Simulation studies showed that the proposed and optimized white LED device structures exhibited ~2 times larger external quantum efficiency (η_{EQE}) and higher light output power as compared to conventional InGaN/GaN LEDs on GaN substrate. The chromaticity coordinates and correlated color temperature (CCT) of the proposed white LEDs on ternary substrate also demonstrated comparable results with those nanostructured white LEDs.

9.1 Introduction

Solid-state lighting based on white color LEDs is considered as the next-generation illumination system due to the high efficiency and reliable device performance. Conventionally, GaN-based blue-emitting LED is coated with yellow phosphor to

convert part of the blue emission to longer wavelength (λ) for white light generation [131, 120, 132, 133]. However, these phosphor-converted (PC) white LEDs exhibit large Stokes loss ($\sim$10 to $\sim$30%) due to the wavelength down-conversion [133]. Additionally, those PC-LEDs suffer from stability issues such as phosphor-aging, packaging cost issues, and dependency on the efficiency of GaN-based LEDs [133]. Meanwhile, "multichip" approach [120] has also been proposed for white-color generation by combining red, green and blue (RGB) monochromatic LED chips, which demonstrates several significant advantages over PC-LEDs. However, this approach suffers from significantly increased cost from additional processing steps for chips integration and the need for driver circuitry.

Thus, the pursuit of high-efficiency, cost-effective, and monolithic white LEDs has attracted tremendous attention [126, 127, 134, 124, 135]. Previous works have reported the possibility of fabricating phosphor-free monolithic white LEDs by stacking multi-color-emitting InGaN/GaN quantum wells (QWs) on GaN substrate [136, 137, 138, 119, 134]. However, it is very challenging to incorporate high In-content into InGaN/GaN QWs on GaN substrate, which is critical for green and yellow emission wavelengths, due to charge separation issue from large lattice-mismatch strain [130, 139]. On the other hand, nanostructure engineering approaches such as the use of quantum dots [125, 124], nanowires [140, 126, 127], pyramids [135, 128, 123] and patterned substrates [141, 142] have also been pursued previously to achieve white LEDs. Nevertheless, these methods all require complex fabrication processes which are challenging to be implemented into large scale production. Therefore, alternative cost-effective and high-efficiency solutions are in great demand for white LEDs.

Recent studies have pointed out that the use of ternary InGaN substrate for InGaN/InGaN QW LEDs could lead to promising light output covering the entire visible spectrum [143, 144]. Up to $\sim$3 times enhancement in spontaneous emission

rate for $\lambda \sim 450 - 645$ nm as compared to conventional InGaN/GaN QWs on GaN substrate has been reported. Additionally, experimental works reporting successful growth of high In-content ternary InGaN substrate [145, 146, 147, 148, 149] would enable the growth of InGaN LEDs on ternary substrates. Specifically, recent works by Hoffbauer and coworkers have demonstrated the growth of high quality InGaN films on sapphire, with In-content up to 40% and film thickness up to 1 μm [148, 149], using molecular beam epitaxy. Thus, it is anticipated that those ternary substrates would be suitable for InGaN-based green and yellow emitters, which would be of great interest for feasible monolithic white LEDs.

9.2 Numerical Simulation of White LEDs with Ternary InGaN Substrate

Advanced Physical Models of Semiconductor Devices (APSYS), a 2D/3D software modeling package developed by Crosslight Software Inc., has been employed to analyze the optical and electrical characteristics of the white LEDs on ternary InGaN substrate. APSYS models the optical and thermal properties of semiconductor devices based on finite element analysis by solving Poisson's equation and current continuity equations. The band structures and radiative recombination rates are solved self-consistently with $k{\cdot}p$ the quantum mechanical solver by taking into consideration carrier transport effect, valence band mixing, strain effect, spontaneous and piezoelectric polarizations, and carrier screening effect. All band parameters used in the simulation were taken from Refs. [150, 151]. The band offset ratio (ΔE_c:ΔE_v) for all layers was set as 0.7:0.3, and the surface charge density was set as 50% of the theoretical values [152]. The operating temperature was assumed to be 300 K.

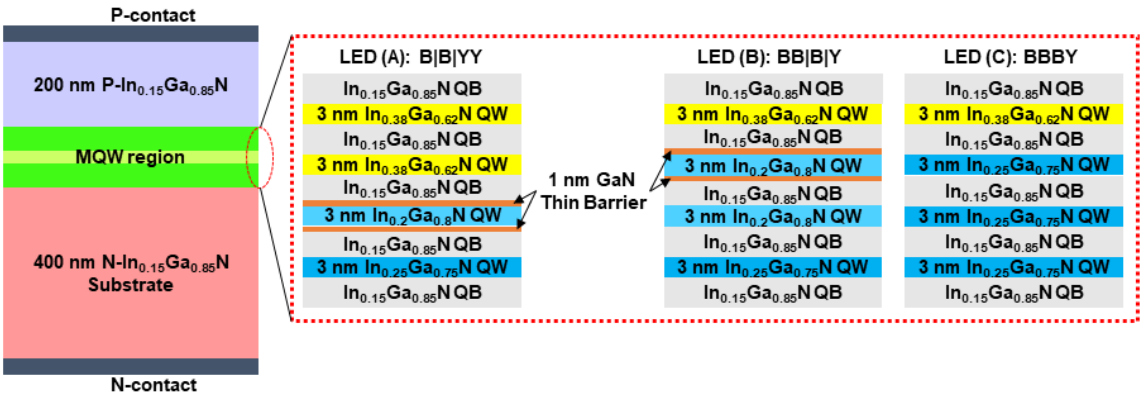

Figure 9.1: Schematics of monolithic white LEDs consist of 3 nm InGaN MQWs with 6 nm $In_{0.15}Ga_{0.85}N$ QBs on ternary $In_{0.15}Ga_{0.85}N$ substrate. 1 nm thin GaN barrier is inserted to surround the blue QW located closer to p-region for LED (A) and LED (B). LED (C) without thin barriers is used as a reference device.

Two monolithic white LED structures with vertical injection configuration shown in Figure 9.1 [LED (A) and LED (B)] have been proposed and studied. The LED device without any nanostructure engineering [LED (C)] is used as a reference. LED (A) is composed of two blue-emitting QWs and two yellow-emitting QWs while LED (B) and LED (C) are composed of three blue-emitting QWs and one yellow-emitting QW. The 0.4 μm thick n-$In_{0.15}Ga_{0.85}N$ layer (n-doping = 5×10^{18} cm^{-3}) is used as the substrate of the device, followed by four periods of 3 nm $In_xGa_{1-x}N$ QWs (x = 0.2 or 0.25 for blue emission and x = 0.38 for yellow emission) with 6 nm $In_{0.15}Ga_{0.85}N$ quantum barriers (QBs), and a 200 nm p-$In_{0.15}Ga_{0.85}N$ layer (p-doping = 1.2×10^{18} cm^{-3}). Note that the strain in InGaN/InGaN QW on ternary InGaN substrate can be reduced by up to ~75% as compared to conventional InGaN/GaN QW on GaN substrate, as pointed out by previous work [144]. The significantly decreased strain resulted in a substantial reduction of piezoelectric polarization field and internal electrostatic field in the QWs, and consequently led to the suppression of the charge separation effect. Thus, the ternary $In_{0.15}Ga_{0.85}N$ substrate has been employed in this study for all the proposed LEDs. The background doping in the

active region is assumed as 5×10^{16} cm^{-3}. For both LED (A) and LED (B), a 1 nm thin GaN barrier has been inserted to surround the blue-emitting QW (in this case, the 6 nm $In_{0.15}Ga_{0.85}N$ QB is replaced with 5 nm $In_{0.15}Ga_{0.85}N$ QB and 1 nm GaN thin barrier) located closer to the p-InGaN layer for improved carrier confinement in the blue-emitting QWs.

9.2.1 Band Structures and Carriers Distributions

The characteristics of the three InGaN/InGaN LEDs with ternary InGaN substrate at current density (J) of 100 A/cm^2 are analyzed and compared. Figure 9.2(a) plots the conduction bands and electron concentrations, and Figure 9.2(b) plots the valence bands and hole concentrations for all investigated devices. The corresponding bandgaps of GaN, $In_{0.15}Ga_{0.85}N$, $In_{0.2}Ga_{0.8}N$, $In_{0.25}Ga_{0.75}N$ and $In_{0.38}Ga_{0.62}N$ are calculated as 3.437 eV, 2.839 eV, 2.654 eV, 2.475 eV and 2.044 eV respectively. As can be observed from Figure 9.2, majority of the carriers are populating the yellow QW for LED (C) with peak electron and hole concentrations of 82×10^{18} cm^{-3} and 114×10^{18} cm^{-3} respectively while negligible amount of carriers are populating the blue QWs. Since the blue QW has smaller effective barrier height (h_c for conduction band and h_v for valence band) as compared to the yellow QW, the latter forms a strong local minimum in the MQWs active region, which is localizing carriers strongly and leading to poor carrier concentrations in the blue QWs. The insertion of the GaN thin barriers [the case of LED (A) and LED (B)] solves this issue by increasing h_c of electrons from 259 meV in LED (C) to 490 meV in both LED (A) and LED (B), and h_v of holes from 223 meV in LED (C) to 371 meV in both LED (A) and LED (B). As a result, the carrier population in the blue-emitting QWs has been enhanced significantly, as shown in Figure 9.2.

The peak electron and hole concentrations in the blue-emitting QW is 40×10^{18} cm^{-3} and 48×10^{18} cm^{-3} respectively for LED (A) and 32×10^{18} cm^{-3} and $41 \times$

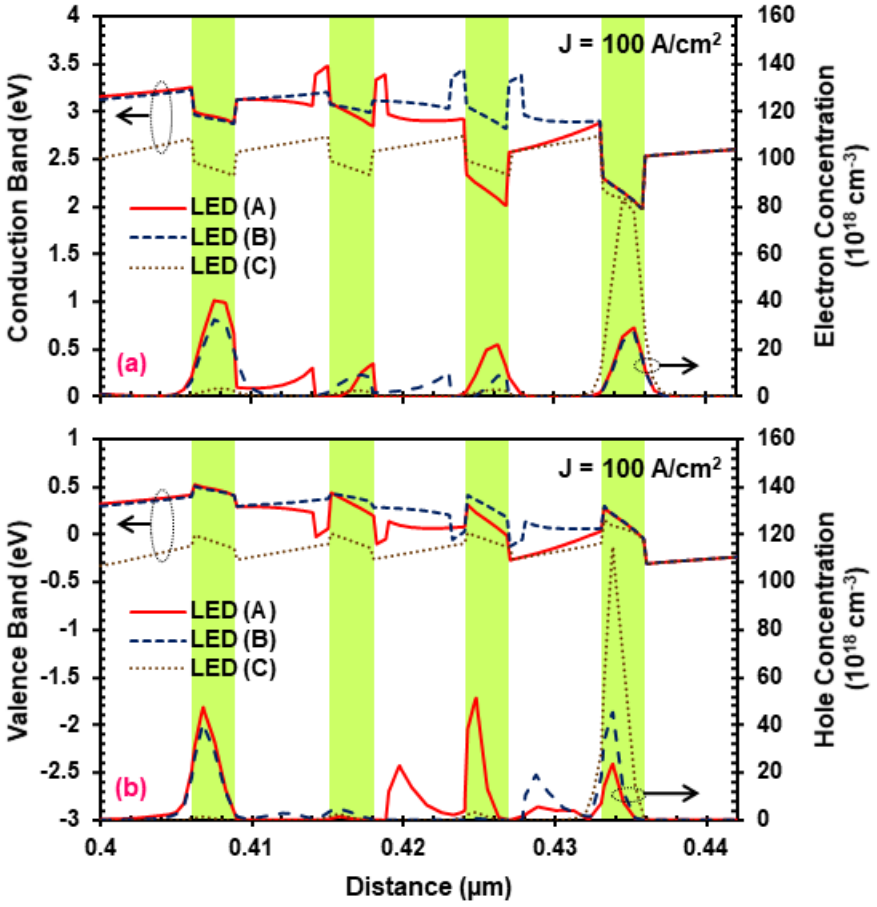

Figure 9.2: Simulated (a) conduction band structures and electron concentrations and (b) valence band structures and hole concentrations of InGaN/InGaN MQWs white LEDs on ternary InGaN substrate at J = 100 A/cm^2.

10^{18} cm^{-3} respectively for LED (B), and the peak electron and hole concentrations in the yellow-emitting QW is 30 $\times$ 10^{18} cm^{-3} and 54 $\times$ 10^{18} cm^{-3} respectively for LED (A) and 27 $\times$ 10^{18} cm^{-3} and 45 $\times$ 10^{18} cm^{-3} respectively for LED (B). This balanced carrier concentration in the MQWs active region is expected to lead to balanced light output in both blue and yellow spectral regimes, which would enable proper color-mixing to achieve white illumination.

9.2.2 Spontaneous Emission Spectra

To demonstrate the optical properties of the proposed white LEDs, Figure 9.3 plots the simulated spontaneous emission spectra of LEDs (A), (B) and (C) at J = 100 A/cm^2. The insertion of the GaN thin barrier effectively leads to dual-wavelength emissions in blue and yellow. Specifically, both LEDs (A) and (B) show the blue peak spontaneous emission wavelength (λ_{peak}) $\sim$ 480 nm due to the enhanced carrier populations in the blue QWs. The yellow peak for both LEDs is obtained with $\lambda_{peak} \sim$ 580 nm. Note that as a comparison, LED (C) shows a single green emission peak with $\lambda_{peak} \sim$ 560 nm and the full-width half maximum (FWHM) $\sim$62 nm, which can be attributed from the recombination of excited states since a considerably large amount of carriers are collected by the yellow QW. The spontaneous emission spectrum from the LED (C) also proves that it is very important to have the GaN thin barrier insertion in order to achieve white color illumination. Furthermore, the design of the MQWs active region from the LED (A) and LED (B) also shows the flexibility in terms of combining the blue and the yellow QWs, which would be ideal for large scale device manufacturing purpose.

9.2.3 Light Output Powers and External Quantum Efficiencies

The simulated light output power, current-voltage (IV) characteristic and relative η_{EQE} of the investigated monolithic white LEDs as a function of J are shown in Figure 9.4. Here, the extraction efficiency, monomolecular coefficient A, and Auger coefficient C are employed as 70%, 10^6 s^{-1} and 10^{34} cm^{6}s^{-1}, respectively [152]. In general, all three LEDs on ternary InGaN substrate exhibit promising light output power and η_{EQE} due to significantly reduced internal electrostatic field. The light output powers of $\sim$134 mW, $\sim$170 mW and $\sim$139 mW has been obtained for LED

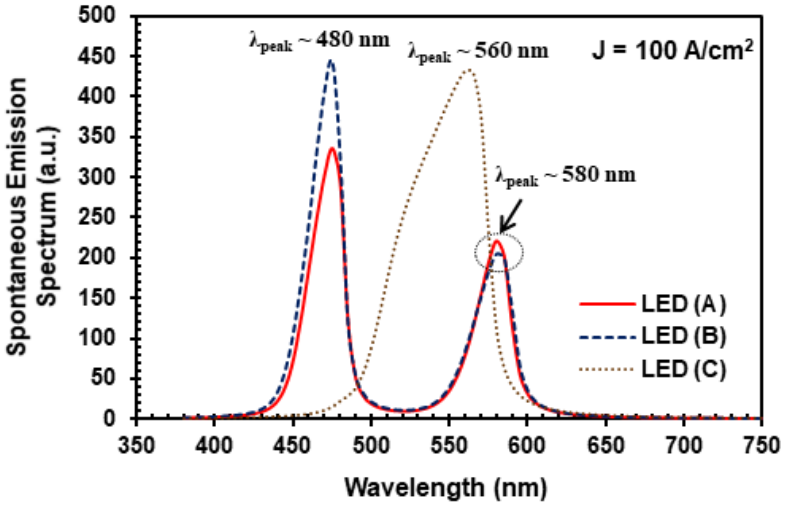

Figure 9.3: Simulated spontaneous emission spectra of InGaN/InGaN MQWs white LEDs on ternary InGaN substrate at J = 100 A/cm^2.

(A), LED (B) and LED (C) respectively at J = 250 A/cm^2, as shown in Figure 9.4(a). Note that the increased turn-on voltage (∼2.7 V) for both LEDs (A) and (B) are due to increased series resistance as compared to LED (C) (∼2.1 V), which is attributed from the larger barrier height induced by the insertion of the GaN thin barriers. From the relative η_{EQE} plot in Figure 9.4(b), it shows that both LEDs (A) and (B) on ternary substrate have the peak η_{EQE} (∼50%) with J ∼ 10 – 15 A/cm^2, which is significantly higher than that of InGaN/GaN monolithic white LEDs on conventional GaN substrate (η_{EQE} ∼ 20%) [137]. Despite the fact that LED (C) shows a higher η_{EQE} peak (∼68%) at J ∼ 25 A/cm^2, it has a much severe droop towards higher current densities, which is attributed from poorer carrier confinement due to the absence of the GaN thin barrier design. More importantly, only green color illumination can be obtained from LED (C) while white color illumination can be achieved by LEDs (A) and (B) with comparable output power and η_{EQE}.

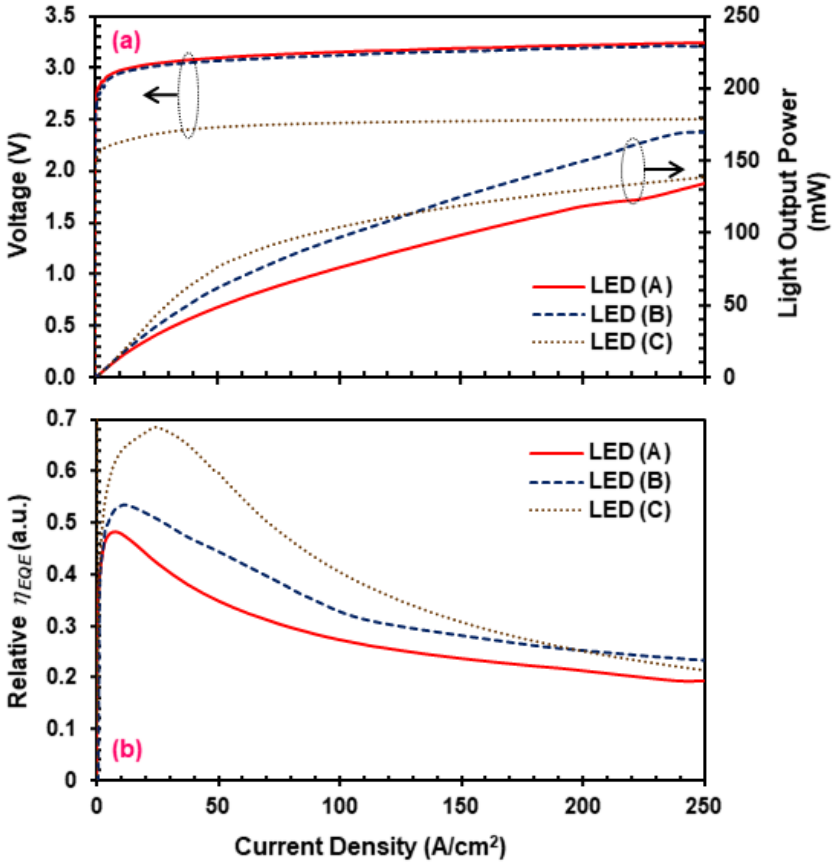

Figure 9.4: Simulated (a) light output powers and IV characteristics, and (b) relative η_{EQE} for InGaN/InGaN MQWs white LEDs on ternary InGaN substrate as a function of current density at room temperature.

9.2.4 Chromaticity Coordinates and Color Temperatures

Figure 9.5 shows the locations of the light emission for the investigated monolithic white LEDs on ternary substrates on the Commission Internationale de l'Eclairage (CIE) 1931 color space chromaticity diagram at various injection current levels. As indicated on the CIE diagram, the coordinates for LED (A) and LED (B) are essentially in the white region at various current injection levels while the coordinates for LED (C) are located in the green region. This again implies that the insertion of thin GaN barriers surrounding the blue QW adjacent to the yellow QW is essential for white color generation. The CIE coordinates are relatively constant,

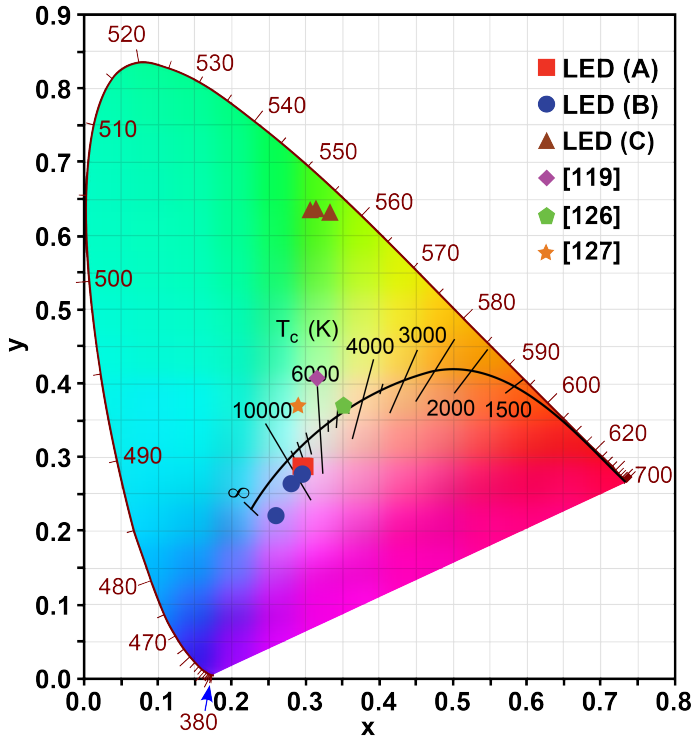

Figure 9.5: Color coordinates of the light emission for the investigated monolithic InGaN/InGaN MQW white LEDs on the CIE 1931 color space chromaticity diagram from 50 A/cm^2 to 150 A/cm^2. The CIE coordinates for InGaN/GaN white LED on GaN substrate [119] and nanowires white LEDs [126], [127] at 50 A/cm^2 are also shown in the figure.

approximately (0.30, 0.28), for LED (A) with current density up to 150 A/cm^2 whereas for LED (B), it moves from (0.30, 0.28) to (0.26, 0.22) as current increases from 50 A/cm^2 to 150 A/cm^2. Both LED (A) and LED (B) exhibit minor blue-shift with increased injection current due to quantum confined Stark effect.

For the investigated monolithic white LED structures, the corresponding CCTs at 50 A/cm^2 are obtained as ∼8200 K for LED (A) and ∼8800 K for LED (B), which are appropriate for general illumination purpose [131, 133]. The CCT values from LEDs (A) and (B) are also comparable with those of nanostructure white LEDs (∼4500 – 6500 K) [126, 127]. For comparison purpose, Figure 9.5 also summarizes the CIE coordinates for InGaN/GaN-based white LEDs on GaN substrates [(0.32, 0.41) at 50 A/cm^2] [119] and nanostructure white LEDs [(0.35, 0.37) and (0.29, 0.37)

respectively for dot-in-wire LEDs [126] and disk-in-wire LEDs [127] at 50 A/cm^2]. These results suggest that the proposed monolithic white InGaN/InGaN MQW LED structures can achieve stable white color illumination and promising efficiency while only require standard device fabrication processes.

9.3 Conclusion

In summary, high-efficiency phosphor-free monolithic white LEDs with InGaN/InGaN QWs on ternary InGaN substrate are proposed and analyzed. Simulation studies show that by integrating blue- and yellow-emitting InGaN/InGaN MQWs with an engineered structures on ternary InGaN substrate, large output power (∼170 mW) and high η_{EQE} (∼50%) can be achieved for stable white illumination at various current injections at room temperature. The results also demonstrate the importance of nanostructure engineering for InGaN/InGaN MQWs LEDs on ternary InGaN substrate for white light emission. The chromaticity coordinates around (0.30, 0.28) and CCT ∼8200 K can be obtained at J = 50 A/cm^2 for the tunable white LED structures with engineered active region in this study. Thus, it is expected that the monolithic InGaN/InGaN MQW white LED devices based on InGaN ternary substrate would serve as a promising candidate for high-efficiency and cost-effective solid-state lighting applications. Further experimental studies to investigate the optimized structure as well as the optimized growth are required for enabling the advantages presented in this study for InGaN/InGaN MQWs white LEDs on ternary InGaN substrate.

Chapter 10

Summary and Future Work

This dissertation describes a body of work investigating light extraction efficiency ($\eta_{extraction}$) for nanostructured III-nitride light-emitting diodes (LEDs). In particular, comprehensive studies on the polarization-dependent $\eta_{extraction}$ for AlGaN-based flip-chip UV LEDs with microdome-shaped patterned sapphire substrates (PSS) and AlGaN-based nanowire UV LEDs have been performed. Plasmonic nanowire green LED structure has also been proposed and investigated for enhancing the LED performance via surface plasmon polaritons (SPPs). Nanosphere lithography and KOH-based wet etching process have been developed for the top-down fabrication of III-nitride nanowire LEDs. In order to achieve white light emission, integration of three-dimension (3D) printing technology with LED fabrication as well as novel LED structures employing ternary InGaN substrate have also been discussed.

10.1 UV LEDs with Patterned Sapphire Substrate

Patterned sapphire substrate (PSS) has been widely used for III-nitride emitters in the visible region while there are still very limited works exploring the light extraction mechanism for III-nitride ultraviolet (UV) LEDs. My work has investigated the

transverse-electric (TE)- and transverse-magnetic (TM)-polarized $\eta_{extraction}$ for 230 nm and 280 nm flip-chip UV LEDs with microdome-shaped array patterning on the sapphire substrate. In particular, three types of PSS have been analyzed: bottom-side PSS, top-side PSS, and double-sided PSS. The results show that microdome-shaped PSS is particularly efficient in enhancing TM-polarized $\eta_{extraction}$ where up to ∼4.5-times and ∼2.2-times can be obtained for 230 nm and 280 nm flip-chip UV LEDs with bottom-side PSS respectively, and ∼6.3-times and ∼1.8-times for 230 nm and 280 nm flip-chip UV LEDs with top-side PSS respectively. The significant improvement obtained in the TM-polarized $\eta_{extraction}$ is attributed to the enhanced scattering effect introduced by the microdome-shaped array that enables the TM-polarized photons to escape from the LED structure. As a result, the use of double-sided PSS could result in even higher TM-polarized $\eta_{extraction}$ where up to ∼11.2-times and ∼2.6-times improvement can be achieved for 230 nm and 280 nm flip-chip UV LEDs respectively. Accordingly, higher η_{EQE} from UV LEDs employing PSS is expected as a result of dominant TM-polarized spontaneous emission and larger TM-polarized $\eta_{extraction}$. On the contrary, the use of the microdome-shaped PSS does not lead to enhanced TE-polarized $\eta_{extraction}$ for both the 230 nm and 280 nm flip-chip UV LEDs. The PSS is actually acting as a reflector that reflect majority of the TE-polarized light back into the structure. Consequently, lower TE-polarized $\eta_{extraction}$ for flip-chip UV LEDs with microdome-shaped PSS as compared to flip-chip UV LEDs with flat sapphire substrate has resulted.

The analysis presented in this study is intended to shed light on the design of flip-chip UV LEDs with nanostructure PSS for both mid- and deep-UV regimes to achieve high-efficiency AlGaN-based UV LEDs. Further analysis and comparison on various types of nanostructure patterning such as triangle, trapezoid and nano-hole arrays can also be performed to provide a more comprehensive insight into the use of nanostructure PSS for UV LEDs. In addition, the experimental realization of the

proposed UV LEDs with nanostructure PSS, including etching procedure to create nanostructure PSS followed by fabrication into LED devices can also be carried out in the future.

10.2 Nanowire UV LEDs

Nanowire LED structure is beneficial for extracting TM-polarized output attributed to its large surface-to-volume ratios, which is particularly important for high Al-composition AlGaN quantum well (QW) emission that is primarily TM-dominant. My work has been attempted to develop nanosphere lithography method to form III-nitride nanowires via top-down etching, followed by wet etching in AZ 400K solution to remove nanowires sidewall surface damage arisen from the plasma etch. The current reactive ion etching (RIE) recipe reported in this dissertation has not been optimized for fast etch rate and forming nanowires without taper base. Further optimization of the etch recipe by altering the gases flow rates, chamber pressure and RF power would be necessary in order to resolve these issues. On the other hand, results on current wet etching study show that AZ 400K solution with a concentration of 40%, at temperature of 45°C is adequate to achieve smooth nanowires with crystallographic base after etching for 30 minutes. Future study investigating the effects of various RIE conditions (which will result in various profiles on the nanowire sidewalls) on the AZ 400K wet etching may be necessary.

In addition, theoretical analysis of the polarization-dependent $\eta_{extraction}$ of 230 nm AlGaN-based nanowire LEDs has also been investigated using 3D FDTD method. Results show that up to ∼48% TM-polarized $\eta_{extraction}$ and ∼41% TE-polarized $\eta_{extraction}$ can be obtained for 230 nm UV LEDs with nanowire structure as compared to ∼0.2% TM-polarized $\eta_{extraction}$ and ∼2% TE-polarized

$\eta_{extraction}$ from the conventional planar structure. Smaller nanowire D (< 60 nm) enables more TM-polarized photons to leak out through the nanowire sidewall that results in higher $\eta_{extraction}$ while increases the nanowire H beyond 800 nm has less impact on the $\eta_{extraction}$. Additionally, investigation on various passivation layers materials and thicknesses also show that thick SiO_2 or AlN (> 75 nm) passivation layer can result in enhanced $\eta_{extraction}$ as compared to SiN_x and thinner SiO_2 or AlN (< 75 nm). Future work to address the impact of various nanowire design within an array of nanowires such as uniformity in nanowire diameter, height, spacing and peak emission wavelength as well as QW position is desired in order to provide more comprehensive modeling of the nanowire LED performance.

10.3 Plasmonic Nanowire LEDs

The use of surface plasmon polaritons (SPPs) has been reported previously as a mean to improve the η_{IQE} and $\eta_{extraction}$ of III-nitride plasmonic LEDs with planar structure. My work has proposed the use of nanowire structure for III-nitride plasmonic LEDs as the large sidewall surface area of the nanowire enables the exposure of the active region to interact with the SPPs, and eliminate the requirement of a thin p-type layer. My work has reported a preliminary study on III-nitride plasmonic nanowire green LEDs structure coated with 5 nm of Al_2O_3 as a dielectric layer and various Ag cladding layer thicknesses using 3D FDTD method. The results show that a Purcell factor of $\sim$80 can be obtained for the investigated plasmonic nanowire LEDs with $\eta_{extraction}$ $\sim$65% when the Ag thickness > 60 nm. Thinner Ag suffers from lower $\eta_{extraction}$ due to the lower reflectance from the thin metal film despite higher Purcell factor can be achieved.

Both the $\eta_{extraction}$ and Purcell factor are inferred to be uncorrelated with the thickness of the Ag cladding layer > 60 nm, which is desired due to the complication

in controlling the metal thickness through evaporation. Future analysis on smaller nanowire diameters, various dielectric layer materials such as SiO_2 and TiO_2, as well as various designs of the nanowire, for instance, torchlight-shaped nanowires, are essential to provide a comprehensive analysis on the use of nanowire structure as plasmonic LEDs to enhance the LED performance. It is important to note that high Purcell factor does not indicate enhancement in η_{IQE} as the latter is also depending on the probability of photons extraction from the SPs energy. Therefore, theoretical analysis can serve as a guidance on the design of plasmonic nanowire LEDs in order to obtain large $\eta_{extraction}$ and high Purcell factor while future experimental study is necessary to examine the decay rate of the SPPs.

10.4 3D Printed Lens on InGaN LEDs for White Color Emission

In light of the advancement of 3D printing technology, the integration of 3D printing process with InGaN-based LED is proposed in this dissertation as a straightforward and highly-reproducible method to improve the $\eta_{extraction}$ as well as to achieve white color generation. As a proof of concept study, optically transparent acrylate-based photopolymer with a refractive index of ∼1.5 has 3D printed in as dome-shaped lens on blue LED devices. Power measurements on the blue LEDs with 3D printed lens show that up to ∼9% enhancement in the light output power at current injection of 4 mA can be observed as compared to blue LEDs without the 3D printed lens. FDTD analysis of various lens designs that show up to 1.61-times enhancement in $\eta_{extraction}$ has confirmed the feasibility of using the 3D printed lens to improve the $\eta_{extraction}$. In addition, white color emission has also been demonstrated from a blue LED with a 3D printed lens by mixing the photopolymer with YAG:Ce phosphor powder. Specifically, chromaticity coordinate of (0.27, 0.32) and CCT ∼8900 K has

been reported at current injection of 10 mA. It is anticipated that the proposal of the integration of 3D printed lens with nitride-based LEDs presented in this study could open the door to cost-effective and scalable processes in realizing next-generation high-efficiency and high-brightness III-nitride LEDs.

10.5 Monolithic White LEDs with Ternary InGaN Substrate

Previous studies have pointed out that the use of ternary InGaN substrate for InGaN/InGaN QW LEDs could lead to promising light output covering the entire visible spectrum attributed to smaller lattice mismatch as compared to conventional InGaN/GaN QWs on GaN substrate. In my work, the use of ternary InGaN substrate for high-efficiency monolithic tunable white LEDs has been investigated. Nanostructure engineering has been conducted in the multiple QW (MQW) active region for LEDs on ternary InGaN substrate to achieve white color illumination. Simulation studies show that by integrating blue- and yellow-emitting InGaN/InGaN MQWs with engineered structures on ternary InGaN substrate, large output power (∼170 mW) and high external quantum efficiency (∼50%) can be achieved for stable white illumination at various current injections at room temperature. The results also demonstrate the importance of nanostructure engineering for InGaN/InGaN MQWs LEDs on ternary InGaN substrate for white light emission. The chromaticity coordinates around (0.30, 0.28) and CCT ∼8200 K can be obtained at current injection of 50 A/cm^2 for the tunable white LED structures with an engineered active region in this study. Thus, it is expected that the monolithic InGaN/InGaN MQW white LED devices based on InGaN ternary substrate would serve as a promising candidate for high-efficiency and cost-effective solid-state lighting applications. Further experimental studies to investigate the

optimized structure as well as the optimized growth are required for enabling the advantages presented in this study for InGaN/InGaN MQWs white LEDs on ternary InGaN substrate.

Appendix A

Finite-Difference Time-Domain Method

In this chapter, the algorithm of Finite-Difference Time-Domain (FDTD) method is discussed, followed by the calculation of light extraction efficiency ($\eta_{extraction}$), far-field radiation pattern and Purcell factor (F_P). The simulation settings for each of this calculation are also discussed here.

A.1 Finite-Difference Time-Domain Algorithm

FDTD calculation is a commonly used technique in studying the propagation of photons in micro and nano-scale structures in response to a given electromagnetic excitation by solving Maxwell's equations with specific boundary conditions based on Yee cell. Maxwell's equations describe a situation in which the temporal change in the electric field field is dependent upon the spatial variation of the magnetic field, and vice versa. The Maxwell's curl equations are expressed as equation (A.1) as followed:

$$\frac{\partial \overrightarrow{\boldsymbol{E}}}{\partial t} = \frac{1}{\varepsilon} \bigtriangledown \times \overrightarrow{\boldsymbol{H}} \tag{A.1a}$$

$$\frac{\partial \overrightarrow{\boldsymbol{H}}}{\partial t} = \frac{1}{\mu} \bigtriangledown \times \overrightarrow{\boldsymbol{E}} \tag{A.1b}$$

where $\overrightarrow{\boldsymbol{E}}$ is the electric field, $\overrightarrow{\boldsymbol{H}}$ is the magnetic field, ε is the medium permittivity and μ is the permeability. In three dimensions, the Maxwell's curl equations can be expressed in Cartesian coordinates as six scalar equations:

$$\frac{\partial \boldsymbol{E}_x}{\partial t} = \frac{1}{\varepsilon}\left(\frac{\partial \boldsymbol{H}_z}{\partial y} - \frac{\partial \boldsymbol{H}_y}{\partial z}\right) \tag{A.2a}$$

$$\frac{\partial \boldsymbol{E}_y}{\partial t} = \frac{1}{\varepsilon}\left(\frac{\partial \boldsymbol{H}_x}{\partial z} - \frac{\partial \boldsymbol{H}_z}{\partial x}\right) \tag{A.2b}$$

$$\frac{\partial \boldsymbol{E}_z}{\partial t} = \frac{1}{\varepsilon}\left(\frac{\partial \boldsymbol{H}_y}{\partial x} - \frac{\partial \boldsymbol{H}_x}{\partial y}\right) \tag{A.2c}$$

$$\frac{\partial \boldsymbol{H}_x}{\partial t} = \frac{1}{\mu}\left(\frac{\partial \boldsymbol{E}_y}{\partial z} - \frac{\partial \boldsymbol{E}_z}{\partial y}\right) \tag{A.2d}$$

$$\frac{\partial \boldsymbol{H}_y}{\partial t} = \frac{1}{\mu}\left(\frac{\partial \boldsymbol{E}_z}{\partial x} - \frac{\partial \boldsymbol{E}_x}{\partial z}\right) \tag{A.2e}$$

$$\frac{\partial \boldsymbol{H}_z}{\partial t} = \frac{1}{\mu}\left(\frac{\partial \boldsymbol{E}_x}{\partial y} - \frac{\partial \boldsymbol{E}_y}{\partial x}\right) \tag{A.2f}$$

Three-dimensional (3D) FDTD method numerically solves the Maxwell's curl equations by discretizing the equations in spatial and temporal grids. The simulated structure is divided into small cubic blocks (Yee cells) at the beginning of the simulation, then the electric field and magnetic field at each grid point are computed at a certain instant in time. Figure A.1 shows the electric field and magnetic field components interlace in three spatial dimensions in a Yee cell with grid points spaced Δx, Δy, and Δz apart. Note that the magnetic field components are computed at points one-half grid spacing from the electric field components. The time interval, Δt, in calculating the electromagnetic field components at each grid points is determined by the mesh size and speed of light. During simulation, the electric field components in a volume of space are first computed at time

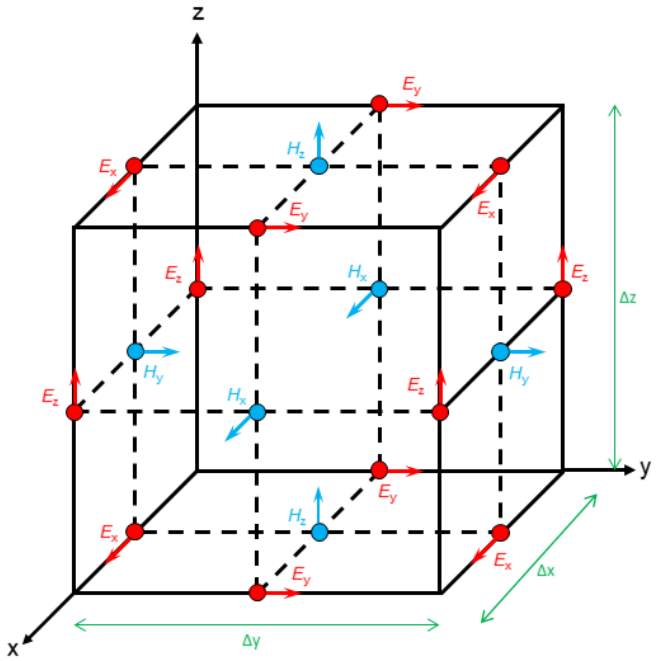

Figure A.1: Yee cell showing the electric field ($\boldsymbol{E}_x$, $\boldsymbol{E}_y$, $\boldsymbol{E}_z$) and magnetic field ($\boldsymbol{H}_x$, $\boldsymbol{H}_y$, $\boldsymbol{H}_z$) components with grid points spaced Δx, Δy, and Δz apart.

$t{=}n\Delta t$, where n is an integer representing the compute step, then the magnetic field components in the same spatial volume are computed at $t{=}(n{+}1)\Delta t$ based on the previously computed magnetic field components and the newly updated electric field components. This alternating computation of electric and magnetic fields at subsequent Δt intervals at a given grid point are repeated in a leapfrog manner until desired transient or steady-state electromagnetic field behavior is achieved.

Figure A.2 illustrates the basic flow of performing 3D FDTD simulation using RSoft FullWAVE developed by Synopsys, Inc. It primarily consists of three steps: setup simulation input files, running simulation, and output results. To begin with, a device structure of interest is built. Next, material properties including relative permittivity $\varepsilon(\boldsymbol{r}, \omega)$ and relative permeability $\mu(\boldsymbol{r}, \omega)$, or refractive index $n(\lambda)$ and absorption coefficient $\alpha(\lambda)$ for each layer is defined. Then, the simulation domain and spatial grid sizes are defined to construct a mesh grid. The grid spacing is

typically set to $< \lambda/10$ where λ is the wavelength in the material to ensure accurate and efficient FDTD calculation. Non-uniform grid size is also employed to allow the smallest feature of the fields to be simulated. In addition, the grid spacing is also related to the time-step Δt through the following Courant condition:

$$c\Delta t < \frac{1}{\sqrt{(1/\Delta x^2 + 1/\Delta y^2 + 1/\Delta z^2)}} \tag{A.3}$$

where c is the velocity of light. The Courant condition must be satisfied in order to obtain a stable simulation. Afterwards, initial launch condition (electromagnetic field excitation) at time t=0 and monitors to record information generated during simulation are defined. Finally, boundary conditions and stop criteria are defined. Perfectly Matched Layer (PML) boundary is typically used to act as a highly lossy material that absorbs all incident energy without producing reflections.

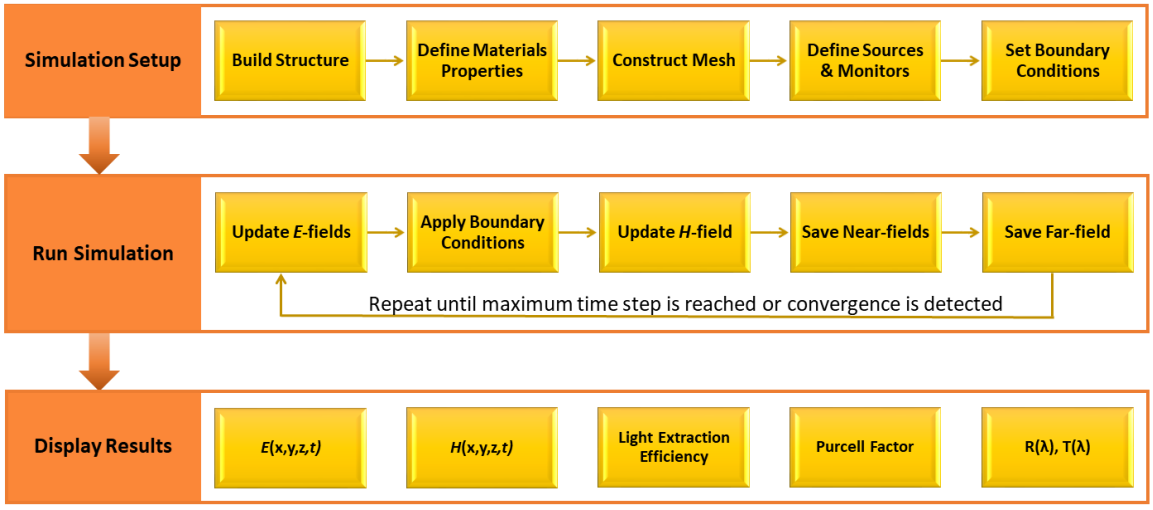

Figure A.2: Flow chart of FDTD simulation.

A.1.1 Calculation of Light Extraction Efficiency

Light extraction efficiency ($\eta_{extraction}$) can be determined by taking the ratio of total extracted power ($P_{extracted}$) to the total power of the dipole source (P_{dipole}), as

expressed in the following equation:

$$\eta_{extraction} = \frac{P_{extracted}}{P_{dipole}} \tag{A.4}$$

During simulation setup, a two-dimensional (2D) plane monitor is typically set at $\lambda/n(\lambda)$ away from the emission surface to calculate the extraction power while a 3D volume monitor surrounding the point source is used to calculate the total launch power. The monitor then calculates the net power passing through the monitor surface by integrating Poynting vectors using the following power integral equation:

$$E(\omega) = \frac{1}{2} \int real\left(P(\omega)\right)\ \mathrm{d}S \tag{A.5}$$

where E is the calculated energy, P(ω) is the Poynting vectors depending on the light angular frequency and dS is the surface normal. The Poynting vectors can be determined from the electric field component $\overrightarrow{\boldsymbol{E}}(\omega)$ based on the planewave approximation:

$$P(\omega) = n(\omega)\sqrt{\frac{\varepsilon_0}{\mu_0}}\left|\overrightarrow{\boldsymbol{E}}(\omega)\right|^2 \tag{A.6}$$

Figure A.3 and Figure A.4 show an example of the parameter setting window for defining the P_{dipole} and the $P_{extracted}$ respectively in the RSoft simulation tool. The monitors have been assigned a unique name – "Zlaunch_pow" for P_{dipole} and "Zmax_pow" for $P_{extracted}$ – for easier reference, as depicted in dash-line circle labeled "1" in both figures. The dimension for the monitors are defined by the "Width", "Height", and "Length" fields in dash-line circle labeled "2". The P_{dipole} monitor is a 3D monitor with the side length set to four grid points along the X, Y and Z direction for the "Width", "Length", and "Height" fields respectively. The $P_{extracted}$ monitor is a two-dimensional (2D) monitor that is defined to have the same size as the plane of interest. For the example shown in Figure A.4, the monitor is intended to collect

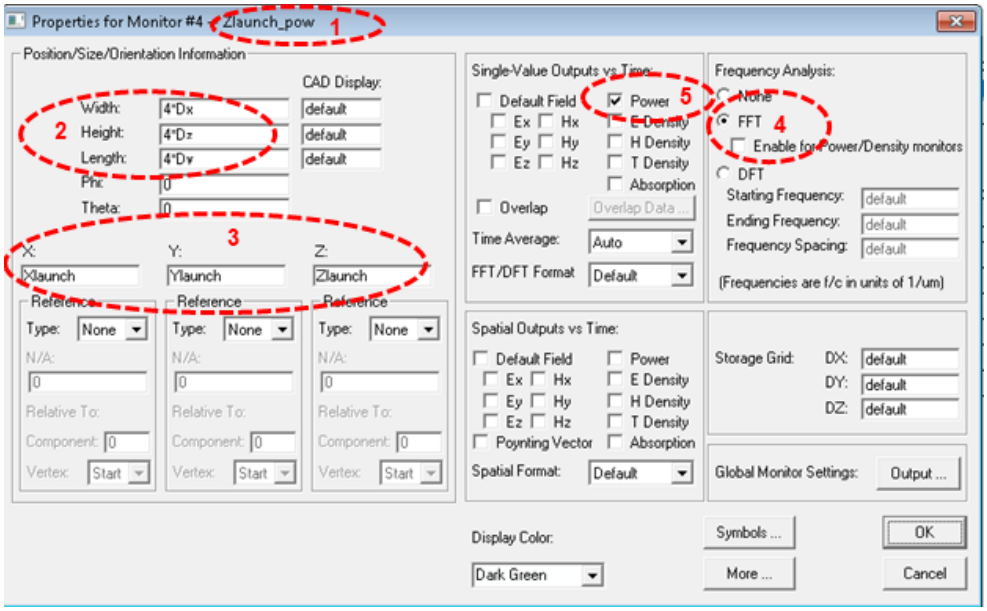

Figure A.3: Parameter setting window for P_{dipole} monitor.

power at the top of the simulation structure. Therefore, the monitor dimension is set to a number defined by "width" and "length" for the field of "Width" and "Length" respectively while the "Height" is set to 0. The location of the monitors are indicated in the fields in the dash-line circle labeled "3". The P_{dipole} monitor is defined to surround the dipole source while the $P_{extracted}$ monitor is placed at one grid point below the simulated region along the +Z direction. FFT analysis has been chosen for the power monitors, as depicted in the dash-line circles labeled "4" and "5" in Figure A.3 and Figure A.4.

A.1.2 Calculation of Far-Field Radiation Pattern

Far-field projection is calculated based on the steady-state near-field data obtained from the simulation. The far-field profile is typically calculated on a hemispherical surface located at distance r away from the simulated structure and the far-field radiation pattern is plotted as if looking straight down on the hemisphere. The intensity of far-field radiation pattern can be determined through the power integral

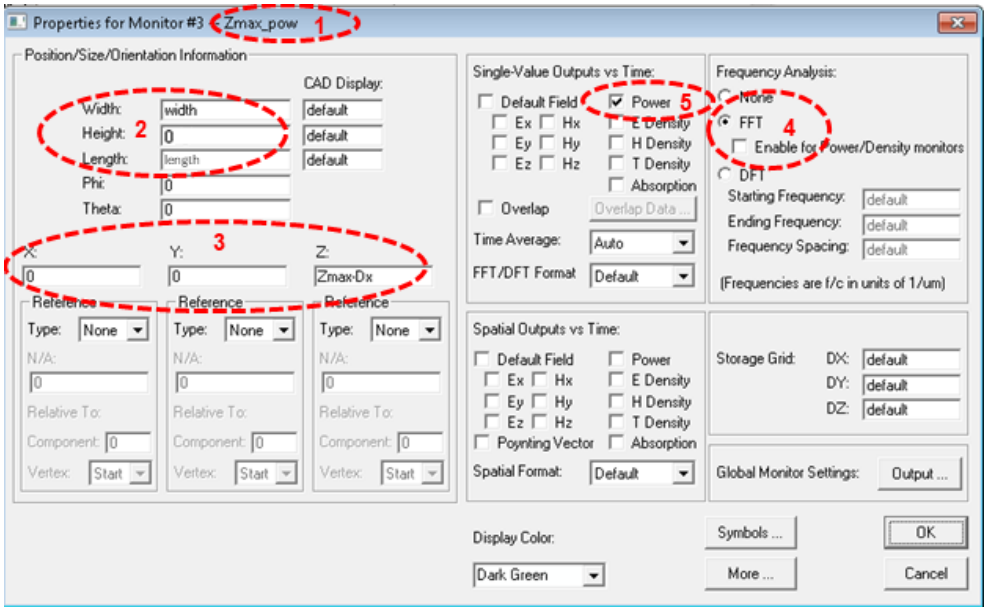

Figure A.4: Parameter setting window for $P_{extracted}$ monitor.

equation in spherical coordinates as followed:

$$E(\omega) = \frac{1}{2} \int \int \left(P(\theta, \phi)\right) r^2 sin(\theta)\, \mathrm{d}\theta \mathrm{d}\phi \tag{A.7}$$

where θ is the polar angle, ϕ is the azimuthal angle and r is the radius of the hemisphere.

Figure A.5 shows the parameter setting window to define an electric field monitor in the RSoft simulation tool. The example shown is a 2D X-Z monitor with dimension defined by the parameters in dash-line circle labeled "2" located at position indicated by the parameters in dash-line circle labeled "3". DFT analysis (dash-line circle labeled "4") has been chosen for this electric field monitor, and the amplitude and phase spatial output of E_x, E_y, and E_z will be recorded (dash-line circles labeled "5" and "6").

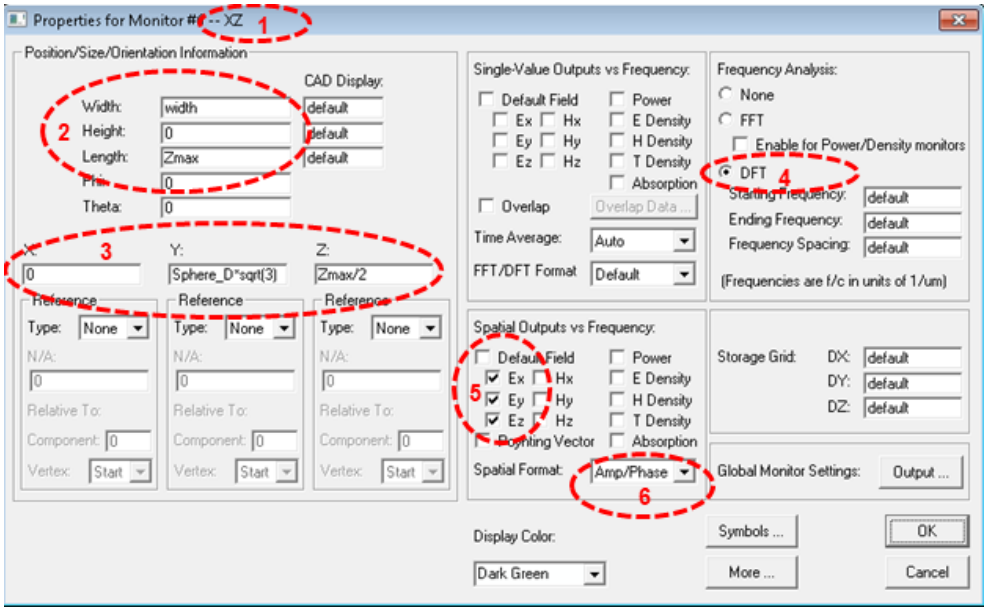

Figure A.5: Parameter setting window for electric field monitor.

A.1.3 Calculation of Purcell Factor

Purcell factor (F_P) define the emission rate enhancement of a spontaneous emitter inside a cavity. In general, F_P can be calculated as followed:

$$F_P = \frac{P_{dipole}}{P_{source}} \tag{A.8}$$

where P_{dipole} is the actual power radiated by a dipole source in the simulated structure and P_{source} is the power that would be radiated by a dipole source in a bulk material with the same refractive index as the active region. As the excitation source is typically normalized to 'Unit Power', the F_P calculation can then be simplified as the average launch power as followed:

$$F_P = \frac{1}{N_{source}N_{polarization}} \sum_{substack N_{source}N_{polarization}} P_{dipole} \tag{A.9}$$

where N_{source} is the number of point sources and $N_{polarization}$ is the number of current directions simulated.

Therefore, the F_P in the RSoft simulation tool can be obtained by taking the average of the value recorded by the P_{dipole} monitor discussed in Section A.1.1 for all simulated polarization directions and the dipole sources.

Bibliography

[1] I Akasaki, H Amano, K Itoh, N Koide, and K Manabe. GaN-based UV/blue light emitting devices. *Institute of Physics Conference Series*, 129:851, 1992.

[2] Shuji Nakamura, Masayuki Senoh, and Takashi Mukai. P-GaN/N-InGaN/N-GaN double-heterostructure blue-light-emitting diodes. *Japanese Journal of Applied Physics*, 32(1 A-B):L8–L11, 1993.

[3] Hadis Morkoç. *Nitride Semiconductor Devices*. Wiley-VCH Verlag GmbH & Co. KGaA, Weinheim, Germany, apr 2013.

[4] Guoqiang Li, Wenliang Wang, Weijia Yang, and Haiyan Wang. Epitaxial growth of group III-nitride films by pulsed laser deposition and their use in the development of LED devices. *Surface Science Reports*, 70(3):380–423, nov 2015.

[5] Wenliang Wang, Weijia Yang, Haiyan Wang, and Guoqiang Li. Epitaxial growth of GaN films on unconventional oxide substrates. *J. Mater. Chem. C*, 2(44):9342–9358, 2014.

[6] Cheng Liu, Yu Kee Ooi, S M Islam, Huili Grace Xing, Debdeep Jena, and Jing Zhang. 234 nm and 246 nm AlN-Delta-GaN quantum well deep ultraviolet light-emitting diodes. *Applied Physics Letters*, 112(1):011101, jan 2018.

[7] Cheng Liu, Yu Kee Ooi, S. M. Islam, Jai Verma, Huili (Grace) Xing, Debdeep Jena, and Jing Zhang. Physics and polarization characteristics of 298 nm AlN-delta-GaN quantum well ultraviolet light-emitting diodes. *Applied Physics Letters*, 110(7):071103, 2017.

[8] Hongping Zhao, Guangyu Liu, and Nelson Tansu. Analysis of InGaN-delta-InN quantum wells for light-emitting diodes. *Applied Physics Letters*, 97(13):131114, sep 2010.

[9] H.P. Zhao, V. Dierolf, G.Y. Liu, G.S. Huang, X.-H. Li, J.D. Poplawsky, R.a. Arif, S. Tafon Penn, and N. Tansu. Design and characteristics of staggered InGaN quantum-well light-emitting diodes in the green spectral regime. *IET Optoelectronics*, 3(6):283–295, dec 2009.

[10] Daniel F. Feezell, James S. Speck, Steven P. DenBaars, and Shuji Nakamura. Semipolar ($20\overline{2}\overline{1}$) InGaN/GaN Light-Emitting Diodes for High-Efficiency Solid-State Lighting. *Journal of Display Technology*, 9(4):190–198, 2013.

[11] R. M. Farrell, E. C. Young, F. Wu, S P DenBaars, and J. S. Speck. Materials and growth issues for high-performance nonpolar and semipolar light-emitting devices. *Semiconductor Science and Technology*, 27(2):024001, feb 2012.

[12] Hisashi Masui, Shuji Nakamura, Steven P. DenBaars, and Umesh K. Mishra. Nonpolar and Semipolar III-Nitride Light-Emitting Diodes: Achievements and Challenges. *IEEE Transactions on Electron Devices*, 57(1):88–100, 2010.

[13] Mathew C. Schmidt, Kwang-Choong Kim, Hitoshi Sato, Natalie Fellows, Hisashi Masui, Shuji Nakamura, Steven P. DenBaars, and James S. Speck. High Power and High External Efficiency m -Plane InGaN Light Emitting Diodes. *Japanese Journal of Applied Physics*, 46(No. 7):L126–L128, feb 2007.

[14] S L Chuang. *Physics of Photonic Devices*. Wiley Series in Pure and Applied Optics. Wiley, 2012.

[15] Chih-Chiang Kao, H C Kuo, K F Yeh, J T Chu, W L Peng, H W Huang, T C Lu, and S C Wang. Light-Output Enhancement of Nano-Roughened GaN Laser Lift-Off Light-Emitting Diodes Formed by ICP Dry Etching. *IEEE Photonics Technology Letters*, 19(11):849–851, 2007.

[16] Xu-Fong Li, Shih-Wei Huang, Hong-Yu Lin, Chun-Yan Lu, Shang-Fu Yang, Ching-Cherng Sun, and Cheng-Yi Liu. Fabrication of patterned sapphire substrate and effect of light emission pattern on package efficiency. *Optical Materials Express*, 5(8):1784, 2015.

[17] Xiao-Hang Li, Peifen Zhu, Guangyu Liu, Jing Zhang, Renbo Song, Yik-Khoon Ee, Pisist Kumnorkaew, James F. Gilchrist, and Nelson Tansu. Light Extraction Efficiency Enhancement of III-Nitride Light-Emitting Diodes by Using 2-D Close-Packed TiO_2 Microsphere Arrays. *Journal of Display Technology*, 9(5):324–332, 2013.

[18] Jonathan J. Wierer, Aurelien David, and Mischa M. Megens. III-nitride photonic-crystal light-emitting diodes with high extraction efficiency. *Nature Photonics*, 3(3):163–169, 2009.

[19] Peng Dong, Jianchang Yan, Junxi Wang, Yun Zhang, Chong Geng, Tongbo Wei, Peipei Cong, Yiyun Zhang, Jianping Zeng, Yingdong Tian, Lili Sun, Qingfeng Yan, Jinmin Li, Shunfei Fan, and Zhixin Qin. 282-nm AlGaN-based deep ultraviolet light-emitting diodes with improved performance on nano-patterned sapphire substrates. *Applied Physics Letters*, 102(24):241113, 2013.

[20] Xinjuan Chen, Cheng Ji, Yong Xiang, Xiangning Kang, Bo Shen, and Tongjun Yu. Angular distribution of polarized light and its effect on light extraction

efficiency in AlGaN deep-ultraviolet light-emitting diodes. *Optics Express*, 24(10):A935, 2016.

[21] Takayoshi Takano, Takuya Mino, Jun Sakai, Norimichi Noguchi, Kenji Tsubaki, and Hideki Hirayama. Deep-ultraviolet light-emitting diodes with external quantum efficiency higher than 20% at 275 nm achieved by improving light-extraction efficiency. *Applied Physics Express*, 10(3):031002, 2017.

[22] Yu Kee Ooi and Jing Zhang. Light Extraction Efficiency Analysis of Flip-Chip Ultraviolet Light-Emitting Diodes With Patterned Sapphire Substrate. *IEEE Photonics Journal*, 10(4):8200913, aug 2018.

[23] Han-Youl Ryu, Il-Gyun Choi, Hyo-Sik Choi, and Jong-In Shim. Investigation of Light Extraction Efficiency in AlGaN Deep-Ultraviolet Light-Emitting Diodes. *Applied Physics Express*, 6(6):62101, 2013.

[24] Keon Hwa Lee, Hyun Jung Park, Seung Hwan Kim, Mojtaba Asadirad, Yong-Tae Moon, Joon Seop Kwak, and Jae-Hyun Ryou. Light-extraction efficiency control in AlGaN-based deep-ultraviolet flip-chip light-emitting diodes: a comparison to InGaN-based visible flip-chip light-emitting diodes. *Optics Express*, 23(16):20340, 2015.

[25] Peng Zhao, Lu Han, Matthew R. McGoogan, and Hongping Zhao. Analysis of TM mode light extraction efficiency enhancement for deep ultraviolet AlGaN quantum wells light-emitting diodes with III-nitride micro-domes, 2012.

[26] Q. Wang, A. T. Connie, H. P. T. Nguyen, M. G. Kibria, S. Zhao, S. Sharif, I. Shih, and Z. Mi. Highly efficient, spectrally pure 340 nm ultraviolet emission from $Al_xGa_{1-x}N$ nanowire based light emitting diodes. *Nanotechnology*, 24(34):345201, 2013.

[27] Thomas F Kent, Santino D Carnevale, A T M Sarwar, Patrick J Phillips, Robert F Klie, and Roberto C Myers. Deep ultraviolet emitting polarization induced nanowire light emitting diodes with $Al_xGa_{1-x}N$ active regions. *Nanotechnology*, 25(45):455201, 2014.

[28] S Zhao, a T Connie, M H T Dastjerdi, X H Kong, Q Wang, M Djavid, S Sadaf, X D Liu, I Shih, H Guo, and Z Mi. Aluminum nitride nanowire light emitting diodes: Breaking the fundamental bottleneck of deep ultraviolet light sources. *Scientific Reports*, 5:8332, 2015.

[29] Yu Kee Ooi, Cheng Liu, and Jing Zhang. Analysis of Polarization-Dependent Light Extraction and Effect of Passivation Layer for 230-nm AlGaN Nanowire Light-Emitting Diodes. *IEEE Photonics Journal*, 9(4):4501712, 2017.

[30] Hongping Zhao, Jing Zhang, Guangyu Liu, and Nelson Tansu. Surface plasmon dispersion engineering via double-metallic Au/Ag layers for III-nitride based light-emitting diodes. *Applied Physics Letters*, 98(15):151115, 2011.

[31] John Henson, Jeff DiMaria, Emmanouil Dimakis, Theodore D Moustakas, and Roberto Paiella. Plasmon-enhanced light emission based on lattice resonances of silver nanocylinder arrays. *Optics Letters*, 37(1):79–81, 2012.

[32] Sang-Hyun Hong, Chu-Young Cho, Sang-Jun Lee, Sang-Youp Yim, Wantae Lim, Sung-Tae Kim, and Seong-Ju Park. Localized surface plasmon-enhanced near-ultraviolet emission from InGaN/GaN light-emitting diodes using silver and platinum nanoparticles. *Optics Express*, 21(3):3138, 2013.

[33] Ahmed Fadil, Daisuke Iida, Yuntian Chen, Jun Ma, Yiyu Ou, Paul Michael Petersen, and Haiyan Ou. Surface plasmon coupling dynamics in InGaN/GaN quantum-well structures and radiative efficiency improvement. *Scientific Reports*, 4:6392, 2014.

[34] Yi Li, Bin Liu, Rong Zhang, Zili Xie, Zhe Zhuang, JiangPing Dai, Tao Tao, Ting Zhi, Guogang Zhang, Peng Chen, Fangfang Ren, Hong Zhao, and Youdou Zheng. Investigation of surface-plasmon coupled red light emitting InGaN/GaN multi-quantum well with Ag nanostructures coated on GaN surface. *Journal of Applied Physics*, 117(15):153103, 2015.

[35] Jing Zhang, Hongping Zhao, and Nelson Tansu. Effect of crystal-field split-off hole and heavy-hole bands crossover on gain characteristics of high Al-content AlGaN quantum well lasers. *Applied Physics Letters*, 97(11):111105, 2010.

[36] Rong-Jun Xie. *Nitride phosphors and solid-state lighting*. Boca Raton, FL : CRC Press, 2011.

[37] JianJang Huang, Shyh-Chiang Shen, and Hao-Chung Kuo, editors. *Nitride Semiconductor Light-Emitting Diodes (LEDs)*. Elsevier, 2014.

[38] Shigefusa F. Chichibu, Akira Uedono, Takeyoshi Onuma, Benjamin A. Haskell, Arpan Chakraborty, Takahiro Koyama, Paul T. Fini, Stacia Keller, Steven P. DenBaars, James S. Speck, Umesh K. Mishra, Shuji Nakamura, Shigeo Yamaguchi, Satoshi Kamiyama, Hiroshi Amano, Isamu Akasaki, Jung Han, and Takayuki Sota. Origin of defect-insensitive emission probability in In-containing (Al,In,Ga)N alloy semiconductors. *Nature Materials*, 5(10):810–816, oct 2006.

[39] Matthias Auf der Maur, Alessandro Pecchia, Gabriele Penazzi, Walter Rodrigues, and Aldo Di Carlo. Efficiency Drop in Green InGaN/GaN Light Emitting Diodes: The Role of Random Alloy Fluctuations. *Physical Review Letters*, 116(2):027401, jan 2016.

[40] Michael Kneissl and Jens Rass, editors. *III-Nitride Ultraviolet Emitters*, volume 227 of *Springer Series in Materials Science*. Springer International Publishing, Cham, 2016.

[41] J. E. Northrup, C. L. Chua, Z. Yang, T. Wunderer, M. Kneissl, N. M. Johnson, and T. Kolbe. Effect of strain and barrier composition on the polarization

of light emission from AlGaN/AlN quantum wells. *Applied Physics Letters*, 100(2):021101, 2012.

[42] Yi-an Chang, Fang-ming Chen, Shan-rong Li, Yen-kuang Kuo, and M Q W U V Leds. Electrical Polarization Effects on the Optical Polarization Properties of AlGaN Ultraviolet Light-Emitting Diodes. *IEEE Transactions on Electron Devices*, 61(9):3233–3238, 2014.

[43] Zachary Bryan, Isaac Bryan, Seiji Mita, James Tweedie, Zlatko Sitar, and Ramón Collazo. Strain dependence on polarization properties of AlGaN and AlGaN-based ultraviolet lasers grown on AlN substrates. *Applied Physics Letters*, 106(23):232101, 2015.

[44] Cyril Pernot, Myunghee Kim, Shinya Fukahori, Tetsuhiko Inazu, Takehiko Fujita, Yosuke Nagasawa, Akira Hirano, Masamichi Ippommatsu, Motoaki Iwaya, Satoshi Kamiyama, Isamu Akasaki, and Hiroshi Amano. Improved Efficiency of 255 – 280 nm AlGaN-Based Light-Emitting Diodes. *Applied Physics Express*, 3(6):061004, 2010.

[45] Masahiro Akiba, Hideki Hirayama, Yuji Tomita, Yusuke Tsukada, Noritoshi Maeda, and Norihiko Kamata. Growth of flat p-GaN contact layer by pulse flow method for high light-extraction AlGaN deep-UV LEDs with Al-based electrode. *Physica Status Solidi (C) Current Topics in Solid State Physics*, 9(3-4):806–809, 2012.

[46] Toru Kinoshita, Toshiyuki Obata, Toru Nagashima, Hiroyuki Yanagi, Baxter Moody, Seiji Mita, Shin Ichiro Inoue, Yoshinao Kumagai, Akinori Koukitu, and Zlatko Sitar. Performance and reliability of deep-ultraviolet light-emitting diodes fabricated on AlN substrates prepared by hydride vapor phase epitaxy. *Applied Physics Express*, 6(9), 2013.

[47] J. J. Wierer, A. A. Allerman, I. Montaño, and M. W. Moseley. Influence of optical polarization on the improvement of light extraction efficiency from reflective scattering structures in AlGaN ultraviolet light-emitting diodes. *Applied Physics Letters*, 105(6):061106, 2014.

[48] SM Islam, Vladimir Protasenko, Sergei Rouvimov, Huili Grace Xing, and Debdeep Jena. Sub-230 nm deep-UV emission from GaN quantum disks in AlN grown by a modified Stranski–Krastanov mode. *Japanese Journal of Applied Physics*, 55(5S):05FF06, 2016.

[49] Dong Yeong Kim, Jun Hyuk Park, Jong Won Lee, Sunyong Hwang, Seung Jae Oh, Jungsub Kim, Cheolsoo Sone, E. Fred Schubert, and Jong Kyu Kim. Overcoming the fundamental light-extraction efficiency limitations of deep ultraviolet light-emitting diodes by utilizing transverse-magnetic-dominant emission. *Light: Science & Applications*, 4(4):e263, 2015.

[50] Hideki Hirayama, Norimichi Noguchi, and Norihiko Kamata. 222 nm Deep-Ultraviolet AlGaN Quantum Well Light-Emitting Diode with Vertical Emission Properties. *Applied Physics Express*, 3(3):032102, 2010.

[51] Sameer Chhajed, Wonseok Lee, Jaehee Cho, E. Fred Schubert, and Jong Kyu Kim. Strong light extraction enhancement in GaInN light-emitting diodes by using self-organized nanoscale patterning of p -type GaN. *Applied Physics Letters*, 98(7), 2011.

[52] Hung-Wen Huang, J T Chu, C C Kao, T H Hseuh, T C Lu, H C Kuo, S C Wang, and C C Yu. Enhanced light output of an InGaN/GaN light emitting diode with a nano-roughened p-GaN surface. *Nanotechnology*, 16(9):1844–1848, sep 2005.

[53] Chia-Feng Lin, Zhong-Jie Yang, Jing-Hui Zheng, and Jing-Jie Dai. Enhanced light output in nitride-based light-emitting diodes by roughening the mesa sidewall. *IEEE Photonics Technology Letters*, 17(10):2038–2040, oct 2005.

[54] T. Fujii, Y. Gao, R. Sharma, E. L. Hu, S. P. DenBaars, and S. Nakamura. Increase in the extraction efficiency of GaN-based light-emitting diodes via surface roughening. *Applied Physics Letters*, 84(6):855, 2004.

[55] Ming Ma, Jaehee Cho, E. Fred Schubert, Yongjo Park, Gi Bum Kim, and Cheolsoo Sone. Strong light-extraction enhancement in GaInN light-emitting diodes patterned with TiO 2 micro-pillars with tapered sidewalls. *Applied Physics Letters*, 101(14):141105, oct 2012.

[56] Xiao Hang Li, Renbo Song, Yik Khoon Ee, Pisist Kumnorkaew, James F. Gilchrist, and Nelson Tansu. Light extraction efficiency and radiation patterns of III-nitride light-emitting diodes with colloidal microlens arrays with various aspect ratios. *IEEE Photonics Journal*, 3(3):489–499, 2011.

[57] Yik Khoon Ee, Pisist Kumnorkaew, Ronald a. Arif, Hua Tong, Hongping Zhao, James F. Gilchrist, and Nelson Tansu. Optimization of light extraction efficiency of III-nitride LEDs with self-assembled colloidal-based microlenses. *IEEE Journal on Selected Topics in Quantum Electronics*, 15(4):1218–1225, 2009.

[58] Yik-Khoon Ee, Pisist Kumnorkaew, Ronald A. Arif, Hua Tong, James F. Gilchrist, and Nelson Tansu. Light extraction efficiency enhancement of InGaN quantum wells light-emitting diodes with polydimethylsiloxane concave microstructures. *Optics Express*, 17(16):13747, aug 2009.

[59] Yik-Khoon Ee, Ronald a. Arif, Nelson Tansu, Pisist Kumnorkaew, and James F. Gilchrist. Enhancement of light extraction efficiency of InGaN quantum wells light emitting diodes using SiO[sub 2]/polystyrene microlens arrays. *Applied Physics Letters*, 91(22):221107, 2007.

[60] Guofeng Yang, Jianjun Chang, Jianli Zhao, Yuying Tong, Feng Xie, Jin Wang, Qing Zhang, Hongjuan Huang, and Dawei Yan. Investigation of light output performance for gallium nitride-based light-emitting diodes grown on different shapes of patterned sapphire substrate. *Materials Science in Semiconductor Processing*, 33:149–153, 2015.

[61] Myunghee Kim, Takehiko Fujita, Shinya Fukahori, Tetsuhiko Inazu, Cyril Pernot, Yosuke Nagasawa, Akira Hirano, Masamichi Ippommatsu, Motoaki Iwaya, Tetsuya Takeuchi, Satoshi Kamiyama, Masahito Yamaguchi, Yoshio Honda, Hiroshi Amano, and Isamu Akasaki. AlGaN-based deep ultraviolet light-emitting diodes fabricated on patterned sapphire substrates. *Applied Physics Express*, 4(9), 2011.

[62] Xiao-long Hu, Ru-lian Wen, Zhao-yi Qi, and Hong Wang. III-nitride ultraviolet, blue and green LEDs with SiO_2 photonic crystals fabricated by UV-nanoimprint lithography. *Materials Science in Semiconductor Processing*, 79:61–65, jun 2018.

[63] Qiming Li, Karl R. Westlake, Mary H. Crawford, Stephen R. Lee, Daniel D. Koleske, Jeffery J. Figiel, Karen C. Cross, Saeed Fathololoumi, Zetian Mi, and George T. Wang. Optical performance of top-down fabricated InGaN/GaN nanorod light emitting diode arrays. *Optics Express*, 19(25):25528, 2011.

[64] Kyeong-Jae Byeon, Joong-Yeon Cho, Jinseung Kim, Hyoungwon Park, and Heon Lee. Fabrication of SiN_x-based photonic crystals on GaN-based LED devices with patterned sapphire substrate by nanoimprint lithography. *Optics Express*, 20(10):11423, 2012.

[65] Elizabeth Rangel, Elison Matioli, Yong Seok Choi, Claude Weisbuch, James S. Speck, and Evelyn L. Hu. Directionality control through selective excitation of low-order guided modes in thin-film InGaN photonic crystal light-emitting diodes. *Applied Physics Letters*, 98(8):96–99, 2011.

[66] Zhihuan Wang and Bahram Nabet. Nanowire Optoelectronics. *Nanophotonics*, 4(1):491–502, 2015.

[67] Mehrdad Djavid and Zetian Mi. Enhancing the light extraction efficiency of AlGaN deep ultraviolet light emitting diodes by using nanowire structures. *Applied Physics Letters*, 108(5), 2016.

[68] Eric A. Evangelou. Contact Resistance Characterization on Gallium Nitride Materials. In *34th Annual Microelectronic Engineering Conference*, Rochester, New York, 2016.

[69] E. F. Schubert. *Light-Emitting Diodes*. Cambridge University Press, 2 edition, 2006.

[70] Han-Youl Ryu. Large enhancement of light extraction efficiency in AlGaN-based nanorod ultraviolet light-emitting diode structures. *Nanoscale Research Letters*, 9(1):58, 2014.

[71] Peifen Zhu, Guangyu Liu, Jing Zhang, and Nelson Tansu. FDTD analysis on extraction efficiency of GaN light-emitting diodes with microsphere arrays. *Journal of Display Technology*, 9(5):317–323, 2013.

[72] Edward D Palik. *Handbook of optical constants of solids*. Academic press, 1998.

[73] C H Yan, H Yao, J M Van Hove, a M Wowchak, P P Chow, and J M Zavada. Ordinary optical dielectric functions of anisotropic hexagonal GaN film determined by variable angle spectroscopic ellipsometry. *Journal of Applied Physics*, 88(6):3463–3469, 2000.

[74] Hideki Hirayama, Sachie Fujikawa, Norimichi Noguchi, Jun Norimatsu, Takayoshi Takano, Kenji Tsubaki, and Norihiko Kamata. 222–282 nm AlGaN and InAlGaN-based deep-UV LEDs fabricated on high-quality AlN on sapphire. *physica status solidi (a)*, 206(6):1176–1182, 2009.

[75] Peifen Zhu. Frustrated total internal reflection in organic light-emitting diodes employing sphere cavity embedded in polystyrene. *Journal of Optics*, 18(2):25403, 2016.

[76] Haiyong Gao, Fawang Yan, Yang Zhang, Jinmin Li, Yiping Zeng, and Guohong Wang. Enhancement of the light output power of InGaN/GaN light-emitting diodes grown on pyramidal patterned sapphire substrates in the micro- and nanoscale. *Journal of Applied Physics*, 103(1), 2008.

[77] Yonghui Zhang, Tongbo Wei, Junxi Wang, Ding Lan, Yu Chen, Qiang Hu, Hongxi Lu, and Jinmin Li. The improvement of GaN-based light-emitting diodes using nanopatterned sapphire substrate with small pattern spacing. *AIP Advances*, 4(2):1–7, 2014.

[78] Songrui Zhao, Hieu P.T. Nguyen, Md G. Kibria, and Zetian Mi. III-Nitride nanowire optoelectronics. *Progress in Quantum Electronics*, 44:14–68, 2015.

[79] Shunfeng Li and Andreas Waag. GaN based nanorods for solid state lighting. *Journal of Applied Physics*, 111(7), 2012.

[80] Ruoxue Yan, Daniel Gargas, and Peidong Yang. Nanowire photonics. *Nature Photonics*, 3(10):569–576, 2009.

[81] Frank Glas. Critical dimensions for the plastic relaxation of strained axial heterostructures in free-standing nanowires. *Physical Review B - Condensed Matter and Materials Physics*, 74(12):2–5, 2006.

[82] Xing Lei. Development of Nanosphere Lithography for Semiconductor Device Applications. Master's thesis, Rochester Institute of Technology, 2016.

[83] Matthew Hartensveld. Optimization of Dry and Wet GaN Etching to Form High Aspect Ratio Nanowires. Master's thesis, Rochester Institute of Technology, 2018.

[84] H. P. T. Nguyen, M. Djavid, and Z. Mi. Nonradiative Recombination Mechanism in Phosphor-Free GaN-Based Nanowire White Light Emitting Diodes and the effect of Ammonium Sulfide Surface Passivation. *ECS Transactions*, 53(2):93–100, may 2013.

[85] S. A. Chevtchenko, M. A. Reshchikov, Q. Fan, X. Ni, Y. T. Moon, A. A. Baski, and H. Morkoç. Study of SiN_x and SiO_2 passivation of GaN surfaces. *Journal of Applied Physics*, 101(11):113709, jun 2007.

[86] S. Jahangir, M. Mandl, M. Strassburg, and P. Bhattacharya. Molecular beam epitaxial growth and optical properties of red-emitting (λ = 650 nm) InGaN/GaN disks-in-nanowires on silicon. *Applied Physics Letters*, 102(7):071101, 2013.

[87] A. Armstrong, Q. Li, Y. Lin, A. A. Talin, and G. T. Wang. GaN nanowire surface state observed using deep level optical spectroscopy. *Applied Physics Letters*, 96(16):163106, 2010.

[88] Wei-Jhih Tseng, D. H. van Dorp, R. R. Lieten, P. M. Vereecken, R. Langer, and G. Borghs. Impact of Plasma-Induced Surface Damage on the Photoelectrochemical Properties of GaN Pillars Fabricated by Dry Etching. *The Journal of Physical Chemistry C*, 118(21):11261–11266, may 2014.

[89] Ki-Sik Im, Chul-Ho Won, Sindhuri Vodapally, Dong-Hyeok Son, Young-Woo Jo, YoHan Park, Jae-Hoon Lee, and Jung-Hee Lee. Lateral GaN nanowire prepared by using two-step TMAH wet etching and HfO_2 sidewall spacer. *Journal of Crystal Growth*, 441:41–45, may 2016.

[90] Yung-Yu Lai, Shih-Chieh Hsu, Hua-Sheng Chang, YewChung Sermon Wu, Ching-Hsiang Chen, Liang-Yih Chen, and Yuh-Jen Cheng. The study of wet etching on GaN surface by potassium hydroxide solution. *Research on Chemical Intermediates*, 43(6):3563–3572, jun 2017.

[91] M Kneissl, T Kolbe, C Chua, V Kueller, N Lobo, J Stellmach, A Knauer, H Rodriguez, S Einfeldt, Z Yang, N M Johnson, and M Weyers. Advances in group III-nitride-based deep UV light-emitting diode technology. *Semiconductor Science and Technology*, 26(1):014036, 2011.

[92] Yitao Liao, Christos Thomidis, Chen-kai Kao, and Theodore D. Moustakas. AlGaN based deep ultraviolet light emitting diodes with high internal quantum efficiency grown by molecular beam epitaxy. *Applied Physics Letters*, 98(2011):081110, 2011.

[93] Anne-Line Henneghien, Bruno Gayral, Yohan Désières, and Jean-Michel Gérard. Simulation of waveguiding and emitting properties of semiconductor nanowires with hexagonal or circular sections. *Journal of the Optical Society of America B*, 26(12):2396, 2009.

[94] Jordan Chesin, X. Zhou, and Silvija Gradečak. Light extraction in individual GaN nanowires on Si for LEDs. *Proceedings of SPIE*, 8467:846703, 2012.

[95] Mohsen Nami and Daniel Feezell. Optical properties of Ag-coated GaN/InGaN axial and core–shell nanowire light-emitting diodes. *Journal of Optics*, 17(2):025004, feb 2015.

[96] X. Zhou, M.-Y. Lu, Y.-J. Lu, E. J. Jones, S. Gwo, and S. Gradečak. Nanoscale Optical Properties of Indium Gallium Nitride / Gallium Nitride Nanodisk-in-Rod Heterostructures. *ACS Nano*, 9(3):2868–2875, 2015.

[97] Cheng Liu, Yu Kee Ooi, and Jing Zhang. Proposal and physics of AlInN-delta-GaN quantum well ultraviolet lasers. *Journal of Applied Physics*, 119(8):083102, 2016.

[98] Wei Guo, Meng Zhang, Animesh Banerjee, and Pallab Bhattacharya. Catalyst-free InGaN/GaN nanowire light emitting diodes grown on (001) silicon by molecular beam epitaxy. *Nano Letters*, 10(9):3356–3359, 2010.

[99] Wei Guo, Meng Zhang, Pallab Bhattacharya, and Junseok Heo. Auger recombination in III-nitride nanowires and its effect on nanowire light-emitting diode characteristics. *Nano Letters*, 11(4):1434–1438, 2011.

[100] Q Wang, J Bai, Y P Gong, and T Wang. Influence of strain relaxation on the optical properties of InGaN/GaN multiple quantum well nanorods. *Journal of Physics D: Applied Physics*, 44(39):395102, 2011.

[101] G Jacopin, L Rigutti, S Bellei, P Lavenus, F H Julien, a V Davydov, D Tsvetkov, K a Bertness, N a Sanford, J B Schlager, and M Tchernycheva. Photoluminescence polarization in strained GaN/AlGaN core/shell nanowires. *Nanotechnology*, 23(32):325701, 2012.

[102] Chao Zhao, Tien Khee Ng, Aditya Prabaswara, Michele Conroy, Shafat Jahangir, Thomas Frost, John O'Connell, Justin D Holmes, Peter J Parbrook, Pallab Bhattacharya, and Boon S Ooi. An enhanced surface passivation effect in InGaN/GaN disk-in-nanowire light emitting diodes for mitigating Shockley-Read-Hall recombination. *Nanoscale*, 7(40):16658–65, 2015.

[103] Hieu Pham Trung Nguyen, Shaofei Zhang, Ashfiqua T. Connie, Md Golam Kibria, Qi Wang, Ishiang Shih, and Zetian Mi. Breaking the carrier injection bottleneck of phosphor-free nanowire white light-emitting diodes. *Nano Letters*, 13(11):5437–5442, 2013.

[104] Yang Kuo, Chun-Han Lin, Horng-Shyang Chen, Chieh Hsieh, Charng-Gan Tu, Pei-Ying Shih, Chung-Hui Chen, Che-Hao Liao, Chia-Ying Su, Yu-Feng Yao, Hao-Tsung Chen, Yean-Woei Kiang, and Chih-Chung Yang. Surface plasmon coupled light-emitting diode: Experimental and numerical studies. *Japanese Journal of Applied Physics*, 54(2S):02BD01, feb 2015.

[105] Chun-Han Lin, Chieh Hsieh, Charng-Gan Tu, Yang Kuo, Horng-Shyang Chen, Pei-Ying Shih, Che-Hao Liao, Yean-Woei Kiang, C. C. Yang, Chih-Han Lai, Guan-Ru He, Jui-Hung Yeh, and Ta-Cheng Hsu. Efficiency improvement of a vertical light-emitting diode through surface plasmon coupling and grating scattering. *Optics Express*, 22(S3):A842, may 2014.

[106] Cheng-Hsueh Lu, Chia-Chun Lan, Yen-Lin Lai, Yun-Li Li, and Chuan-Pu Liu. Enhancement of Green Emission from InGaN/GaN Multiple Quantum Wells via Coupling to Surface Plasmons in a Two-Dimensional Silver Array. *Advanced Functional Materials*, 21(24):4719–4723, dec 2011.

[107] Giuseppe Y. Mak, W. Y. Fu, Edmund Y. Lam, and H. W. Choi. Metallic nanoparticle array on GaN by microsphere lithography. *physica status solidi (c)*, 6(S2):S654–S657, jun 2009.

[108] Jun-Ho Sung, Bo-Soon Kim, Chul-Hyun Choi, Min-Woo Lee, Seung-Gol Lee, Se-Geun Park, El-Hang Lee, and O. Beom-Hoan. Enhanced luminescence of GaN-based light-emitting diode with a localized surface plasmon resonance. *Microelectronic Engineering*, 86(4-6):1120–1123, apr 2009.

[109] Dong-Ming Yeh, Chi-Feng Huang, Cheng-Yen Chen, Yen-Cheng Lu, and C C Yang. Localized surface plasmon-induced emission enhancement of a green light-emitting diode. *Nanotechnology*, 19(34):345201, aug 2008.

[110] Min-Ki Kwon, Ja-Yeon Kim, Baek-Hyun Kim, Il-Kyu Park, Chu-Young Cho, Clare Chisu Byeon, and Seong-Ju Park. Surface-Plasmon-Enhanced Light-Emitting Diodes. *Advanced Materials*, 20(7):1253–1257, apr 2008.

[111] Koichi Okamoto, Isamu Niki, Alexander Shvartser, Yukio Narukawa, Takashi Mukai, and Axel Scherer. Surface-plasmon-enhanced light emitters based on InGaN quantum wells. *Nature Materials*, 3(9):601–605, 2004.

[112] Koichi Okamoto. *Surface Plasmon Enhanced Solid-State Light-Emitting Devices*. Springer New York, New York, NY, 2010.

[113] J. Shakya, K. Knabe, K. H. Kim, J. Li, J. Y. Lin, and H. X. Jiang. Polarization of III-nitride blue and ultraviolet light-emitting diodes. *Applied Physics Letters*, 86(9):091107, 2005.

[114] C. Wiesmann, K. Bergenek, N. Linder, and U.T. Schwarz. Photonic crystal LEDs - designing light extraction. *Laser & Photonics Review*, 3(3):262–286, 2009.

[115] Dongwoo Kim, Hyoyoung Lee, Namgil Cho, Younjoon Sung, and Geunyoung Yeom. Effect of GaN microlens array on efficiency of GaN-based blue-light-emitting diodes. *Japanese Journal of Applied Physics, Part 2: Letters*, 44(1-7), 2005.

[116] Rui Zhang, Hang Lin, Yunlong Yu, Daqin Chen, Ju Xu, and Yuansheng Wang. A new-generation color converter for high-power white LED: Transparent Ce^{3+}: YAG phosphor-in-glass. *Laser and Photonics Reviews*, 8(1):158–164, 2014.

[117] Yukuan Chu, Chunyu Chen, and Chingfu Tsou. A Silicon-Based LED Packaging Substrate With an Island Structure for Phosphor Encapsulation Shaping. *IEEE Transactions on Components, Packaging and Manufacturing Technology*, 5(2):155–162, feb 2015.

[118] Yu Kee Ooi and Jing Zhang. Design analysis of phosphor-free monolithic white light-emitting-diodes with InGaN/ InGaN multiple quantum wells on ternary InGaN substrates. *AIP Advances*, 5(5):057168, 2015.

[119] Chih Feng Lu, Chi Feng Huang, Yung Sheng Chen, Wen Y. Shiao, Cheng Y. Chen, Yen Cheng Lu, and Chih Chung Yang. Phosphor-free monolithic white-light LED. *IEEE Journal on Selected Topics in Quantum Electronics*, 15(4):1210–1217, 2009.

[120] M.H. Crawford. LEDs for Solid-State Lighting: Performance Challenges and Recent Advances. *IEEE Journal of Selected Topics in Quantum Electronics*, 15(4):1028–1040, 2009.

[121] Young Chul Sim, Seung Hyuk Lim, Yang Seok Yoo, Min Ho Jang, Sunghan Choi, Hwan Seop Yeo, Kie Young Woo, Sangwon Lee, Hyun Gyu Song, and Yong Hoon Cho. Three-dimensional GaN dodecagonal ring structures for highly efficient phosphor-free warm white light-emitting diodes. *Nanoscale*, 10(10):4686–4695, 2018.

[122] Nan Guan, Xing Dai, Agnès Messanvi, Hezhi Zhang, Jianchang Yan, Eric Gautier, Catherine Bougerol, François H. Julien, Christophe Durand, Joël Eymery, and Maria Tchernycheva. Flexible White Light Emitting Diodes Based on Nitride Nanowires and Nanophosphors. *ACS Photonics*, 3(4):597–603, 2016.

[123] Seung-Hyuk Lim, Young-Ho Ko, Christophe Rodriguez, Su-Hyun Gong, and Yong-Hoon Cho. Electrically driven, phosphor-free, white light-emitting diodes using gallium nitride-based double concentric truncated pyramid structures. *Light: Science & Applications*, 5(2):e16030, 2016.

[124] Shafat Jahangir, Ines Pietzonka, Martin Strassburg, and Pallab Bhattacharya. Monolithic phosphor-free InGaN/GaN quantum dot wavelength converter white light emitting diodes. *Applied Physics Letters*, 105(11):111117, 2014.

[125] C. B. Soh, W. Liu, J. H. Teng, S. Y. Chow, S. S. Ang, and S. J. Chua. Cool white III-nitride light emitting diodes based on phosphor-free indium-rich InGaN nanostructures. *Applied Physics Letters*, 92(26):261909, 2008.

[126] H. P T Nguyen, S. Zhang, K. Cui, X. Han, S. Fathololoumi, M. Couillard, G. a. Botton, and Z. Mi. P-type modulation doped InGaN/GaN dot-in-a-wire white-light-emitting diodes monolithically grown on Si(111). *Nano Letters*, 11(5):1919–1924, 2011.

[127] Wei Guo, Animesh Banerjee, Pallab Bhattacharya, and Boon S. Ooi. InGaN/GaN disk-in-nanowire white light emitting diodes on (001) silicon. *Applied Physics Letters*, 98(19):193102, 2011.

[128] Binglei Fu, Yan Cheng, Zhao Si, Tongbo Wei, Xionghui Zeng, Guodong Yuan, Zhiqiang Liu, Hongxi Lu, Xiaoyan Yi, Jinmin Li, and Junxi Wang. Phosphor-free InGaN micro-pyramid white light emitting diodes with multilayer graphene electrode. *RSC Adv.*, 5(122):100646–100650, 2015.

[129] FullWAVE, Synopsys's Optical Solutions Group. [Online]. Available: `https://optics.synopsys.com`.

[130] Hongping Zhao, Guangyu Liu, Jing Zhang, Jonathan D Poplawsky, Volkmar Dierolf, and Nelson Tansu. Approaches for high internal quantum efficiency green InGaN light-emitting diodes with large overlap quantum wells. *Optics Express*, 19(S4):A991, 2011.

[131] Michael R Krames, Oleg B Shchekin, Regina Mueller-Mach, Gerd O Mueller, Ling Zhou, Gerard Harbers, and M George Craford. Status and Future of High-Power Light-Emitting Diodes for Solid-State Lighting. *Journal of Display Technology*, 3(2):160–175, 2007.

[132] Jeffrey Y. Tsao, Mary H. Crawford, Michael E. Coltrin, Arthur J. Fischer, Daniel D. Koleske, Ganapathi S. Subramania, G. T. Wang, Jonathan J. Wierer, and Robert F. Karlicek. Toward Smart and Ultra-efficient Solid-State Lighting. *Advanced Optical Materials*, 2(9):809–836, 2014.

[133] Joanna McKittrick and Lauren E. Shea-Rohwer. Review: Down conversion materials for solid-state lighting. *Journal of the American Ceramic Society*, 97(5):1327–1352, 2014.

[134] Hongjian Li, Panpan Li, Junjie Kang, Zhi Li, Zhicong Li, Jing Li, Xiaoyan Yi, and Guohong Wang. Phosphor-free, color-tunable monolithic InGaN light-emitting diodes. *Applied Physics Express*, 6(10):102103, 2013.

[135] Kui Wu, Tongbo Wei, Haiyang Zheng, Ding Lan, Xuecheng Wei, Qiang Hu, Hongxi Lu, Junxi Wang, Yi Luo, and Jinmin Li. Fabrication and optical characteristics of phosphor-free InGaN nanopyramid white light emitting diodes by nanospherical-lens photolithography. *Journal of Applied Physics*, 115(12):123101, 2014.

[136] Benjamin Damilano, Nicolas Grandjean, Cyril Pernot, and Jean Massies. Monolithic White Light Emitting Diodes Based on InGaN/GaN Multiple-Quantum Wells. *Japanese Journal of Applied Physics*, 40(Part 2, No. 9A/B):L918–L920, 2001.

[137] Motokazu Yamada, Yukio Narukawa, and Takashi Mukai. Phosphor Free High-Luminous-Efficiency White Light-Emitting Diodes Composed of InGaN Multi-Quantum Well. *Japanese Journal of Applied Physics*, 41(Part 2, No. 3A):L246–L248, 2002.

[138] Sung-Nam Lee, H. S. Paek, H. Kim, T. Jang, and Y. Park. Monolithic InGaN-based white light-emitting diodes with blue, green, and amber emissions. *Applied Physics Letters*, 92(8):081107, 2008.

[139] Chee-keong Tan and Nelson Tansu. Nanostructured lasers: Electrons and holes get closer. *Nature Nanotechnology*, 10(2):107–109, 2015.

[140] Hon-Way Lin, Yu-Jung Lu, Hung-Ying Chen, Hong-Mao Lee, and Shangjr Gwo. InGaN/GaN nanorod array white light-emitting diode. *Applied Physics Letters*, 97(7):073101, 2010.

[141] M. Funato, K. Hayashi, M. Ueda, Y. Kawakami, Y. Narukawa, and T. Mukai. Emission color tunable light-emitting diodes composed of InGaN multifacet quantum wells. *Applied Physics Letters*, 93(2):021126, 2008.

[142] Chu-Young Cho, Il-Kyu Park, Min-Ki Kwon, Ja-Yeon Kim, Seong-Ju Park, Dong-Ryul Jung, and Kwang-Woo Kwon. InGaN/GaN multiple quantum wells grown on microfacets for white-light generation. *Applied Physics Letters*, 93(24):241109, 2008.

[143] Jing Zhang and Nelson Tansu. Improvement in spontaneous emission rates for InGaN quantum wells on ternary InGaN substrate for light-emitting diodes. *Journal of Applied Physics*, 110(11):113110, 2011.

[144] Jing Zhang and Nelson Tansu. Engineering of AlGaN-Delta-GaN Quantum-Well Gain Media for Mid- and Deep-Ultraviolet Lasers. *IEEE Photonics Journal*, 5(2):2600209, 2013.

[145] Masaya Shimizu, Yasutoshi Kawaguchi, Kazumasa Hiramatsu, and Nobuhiko Sawaki. MOVPE growth of thick homogeneous InGaN directly on sapphire substrate using AlN buffer layer. *Solid-State Electronics*, 41(2):145–147, 1997.

[146] D. Doppalapudi, S. N. Basu, K. F. Ludwig, and T. D. Moustakas. Phase separation and ordering in InGaN alloys grown by molecular beam epitaxy. *Journal of Applied Physics*, 84(3):1389–1395, 1998.

[147] Shucheng Chu, Tetsuhiro Saisho, Kazuo Fujimura, Shingo Sakakibara, Fumiyasu Tanoue, Kenei Ishino, Akihiro Ishida, Hiroshi Harima, Yefan Chen,

Takafumi Yao, and Hiroshi Fujiyasu. High-Quality InGaN Films Grown by Hot-Wall Epitaxy with Mixed (Ga+In) Source. *Japanese Journal of Applied Physics*, 38(Part 2, No. 4B):L427–L429, 1999.

[148] T. L. Williamson, M. a. Hoffbauer, K. M. Yu, L. a. Reichertz, M. E. Hawkridge, R. E. Jones, N. Miller, J. W. Ager, Z. Liliental-Weber, and W. Walukiewicz. Highly luminescent InxGa1-xN thin films grown over the entire composition range by energetic neutral atom beam lithography & epitaxy (ENABLE). *physica status solidi (c)*, 6(S2):S409–S412, 2009.

[149] Mark a. Hoffbauer, Todd L. Williamson, Joshua J. Williams, Julia L. Fordham, Kin M. Yu, Wladek Walukiewicz, and Lothar a. Reichertz. In-rich InGaN thin films: Progress on growth, compositional uniformity, and doping for device applications. *Journal of Vacuum Science & Technology B: Microelectronics and Nanometer Structures*, 31(3):03C114, 2013.

[150] I. Vurgaftman and J. R. Meyer. Band parameters for nitrogen-containing semiconductors. *Journal of Applied Physics*, 94(6):3675–3696, 2003.

[151] Igor Vurgaftman and Jerry R. Meyer. Electron Bandstructure Parameters. In Joachim Piprek, editor, *Nitride Semiconductor Devices: Principles and Simulation*, chapter 2, pages 13–48. Wiley-VCH Verlag GmbH & Co. KGaA, Weinheim, Germany, 2007.

[152] Guangyu Liu, Jing Zhang, Chee Keong Tan, and Nelson Tansu. Efficiency-Droop Suppression by Using Large-Bandgap AlGaInN Thin Barrier Layers in InGaN Quantum-Well Light-Emitting Diodes. *IEEE Photonics Journal*, 5(2):2201011, 2013.